

**DIRECT COMPARISONS OF POLARIMETRIC C-BAND AND
S-BAND RADAR IN SNOW**

BRANDON M. TAYLOR

A THESIS SUBMITTED TO THE FACULTY OF GRADUATE STUDIES
IN PARTIAL FULFILMENT OF THE REQUIREMENTS
FOR THE DEGREE OF

MASTER OF SCIENCE

GRADUATE PROGRAM IN EARTH AND SPACE SCIENCE
YORK UNIVERSITY
TORONTO, ONTARIO
APRIL 2018

**DIRECT COMPARISONS OF
POLARIMETRIC C-BAND AND S-BAND
RADAR IN SNOW**

by **Brandon M. Taylor**

a thesis submitted to the Faculty of Graduate Studies of
York University in partial fulfilment of the requirements
for the degree of

MASTER OF SCIENCE
© 2018

Permission has been granted to: a) YORK UNIVERSITY LIBRARIES to lend or sell copies of this dissertation in paper, microform or electronic formats, and b) LIBRARY AND ARCHIVES CANADA to reproduce, lend, distribute, or sell copies of this thesis anywhere in the world in microform, paper or electronic formats *and* to authorise or procure the reproduction, loan, distribution or sale of copies of this thesis anywhere in the world in microform, paper or electronic formats.

The author reserves other publication rights, and neither the thesis nor extensive extracts for it may be printed or otherwise reproduced without the author's written permission.

DIRECT COMPARISONS OF POLARIMETRIC C-BAND AND S-BAND RADAR IN SNOW

by **Brandon M. Taylor**

By virtue of submitting this document electronically, the author certifies that this is a true electronic equivalent of the copy of the thesis approved by York University for the award of the degree. No alteration of the content has occurred and if there are any minor variations in formatting, they are as a result of the conversion to Adobe Acrobat format (or similar software application).

Examination Committee Members:

1. Mark Gordon
2. George Isaac
3. Dave Sills
4. Don Hastie

Abstract

The Canadian Weather Radar Network is currently undergoing an upgrade to polarimetric, S-Band radar systems. Forecasting experiences in Canada with the legacy C-Band radars lends to the idea that the narrow beamwidth of C-Band systems is preferential for nowcasting the typical shallow lake-effect snow event. This idea is tested by comparing moments from King City radar, just north of Toronto, to the neighboring Buffalo, NY WSR-88D. By transforming the radar data from spherical coordinates to the Cartesian coordinate system, the two radars can be compared directly. Objective analysis indicates that the spatial patterns of reflectivity are very similar, with King maintaining the obvious advantage in resolving fine scale features of lake-effect snow bands through a narrow physical beamwidth. Also, it is shown that comparatively, the mean reflectivity values obtained through this method are similar, but King City maintains a slight advantage over Buffalo in detecting shallow snow-squalls. In regards to differential reflectivity, a case by case comparison is performed to determine any event biases from the King City radar. With biases removed, both radars indicate similar mean values of differential reflectivity, which agrees with theoretical expectations. Results also indicate that the bulk hydrometeor type in synoptic snowfalls tend towards pristine crystals, while lake-effect events tend towards aggregated snow.

Dedication

for my little family, Liz and Inola

Acknowledgements

I would like thank my primary supervisor, Dr. Peter Taylor, for enabling me to pursue my passion for meteorology, and providing insightful critiques to my work. My co-supervisor and committee member Drs. George Isaac and David Sills played a big role in guiding me through my research, and I greatly thank them for their viewpoints. Dr. Diar Hassan was the spark for this research, and I thank him for being a mentor to me. I would also like to thank and acknowledge Sudesh Boodoo at Environment and Climate Change Canada for providing data from King City research radar, and the NOAA big data project for enabling access to NWS radar data. Thanks to the NSERC Discovery Grant and The Weather Network for financial support. I couldn't have moved to another country and completed this research without my wife Liz by my side. She has supported me from day one. I would like to express my love and appreciation for my family, my Mom for giving me the weather-bug, my Dad for his writing skills, and both for a strong foundation in maths. Thanks to my sisters Lauren and Jenna for coming to visit in Toronto. I love you all. Finally, my friends and colleagues Zheng Qi Wang and Kaiti (Tim) Jiang were always there for pints of wisdom.

Table of Contents

Abstract	iv
Acknowledgements	vi
Table of Contents	vii
List of Figures	x
1 Chapter One	1
1.1 Introduction	1
1.2 Background	2
1.2.1 Radar Locations	3
1.2.2 Equivalent Reflectivity Factor (Z_h)	4
1.2.3 Differential Reflectivity (Z_{dr})	4
1.2.4 Co-polar Cross-Correlation Coefficient (ρ_{hv})	5
2 Chapter Two	7
2.1 Methodology	7
2.1.1 Comparison of Radar Systems	7
2.1.2 Distance-Weighting Scheme	10
2.2 Selection of Cases	12

2.3	Filtering Conditions	13
2.3.1	Time Filter	13
2.3.2	Gate Filters	14
2.4	Advanced Statistical Techniques	14
2.4.1	Bi-Variate Kernel Density Estimation	14
2.4.2	Orthonormal Linear Regression	16
2.5	Z_{DR} Bias Estimation	16
3	Chapter Three	18
3.1	Event Comparisons	18
3.1.1	18 January 2014 - Synoptic	18
3.1.2	23 January 2014 - Lake-Effect	21
3.1.3	1 February 2014 - Synoptic	24
3.1.4	6 January 2015 - Lake-Effect	27
3.1.5	7 January 2015 - Synoptic	30
3.1.6	6 February 2015 - Synoptic	33
3.1.7	14 February 2015 - Lake-Effect	36
3.1.8	18 February 2015 - Lake-Effect	39
3.1.9	10 February 2016 - Lake-Effect	42
3.1.10	15 December 2016 - Synoptic	45
3.2	Z_{eH} Subset Comparisons	48
3.3	KDE Constrained Z_{DR}	50
3.3.1	Unbiased Z_{DR} Cases	50
3.3.2	Biased Z_{DR} Cases	55
4	Chapter Four	61
4.1	Discussion	61

4.1.1	Diagnosing Z_{DR} Bias	61
4.1.2	Z_{DR} Statistics	64
4.1.3	Relative Merits of C-Band vs. S-Band in Lake-Effect Snow .	65
5	Chapter Five	67
5.1	Conclusions	67
A	Appendix A	69
A.1	Upper-Air Charts	69
A.2	Skew-T Charts	69
A.3	Sounding Climatology	69
	Bibliography	91

List of Figures

1.1	The location of the NWS Buffalo Radar (KBUF) and King City Radar (CWKR) are shown as red dots, with a 100 km range ring around each. The distance between the two, drawn as a blue line, is 131.5 km.	3
1.2	Chart of expected ranges of Z_{DR} for a variety of targets. Taken from Fabry (2015).	5
2.1	Bounding box of the study area, denoted by the green shading.	8
2.2	Base moment comparisons between radars over Lake Ontario, with dimensions of 20x12.5 km. Left panels are in native radars coordinates, with gates outlined in black. Right panels are transformed to a common Cartesian grid, with grid cells outlined in black.	11
2.3	Scatter-plot of matched points illustrating the high density of the points (left). The total of points in this figure are 147,457. 2-D histogram of the same matched points, binned to native data resolution (right).	15
2.4	Demonstration of an Orthonormal Linear Regression	16
3.1	Gridded Z_{eH} comparison for 18 January 2014. Time-average of all admitted scans.	19

3.2	Gridded Z_{DR} comparison for 18 January 2014. Time-average of all admitted scans.	19
3.3	Direct comparisons for 18 January 2014. Dataset includes all admitted grid cells.	20
3.4	Histograms of Z_{DR} (left), Z_{DR} bias at CWKR (right). Bias is calculated by subtracting the gridded, bias-adjusted Z_{DR} at KBUF from the Z_{DR} at CWKR. Both datasets include points with KDE ≥ 2 . The modal bin is shaded red.	21
3.5	Gridded Z_{eH} comparison for 23 January 2014. Time-average of all admitted scans.	22
3.6	Gridded Z_{DR} comparison for 23 January 2014. Time-average of all admitted scans.	22
3.7	Direct comparisons for 23 January 2014. Dataset includes all admitted grid cells.	23
3.8	Histograms of Z_{DR} (left), Z_{DR} bias at CWKR (right). Bias is calculated by subtracting the gridded, bias-adjusted Z_{DR} at KBUF from the Z_{DR} at CWKR. Both datasets include points with KDE ≥ 2 . The modal bin is shaded red.	24
3.9	Gridded Z_{eH} comparison for 1 February 2014. Time-average of all admitted scans.	25
3.10	Gridded Z_{DR} comparison for 1 February 2014. Time-average of all admitted scans.	25
3.11	Direct comparisons for 1 February 2014. Dataset includes all admitted grid cells.	26

3.12 Histograms of Z_{DR} (left), Z_{DR} bias at CWKR (right). Bias is calculated by subtracting the gridded, bias-adjusted Z_{DR} at KBUF from the Z_{DR} at CWKR. Both datasets include points with $\text{KDE} \geq 2$. The modal bin is shaded red.	27
3.13 Gridded Z_{eH} comparison for 6 January 2015. Time-average of all admitted scans.	28
3.14 Gridded Z_{DR} comparison for 6 January 2015. Time-average of all admitted scans.	28
3.15 Direct comparisons for 6 January 2015. Dataset includes all admitted grid cells.	29
3.16 Histograms of Z_{DR} (left), Z_{DR} bias at CWKR (right). Bias is calculated by subtracting the gridded, bias-adjusted Z_{DR} at KBUF from the Z_{DR} at CWKR. Both datasets include points with $\text{KDE} \geq 2$. The modal bin is shaded red.	30
3.17 Gridded Z_{eH} comparison for 7 January 2015. Time-average of all admitted scans.	31
3.18 Gridded Z_{DR} comparison for 7 January 2015. Time-average of all admitted scans.	31
3.19 Direct comparisons for 7 January 2015. Dataset includes all admitted grid cells.	32
3.20 Histograms of Z_{DR} (left), Z_{DR} bias at CWKR (right). Bias is calculated by subtracting the gridded, bias-adjusted Z_{DR} at KBUF from the Z_{DR} at CWKR. Both datasets include points with $\text{KDE} \geq 2$. The modal bin is shaded red.	33
3.21 Gridded Z_{eH} comparison for 6 February 2015. Time-average of all admitted scans.	34

3.22 Gridded Z_{DR} comparison for 6 February 2015. Time-average of all admitted scans.	34
3.23 Direct comparisons for 6 February 2015. Dataset includes all admitted grid cells.	35
3.24 Histograms of Z_{DR} (left), Z_{DR} bias at CWKR (right). Bias is calculated by subtracting the gridded, bias-adjusted Z_{DR} at KBUF from the Z_{DR} at CWKR. Both datasets include points with KDE ≥ 2 . The modal bin is shaded red.	36
3.25 Gridded Z_{eH} comparison for 14 February 2015. Time-average of all admitted scans.	37
3.26 Gridded Z_{DR} comparison for 14 February 2015. Time-average of all admitted scans.	37
3.27 Direct comparisons for 14 February 2015. Dataset includes all admitted grid cells.	38
3.29 Gridded Z_{eH} comparison for 18 February 2015. Time-average of all admitted scans.	39
3.28 Histograms of Z_{DR} (left), Z_{DR} bias at CWKR (right). Bias is calculated by subtracting the gridded, bias-adjusted Z_{DR} at KBUF from the Z_{DR} at CWKR. Both datasets include points with KDE ≥ 2 . The modal bin is shaded red.	40
3.30 Gridded Z_{DR} comparison for 18 February 2015. Time-average of all admitted scans.	40
3.31 Direct comparisons for 18 February 2015. Dataset includes all admitted grid cells.	41

3.32 Histograms of Z_{DR} (left), Z_{DR} bias at CWKR (right). Bias is calculated by subtracting the gridded, bias-adjusted Z_{DR} at KBUF from the Z_{DR} at CWKR. Both datasets include points with $\text{KDE} \geq 2$. The modal bin is shaded red.	42
3.33 Gridded Z_{eH} comparison for 10 February 2016. Time-average of all admitted scans.	43
3.34 Gridded Z_{DR} comparison for 10 February 2016. Time-average of all admitted scans.	43
3.35 Direct comparisons for 10 February 2016. Dataset includes all admitted grid cells.	44
3.36 Histograms of Z_{DR} (left), Z_{DR} bias at CWKR (right). Bias is calculated by subtracting the gridded, bias-adjusted Z_{DR} at KBUF from the Z_{DR} at CWKR. Both datasets include points with $\text{KDE} \geq 2$. The modal bin is shaded red.	45
3.37 Gridded Z_{eH} comparison for 15 December 2016. Time-average of all admitted scans.	46
3.38 Gridded Z_{DR} comparison for 15 December 2016. Time-average of all admitted scans.	46
3.39 Direct comparisons for 15 December 2016. Dataset includes all admitted grid cells.	47
3.40 Histograms of Z_{DR} (left), Z_{DR} bias at CWKR, determined by subtracting the gridded, bias adjusted Z_{DR} at KBUF from the Z_{DR} at CWKR. Both datasets include points with $\text{KDE} \geq 2$. The modal bin is shaded red.	48

3.41 Scatter-plots of CWKR versus KBUF grid analyzed reflectivity, with Kernel Density Estimation shading. The red line is an Orthonormal Linear Regression, with a black identity line.	49
3.42 Comparison of gridded Z_{DR} with Gaussian ($\sigma = 3$) smoothed contours of Z_{eH} for 18 January 2014. Z_{DR} is constrained by only including points with a $KDE \geq 2$	51
3.43 Comparison of gridded Z_{DR} with Gaussian ($\sigma = 3$) smoothed contours of Z_{eH} for 23 January 2014. Z_{DR} is constrained by only including points with a $KDE \geq 2$	52
3.44 Comparison of gridded Z_{DR} with Gaussian ($\sigma = 3$) smoothed contours of Z_{eH} for 6 January 2014. Z_{DR} is constrained by only including points with a $KDE \geq 2$	53
3.45 Comparison of gridded Z_{DR} with Gaussian ($\sigma = 3$) smoothed contours of Z_{eH} for 7 January 2014. Z_{DR} is constrained by only including points with a $KDE \geq 2$	54
3.46 Comparison of gridded Z_{DR} with Gaussian ($\sigma = 3$) smoothed contours of Z_{eH} for 10 February 2016. Z_{DR} is constrained by only including points with a $KDE \geq 2$	55
3.47 Comparison of gridded Z_{DR} with Gaussian ($\sigma = 3$) smoothed contours of Z_{eH} for 1 February 2014. Z_{DR} is constrained by only including points with a $KDE \geq 2$, and is bias-adjusted using the offset calculated in the first section of Chapter 3.	56
3.48 Comparison of gridded Z_{DR} with Gaussian ($\sigma = 3$) smoothed contours of Z_{eH} for 6 February 2015. Z_{DR} is constrained by only including points with a $KDE \geq 2$, and is bias-adjusted using the offset calculated in the first section of Chapter 3.	57

3.49 Comparison of gridded Z_{DR} with Gaussian ($\sigma = 3$) smoothed contours of Z_{eH} for 14 February 2015. Z_{DR} is constrained by only including points with a KDE ≥ 2 , and is bias-adjusted using the offset calculated in the first section of Chapter 3.	58
3.50 Comparison of gridded Z_{DR} with Gaussian ($\sigma = 3$) smoothed contours of Z_{eH} for 18 February 2015. Z_{DR} is constrained by only including points with a KDE ≥ 2 , and is bias-adjusted using the offset calculated in the first section of Chapter 3.	59
3.51 Comparison of gridded Z_{DR} with Gaussian ($\sigma = 3$) smoothed contours of Z_{eH} for 15 December 2016. Z_{DR} is constrained by only including points with a KDE ≥ 2 , and is bias-adjusted using the offset calculated in the first section of Chapter 3.	60
4.1 Gate-by-gate idealized beam volume comparison along a straight line between radars, assuming Gaussian beam functions.	62
4.2 Comparison of the range of Z_{DR} (max-min) values observed for each case, with biased cases depicted with yellow triangles and unbiased as green dots.	64
A.1 500mb Geopotential Height at 06Z 18 January 2014.	70
A.2 500mb Geopotential Height at 06Z 23 January 2014	71
A.3 500mb Geopotential Height at 18Z 1 February 2014.	72
A.4 500mb Geopotential Height at 15Z 6 January 2015.	73
A.5 500mb Geopotential Height at 09Z 7 January 2015.	74
A.6 500mb Geopotential Height at 09Z 6 February 2015.	75
A.7 500mb Geopotential Height at 12Z 14 February 2015.	76
A.8 500mb Geopotential Height at 21Z 18 February 2015.	77

A.9 500mb Geopotential Height at 18Z 10 February 2016.	78
A.10 500mb Geopotential Height at 09Z 15 December 2016.	79
A.11 SkewT/Log-P Chart from the BUF Radiosonde launched at 12Z 18 January 2014	80
A.12 SkewT/Log-P Chart from the BUF Radiosonde launched at 00Z 23 January 2014	81
A.13 SkewT/Log-P Chart from the BUF Radiosonde launched at 12Z 1 February 2014	82
A.14 SkewT/Log-P Chart from the BUF Radiosonde launched at 00Z 6 January 2015	83
A.15 SkewT/Log-P Chart from the BUF Radiosonde launched at 12Z 7 January 2015	84
A.16 SkewT/Log-P Chart from the BUF Radiosonde launched at 00Z 6 February 2015	85
A.17 SkewT/Log-P Chart from the BUF Radiosonde launched at 12Z 14 February 2015	86
A.18 SkewT/Log-P Chart from the BUF Radiosonde launched at 00Z 18 February 2015	87
A.19 SkewT/Log-P Chart from the BUF Radiosonde launched at 12Z 10 February 2016	88
A.20 SkewT/Log-P Chart from the BUF Radiosonde launched at 12Z 15 December 2016	89
A.21 Sounding Precipitable Water Climatology for BUF	90

1 Chapter One

1.1 Introduction

Weather radar is an invaluable tool for nowcasting severe weather. In Canada, lake-effect snows are a severe weather event which have adverse impacts on a large sector of the population. While the current Canadian C-Band radar systems have been proven in this regard, there is some uncertainty with how the specifications of the new S-Band systems will translate to lake-effect snow forecasting. While no prototype system is available to test in the Great Lakes area, the next best stand-in to compare with are the current S-Band radars in the United States. King City radar (CWKR) has been compared with the Buffalo, NY radar (KBUF) previously by Boodoo et al. (2015), but this case was for deep, warm-season convection. Furthermore, C-Band radars have been compared with S-Band radars before in other locales, e.g (Abon et al. 2014; Kernen et al. 2008), however polarimetric variables were not numerically compared on a large-scale. Our experimental setup is unique in that the radars are not co-located, in contrast with other research centers such as the University of Alabama Huntsville, where a research C-Band radar is several kilometer away from a WSR-88D (Petersen et al. 2007). With Lake Ontario in between CWKR and KBUF, this creates the opportunity to analyze a vast amount of incident sample volumes from lake-effect snow events. The one downfall is the addition of uncertainty stemming from differing elevation angles and beamwidths

of the radars. In order to accurately compare the two radars, the data is objectively analyzed. Radar data objective analysis is most prominently used to create mosaics of multiple radars for projects such as the National Severe Storm Laboratory’s Multi-Radar Multi Sensor in the U.S. (Zhang et al. 2016). It is also used extensively for research purposes, including studying snow squalls (Mulholland et al. 2017). The goal of this study is to show that there will be no loss in quality of radar observations for the purposes of nowcasting lake-effect snow with S-Band radar. Another goal is to directly compare polarimetric moments, which has not been done in this manner before, and identify any biases. It is important to remove biases as no amount of spatial or temporal smoothing will remove them. With bias-adjusted values from two independent sources, a high-confidence conclusion can be made on the types of hydrometeors present in the common sampling volumes. Although polarimetric (dual-pol) radar has matured within the research community, operational deployment has been a much slower process. Many studies have been undertaken in regards to quantitative precipitation estimation using dual-pol variables for rainfall, but studies involving snow have been much more limited. Findings here should increase confidence in comparing dual-polarimetric at two different wavelengths, and demonstrate the information rich nature of these variables.

1.2 Background

First, it is important to provide some background on the weather radar moments that are presented in this study, from both single and dual polarized signals. The convention for representing these moments symbolically hereafter is lower-case subscript for linear units and upper-case subscript for logarithmic units, i.e. Z_{DR} is logarithmic while Z_{dr} is linear.

1.2.1 Radar Locations

In Canada, there is one active C-Band weather radar with dual-pol capabilities. It is located north of Toronto, in King City, while the rest of the network is currently undergoing an upgrade to polarimetric S-Band. Its neighbor to the south, KBUF, was upgraded to dual-pol in 2012 as part of a network wide upgrade. The terms C-Band and S-Band are in reference to the frequency band in which a radar operates, thereby determining the wavelength they transmit. Figure 1.1 shows the geographic

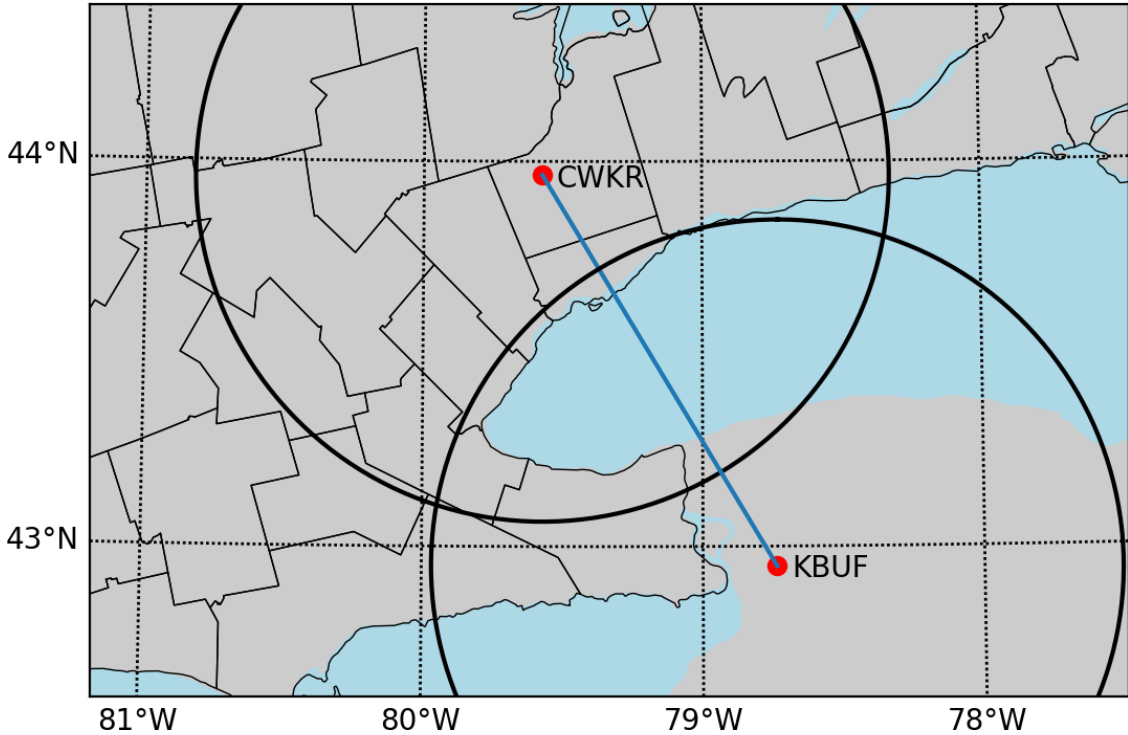


Figure 1.1: The location of the NWS Buffalo Radar (KBUF) and King City Radar (CWKR) are shown as red dots, with a 100 km range ring around each. The distance between the two, drawn as a blue line, is 131.5 km.

location of the radar sites in comparison with each other.

1.2.2 Equivalent Reflectivity Factor (Z_h)

The foremost moment derived from radar is the reflectivity factor (Z_h), where the subscript denotes its derivation from the horizontally polarized signal. This variable measures the number density $N(D)$ of hydrometeors of diameter D per unit volume, as presented in Equation 1.1. Due to uncertainties about what type of target is actually doing the scattering, it is typically represented as the equivalent reflectivity factor Z_{eh} , where $Z_h = Z_{eh}$ if the targets are made of liquid water and are comparatively small to the wavelength (Fabry 2015). The two names are essentially interchangeable, but the nomenclature *equivalent* reflectivity factor will be used in this study to acknowledge the presence of non-ideal targets, e.g. ice crystals/snow.

$$Z_{eh} \approx Z_h = \int_0^{\infty} N(D) D^6 dD \text{ (mm}^6/\text{m}^3\text{)} \quad (1.1)$$

1.2.3 Differential Reflectivity (Z_{dr})

Radar equipped with dual-pol capabilities are still an emerging technology, in terms of operational meteorological applications. These types of radar systems are capable of transmitting and receiving two orthogonally polarized electromagnetic waves in order to deduce more information about the microphysical structure of hydrometeors. One of the main variables this allows them to produce is Z_{DR} , defined as the ratio of the horizontal channel reflectivity (Z_H) to the vertical channel reflectivity (Z_V). This can be simplified to the difference between the two using the logarithmic quotient rule, since they are represented in logarithmic units. Equation 1.2 demonstrates this concept.

$$Z_{dr} = 10 * \log_{10}\left(\frac{Z_H}{Z_V}\right) = Z_h - Z_v \quad (1.2)$$

1.2.3.1 Interpretations of Z_{DR} in Snow

In snowfall, Z_{DR} can be a powerful tool for deducing the predominant crystal habit and type. Ranges of Z_{DR} are typically given in the literature for characterizing hydrometeors, and vary due to their semi-empirical nature. The most widely cited synthesis paper by Straka et al. (2000) reports that dry aggregated snow at cold temperatures range from $0 < Z_{DR} < 0.2$ dB, while pristine ice crystals and lightly aggregated crystals range from $0.4 < Z_{DR} < 3$ dB, both for a range of Z_{eH} of $5 < Z_{eH} < 30$ dBZ. Fabry (2015) reports slightly different ranges in Figure 1.2, and gives ranges for other targets beyond the scope of this study; hydrometeors that are sufficiently frozen are only considered in this study.

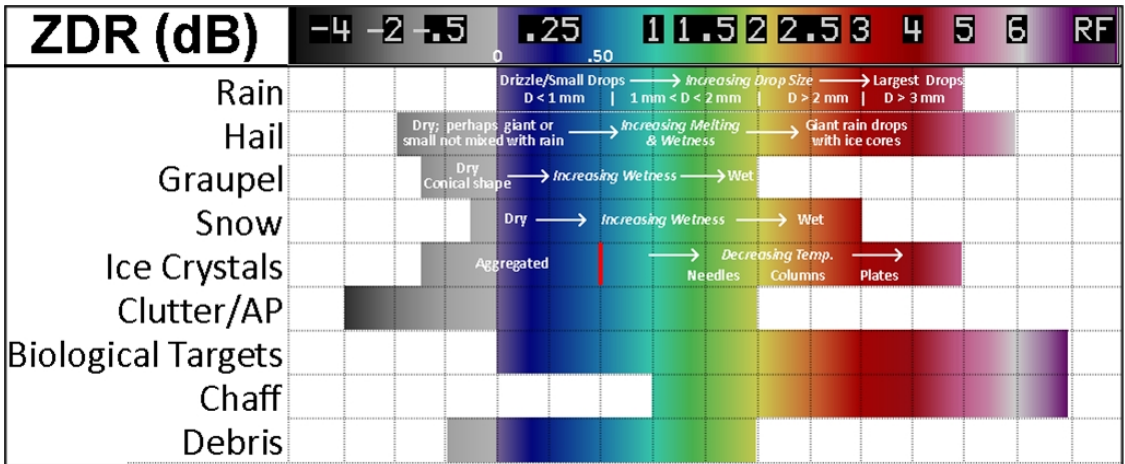


Figure 1.2: Chart of expected ranges of Z_{DR} for a variety of targets. Taken from Fabry (2015).

1.2.4 Co-polar Cross-Correlation Coefficient (ρ_{hv})

With the advent of Simultaneous Transmit and Receive (STAR) radar systems, which both radars used here have, it is possible to perform the zero time-lag cross-

correlation between the time series data obtained from horizontal and vertical channels. This is known as the Co-polar Cross-Correlation Coefficient (ρ_{hv}) in radar meteorology, and ranges from 0 to 1. Low values indicate pulse volumes containing heterogeneities, while a value of 1 indicates matching, homogenous volumes. For an ensemble of scatters, Equation 1.3 defines the backscattering matrix used in the definition of ρ_{hv} in Equation 1.4, as defined by Ryzhkov and Zrnić (2007).

$$\mathbf{S} = \begin{bmatrix} S_{hh} & S_{hv} \\ S_{hv} & S_{vv} \end{bmatrix} \quad (1.3)$$

$$\rho_{hv} = \frac{\langle S_{vv} S_{hh}^* \rangle}{\sqrt{\langle S_{hh}^2 \rangle \langle S_{vv}^2 \rangle}} \quad (1.4)$$

1.2.4.1 Interpretations of ρ_{hv} in Snow

Contamination from clutter and other non-meteorological targets can be filtered by using a ρ_{hv} threshold of 0.95, as suggested by Straka et al. (2000). Using this threshold can also be used to avoid Mie scatters, which becomes a bigger problem at C-Band wavelengths Fabry (2015).

2 Chapter Two

2.1 Methodology

2.1.1 Comparison of Radar Systems

Comparing two radar datasets is fraught with challenges; solutions to meet this challenge are presented herein. Even though the radar system characteristics are not identical, the measurements are comparable due to the design of the weather radar equation, which accounts for the sensitivity of the radar system itself (Rogers and Yau 1989). The area of study was chosen to ensure that the coinciding radar scans had similar resolution samples and beam heights. Lake Ontario happens to be the perfect area to bound between the radars, therefore only data from areas over water inside the bounding box depicted in Figure 2.1 are used. This also ensures that no ground clutter is incorporated into the analyses.

2.1.1.1 Comparing Radar Characteristics

As presented in Equation 2.1, the weather radar equation is defined by constant parameters dependent on the radar system characteristics, and varying properties related to the target. This equation determines the theoretical mean power (\bar{P}_r)

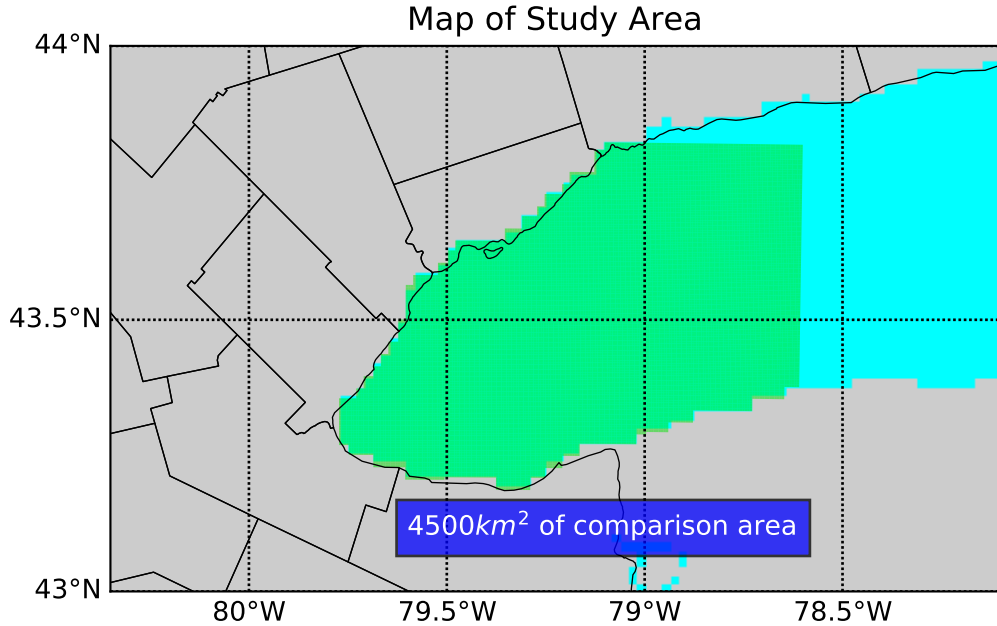


Figure 2.1: Bounding box of the study area, denoted by the green shading.

that should be returned to the radar receiver.

$$\bar{P}_r = \frac{\pi^3 c}{1024 \ln(2)} \left[\frac{P_t \tau G^2 \theta^2}{\lambda^2} \right]_{dBZ_0} \left[|K_w|^2 \frac{Z_{eh}}{r^2} \right]_{TARGET} \quad (2.1)$$

The target properties are dielectric constant (K), range (r) and equivalent reflectivity factor Z_{eh} . Conversely, the radar parameters ideally remain unchanged from their values upon installation of the radar system. These parameters form the radar constant, symbolically expressed as dBZ_0 . The parameters that define this constant include the power transmitted (P_t), the pulse length (τ), the antenna gain (G), the angular beamwidth (θ), and the wavelength (λ).

$$10 \log Z_H = 10 \log \bar{P}_r + 20 \log r - dBZ_0 \quad (2.2)$$

Equation 2.2 shows how dBZ_0 is subtracted out from the full calculation of Z . This means that values from two different systems are comparable, as the contributions to the returned power intrinsic to the radar are negated. Next, Table 2.1 compares

parameters for both radar systems. The biggest difference between the two is the wavelength, with CWKR operating in the C frequency band and KBUF operating in the S frequency band. It should be noted that although KBUF has a larger physical beamwidth than CWKR, it achieves an effective azimuthal resolution of 0.5° through an over-sampled data windowing technique (Torres and Curtis 2007). Therefore, the two radars are matched in azimuthal resolution, while CWKR has twice the range resolution of KBUF. Also, it should be stated that the signal processors used in both radar systems are in the Vaisala SIGMET series, therefore they measure Z_{eH} and Z_{DR} using 8 bit resolution. For Z_{eH} , the data intervals of -31.5 dBZ to +95.5 dBZ yield a data resolution of 0.5 dBZ. For Z_{DR} , an interval of -7.94 dB to +7.94 dB yields a resolution of 0.0625 dB.

Table 2.1: Specifications of each radars system, with symbols as used in Eq. 2.2. Pulse Length is specified as short pulse/long pulse

field [symbol](unit)	King City (CWKR)	Buffalo (KBUF)
Wavelength [λ](cm)	5 (C-Band)	10 (S-Band)
Beamwidth [θ] ($^\circ$)	0.62	0.92
Antenna Gain [G] (dB)	45.5	49.2
Transmitter Peak Power (kW)	250	1000
Pulse Length [τ] (μs)	0.8/2.0	1.5/4.5
Matched Elevation Angle ($^\circ$)	0.2	0.5
Range Resolution [r] (m)	125	250

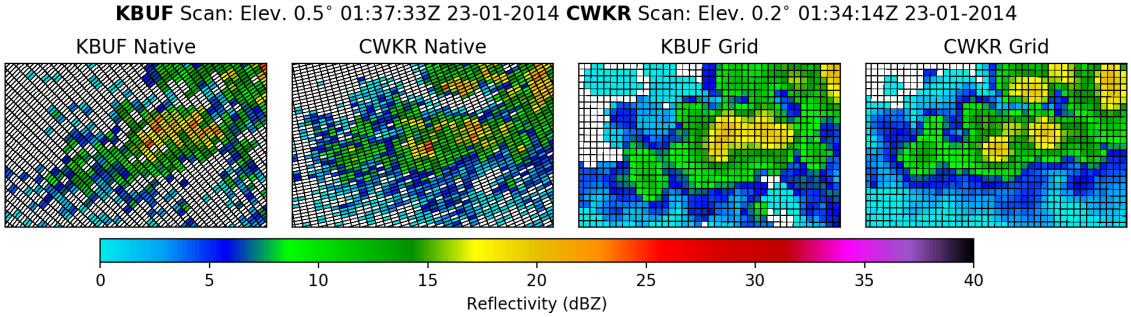
2.1.2 Distance-Weighting Scheme

The biggest challenge when comparing radar resolution volumes measured by radars that are not co-located is resolving the differences in coordinate system. A resolution volume is defined as volume irradiated by the idealized Gaussian beam pattern for each range gate, otherwise known as a bin. Resolution volumes are sampled natively in the spherical coordinate system; although there may be some overlap, the shape of the bins will vary drastically. Differences between KBUF and CWKR bin geometry can be ascertained from Figure 2.2. These differences require the radar data to be objectively analyzed onto a common coordinate system, which can be achieved through a distance-weighting scheme. This method was adopted in the open source software module called the Python ARM Radar Toolkit (Py-ART) (Helmus and Collis 2016), which is used here. In accordance with the recommendations of Pauley and Wu (1990), a grid resolution ($\Delta x, \Delta y$) of 500 meters is chosen. A Barnes distance-weighting scheme is used for this analysis.

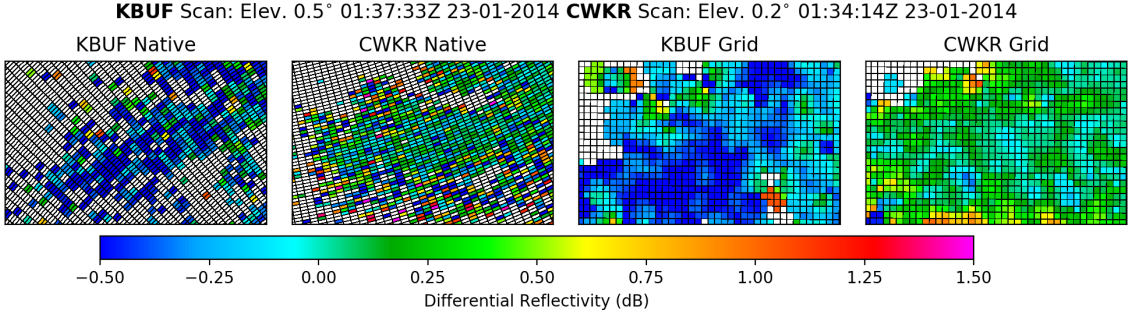
$$f'_p = \sum_{b=1}^n e^{-(d_b/\kappa)^2} f_q / \sum_{b=1}^n e^{-(d_b/\kappa)^2} \quad (2.3)$$

The Gaussian weighting function used in said scheme is given in Equation 2.3. It shows that the value of the analysis at some point p is equal to sum of weights convolved with the actual values at bin b in radar space, divided by the sum of the weights. The summation is performed over n number of bins that are within the radius of influence (κ) of the center point of the grid cell, and d is the horizontal distance from the native bin to the center point of the cell. Vertical distance is neglected, as only the lowest elevation angle from the radars are included for comparison.

$$\kappa = D * \tan \theta \quad (2.4)$$



(a) Z_H comparison, shows the transformation from a smooth input to smooth gridded output.



(b) Z_{DR} comparison, in contrast with (a), shows the limitations of representing an non-linear field with an isotropic distance-weighting function.

Figure 2.2: Base moment comparisons between radars over Lake Ontario, with dimensions of 20x12.5 km. Left panels are in native radars coordinates, with gates outlined in black. Right panels are transformed to a common Cartesian grid, with grid cells outlined in black.

The definition of κ is found in Equation 2.4, where D is the horizontal distance from the grid cell to the radar and θ is the angular beamwidth. This completes the framework for comparing the radar datasets in this study.

2.2 Selection of Cases

Cases selected for this study were chosen entirely based on the pattern of motion and banding of the radar echoes. Radar mosaics for the study area were manually examined, beginning in 2014. When time intervals with echoes in the study area were observed, it was noted whether they moved repeatedly over the same area, or were progressive. Also, it was noted whether they exhibited meso- β length scales (\sim 20 km wide), or synoptic length scales (> 200 km) (Orlanski 1975). The narrow bands that moved over the same area were classified as lake-effect driven events, while the progressive, wide-areas of precipitation are classified as synoptically driven events. A tabulation of important level temperatures for the five lake-effect snow events selected is shown in Table 2.2, along with the time interval during which radar scans were chosen. Synoptic events are given in Table 2.3. This indicates that all events were sufficiently below freezing, and dry snow/ice crystals were the predominant hydrometeor type.

Table 2.2: Temperatures at two important levels from radiosonde launched closest in time to the selected lake-effect snow events, with the time interval during which radar scans were chosen.

BUF - Radiosonde	Radar Times	850mb T ($^{\circ}$ C)	Sfc. T ($^{\circ}$ C)
2014-01-23 00Z	0100-1000Z	-22.5	-14.9
2015-01-06 12Z	1200-1700Z	-20.1	-11.7
2015-02-14 12Z	1000-1400Z	-14.9	-6.9
2015-02-18 12Z	2100-2359Z	-17.3	-10.1
2016-02-10 12Z	1300-2359Z	-10.5	-2.7

Table 2.3: Temperatures at two important levels from radiosonde launched closest in time to the selected synoptic snow events, with the time interval during which radar scans were chosen.

KBUF - Radiosonde	Radar Times	850mb T ($^{\circ}$ C)	Sfc. T ($^{\circ}$ C)
2014-01-18 12Z	0600-0800Z	-11.3	-6.5
2014-02-01 12Z	1500-1800Z	-4.7	-3.1
2015-01-07 12Z	0900-1100Z	-19.5	-10.1
2015-02-06 12Z	0900-1030Z	-16.3	-10.7
2016-12-15 12Z	0920-1020Z	-20.3	-12.3

2.3 Filtering Conditions

Several conditions were used to narrow down the selected sets to the best suited scans and individual gates for admission into the distance-weighting scheme.

2.3.1 Time Filter

Scan start times are compared between the radars, and if they are within four minutes of each other, the pair is admitted. For CWKR, there is a regular volume update frequency of ten minutes, while KBUF is variable based on the Volume Coverage Pattern (VCP) selected by the operator. The update frequency could be as short as every two minutes if the operator has activated Supplemental Adapative Intra-Volume Low-Level Scans (SAILS) mode.

2.3.2 Gate Filters

Several gate filters were used to ensure the highest data quality possible. Gates with $\rho_v < 0.95$ were excluded to filter for dry snow and crystals only. A manual inspection of all cases was made, and the range of Z_{DR} in all cases lay within $-0.5 < Z_{DR} < 1.5$ dB. Therefore, Z_{DR} values outside this range were filtered to avoid contamination from beam blockages, etc. Finally, gates over land were filtered, to avoid ground clutter contamination.

2.4 Advanced Statistical Techniques

Scatter plots directly comparing grid cells produced by the distance-weighting scheme are used in this study. This section discusses how advanced statistical techniques were leveraged to derive the most information from these plots, and also reduce the error intrinsic to the variables for quantitative analysis.

2.4.1 Bi-Variate Kernel Density Estimation

Both radar datasets contain a similar amount of measurement and analysis error. Furthermore, scatter-plots containing on the order of 10^5 points become overwhelming to visually analyze. To solve this problem, a bi-variate Kernel Density Estimation (KDE) technique is used. A 2-D KDE is a technique that estimates the joint probability density function between two random variables (Silverman 1986). The two variables compared in this study are the matched observations made by the two radars. Equation 2.5 gives a full definition of this estimate, where \mathbf{x} is the matrix of matched observations, \mathbf{H} is the 2x2 bandwidth (smoothing) matrix, and \mathbf{K} is the kernel function. Scott (1992) suggests a rule of thumb for calculating the bandwidth matrix, shown in Equation 2.6, where n is the number of points

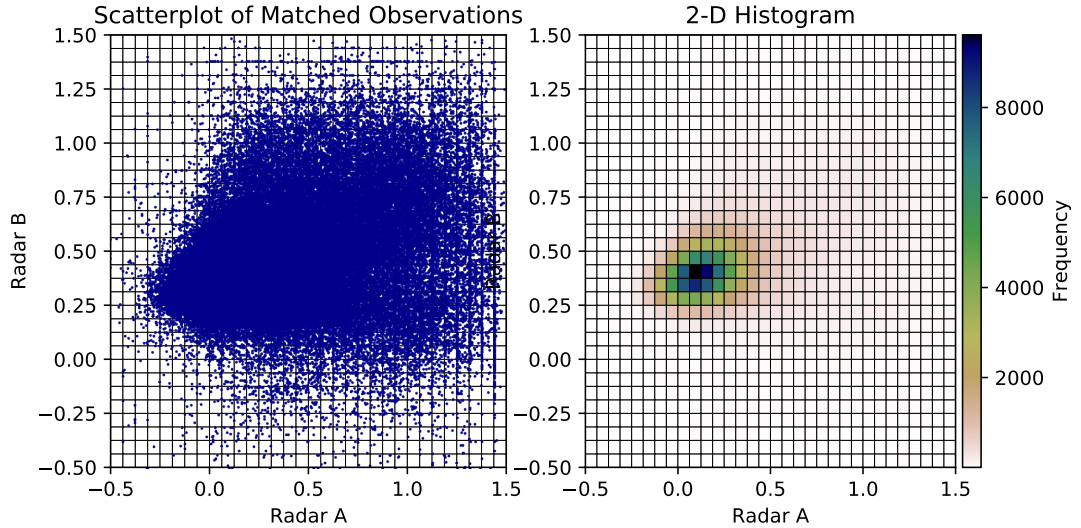


Figure 2.3: Scatter-plot of matched points illustrating the high density of the points (left). The total of points in this figure are 147,457. 2-D histogram of the same matched points, binned to native data resolution (right).

and σ is the standard deviation. The kernel function is chosen as 2-D Gaussian throughout, given as Equation 2.7, where the terms retain their prevailing meaning. Figure 2.3 demonstrates the motivation and the discrete version of this method, a 2-D histogram of the data. The units of the KDE can be thought of as a likelihood ratio.

$$\hat{f}_{\mathbf{H}}(\mathbf{x}) = \frac{1}{n} \sum_{i=1}^n \mathbf{K}_{\mathbf{H}}(\mathbf{x} - \mathbf{x}_i) \quad (2.5)$$

$$\mathbf{H} = \sigma * n^{-1/3} \quad (2.6)$$

$$\mathbf{K}_{\mathbf{H}}(\mathbf{x}) = \mathbf{H} * 2\pi * e^{-\frac{1}{2}\mathbf{x}^T \mathbf{H}^{-1} \mathbf{x}} \quad (2.7)$$

2.4.2 Orthonormal Linear Regression

A hallmark of this study is the lack of ground truth. The sample sets compared contain error prone, independent variables. Typically, scatter-plots compare an independent variable to a dependent variable. Instead of performing a standard linear regression between the variables, an orthonormal linear regression is used. This type of regression allows for error in both variables, by performing the least squares regression perpendicular to the initial fit instead of vertically (Markovsky and Huffel 2007). Figure 2.4 demonstrates this concept.

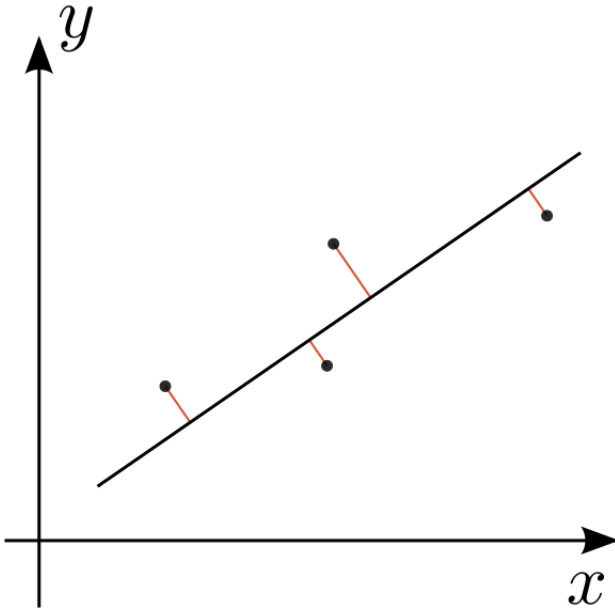


Figure 2.4: Demonstration of an Orthonormal Linear Regression

2.5 Z_{DR} Bias Estimation

Although it is not possible to check absolute calibration of Z_H when comparing two radars, it is possible to verify Z_{DR} calibration due to relative nature of the quantity (Zrnić et al. 2006). While radars are regularly calibrated using internal calibration

procedures, an external check is useful for monitoring the time-varying component of calibration. The typical process for calibration of Z_{DR} is pointing the antenna to zenith and performing “bird bath” scans during light rain events (Hubbert and Pratte 2006). The Z_{DR} in light rain is expected to be 0 dB, therefore any offset from this is considered a bias; The signal processor subtracts out this bias to achieve the final output. Due to mechanical constraints, NEXRAD radars are unable to perform this procedure, but CWKR is. NEXRAD radars disseminate a product which contains an estimate of Z_{DR} bias using the intrinsic properties of dry snow Zittel et al. (2015). The daily published offset will be used to adjust Z_{DR} values obtained from KBUF to diagnose any bias at CWKR. Under normal conditions, Z_{DR} can be calibrated within 0.1 dB (Zrnić et al. 2006). This error threshold is adopted in this study.

3 Chapter Three

3.1 Event Comparisons

Now, we consider each of the selected events individually, demonstrating that the events were classified correctly, and breaking down the results from each case. Although it is nearly impossible to extricate lake influence from synoptically classified events, synoptic-scale ascent is considered the characterizing factor. Classification of the synoptic pattern during each event are based on interpretations of data given in Appendix A. These descriptions are ancillary to the study and are provided to demonstrate a variety of patterns are represented.

3.1.1 18 January 2014 - Synoptic

In this event, a weak shortwave is approaching Southern Ontario as it rounds the base of a longwave trough centered over the Eastern US. With the study area in the attendant region of upper-level divergence, and a moist column present through 500mb, scattered snow showers form ahead of the shortwave. Figure 3.1 depicts similiar cellular patterns between radars in the time-averaged Z_{eH} field. In contrast, the Z_{DR} comparison in Figure 3.2 shows that although the fields are similiar in their heterogeneity, the spatial matching between the two is tenuous everywhere but in the heaviest showers.

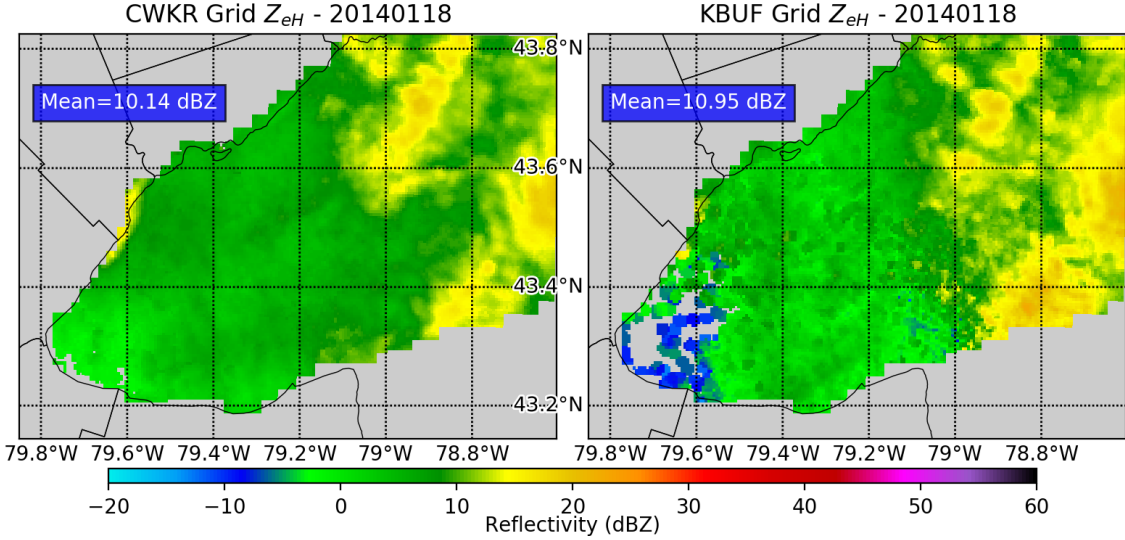


Figure 3.1: Gridded Z_{eH} comparison for 18 January 2014. Time-average of all admitted scans.

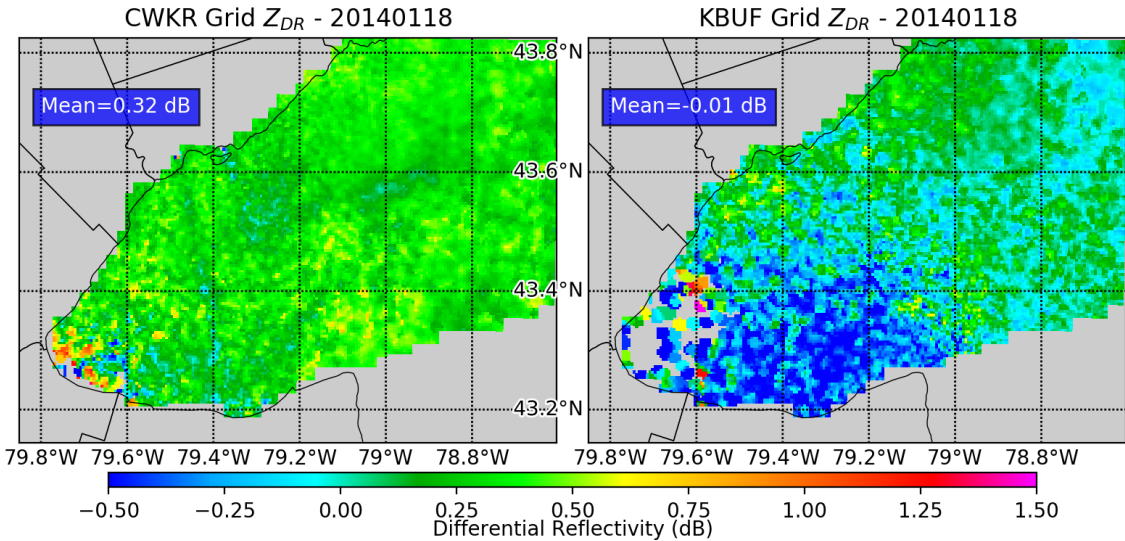


Figure 3.2: Gridded Z_{DR} comparison for 18 January 2014. Time-average of all admitted scans.

To investigate further, we examine a scatter-plot directly comparing matched values between radars. Artifacts are present in both moments in Figure 3.3, indicated by evenly spaced vertical lines; these indicate an anomaly originating from the axis the lines are normal to. These anomalies are likely related to the transmit and receive errors KBUF reported throughout the month of January 2014, i.e. calibration issues. For Z_{eH} , Figure 3.3a shows that artifacts are no longer present for values greater than 15 dBZ, which indicates that a stronger weather signal leads to better matching. On the contrary, Figure 3.3b shows that for Z_{DR} , artifacts are present throughout. Also, the distribution of Z_{DR} is unimodal, which indicates one predominant hydrometeor type.

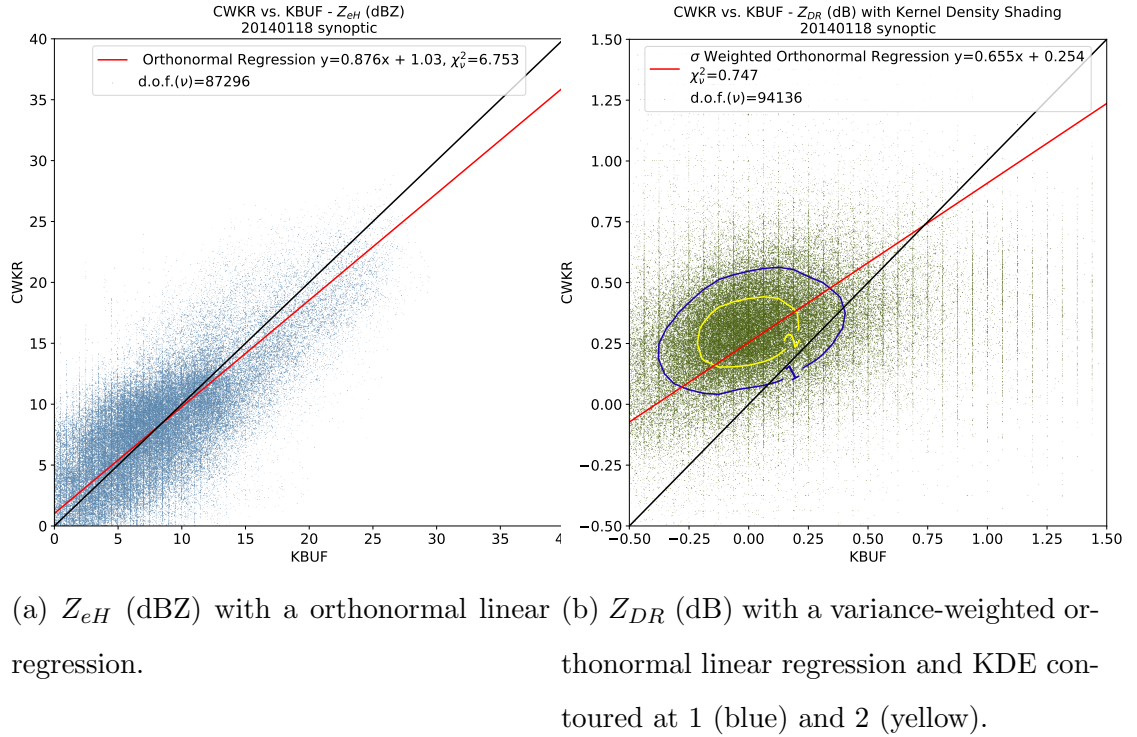


Figure 3.3: Direct comparisons for 18 January 2014. Dataset includes all admitted grid cells.

It is still possible to extract a signal from the noise and calibration issues, by subjectively selecting a KDE threshold of 2. Points with $\text{KDE} < 2$ are discarded, then the constrained set is used to resolve the bias present in Z_{DR} , as suggested by the comparisons. Figure 3.4 gives an estimate of the bias at CWKR by using the known bias at KBUF as provided by the NEXRAD External Target Bias Estimation technique. This method yields a median of -0.095 dB for the bias at CWKR, which is within the error threshold of ± 0.1 dB, indicating no discernible bias.

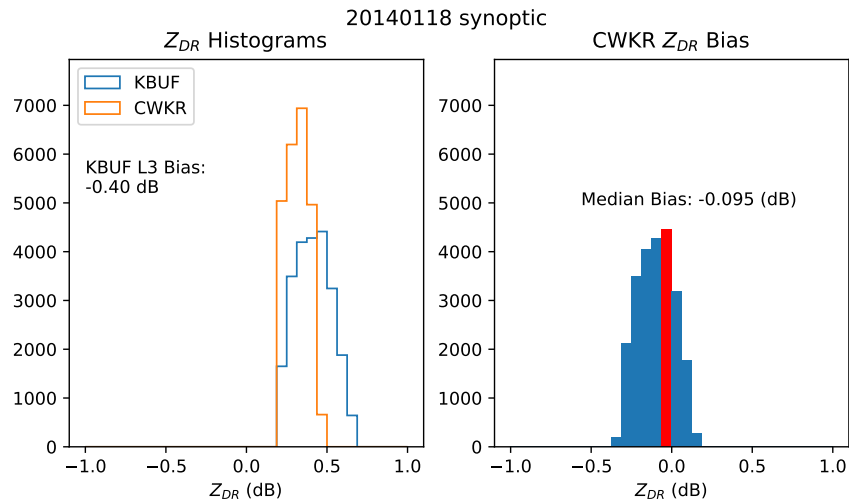


Figure 3.4: Histograms of Z_{DR} (left), Z_{DR} bias at CWKR (right). Bias is calculated by subtracting the gridded, bias-adjusted Z_{DR} at KBUF from the Z_{DR} at CWKR. Both datasets include points with $\text{KDE} \geq 2$. The modal bin is shaded red.

3.1.2 23 January 2014 - Lake-Effect

A positively tilted longwave trough dominates the eastern third of Canada during this event, with NW winds at 850mb and SW winds at the surface. This light flow pattern yields a single, heavy band depicted in Figure 3.5, colloquially referred to as “tea-kettle” lake-effect snow. There is also a background stream of very light

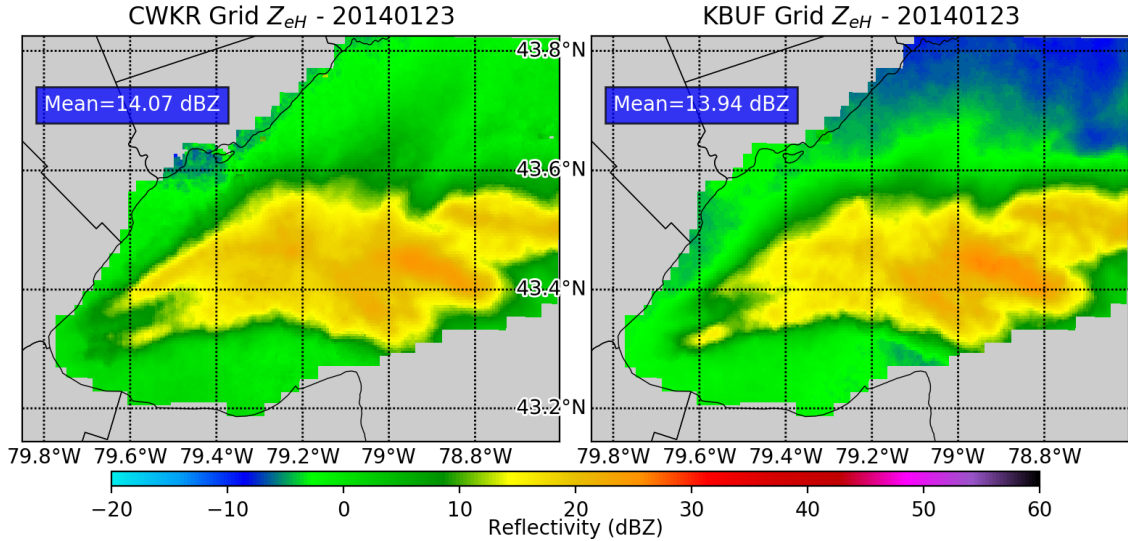


Figure 3.5: Gridded Z_{eH} comparison for 23 January 2014. Time-average of all admitted scans.

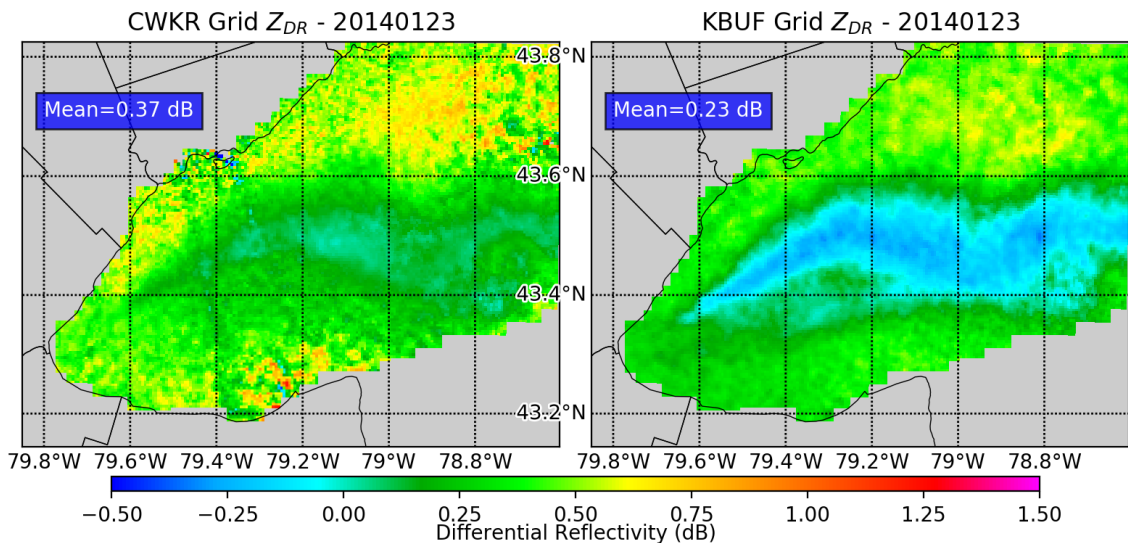


Figure 3.6: Gridded Z_{DR} comparison for 23 January 2014. Time-average of all admitted scans.

lake-effect snow impinging from Lake Erie. Spatial banding patterns of the lake-effect snow in the time-averaged Z_{eH} fields as compared between the radars are remarkably similar. The difference between the grid mean values is only 0.13 dBZ. Comparing Z_{DR} fields in Figure 3.6, the spatial matching is good, but a clear bias exists. Also, a speckled pattern is imparted on the Z_{DR} fields by the light snow from Lake Erie.

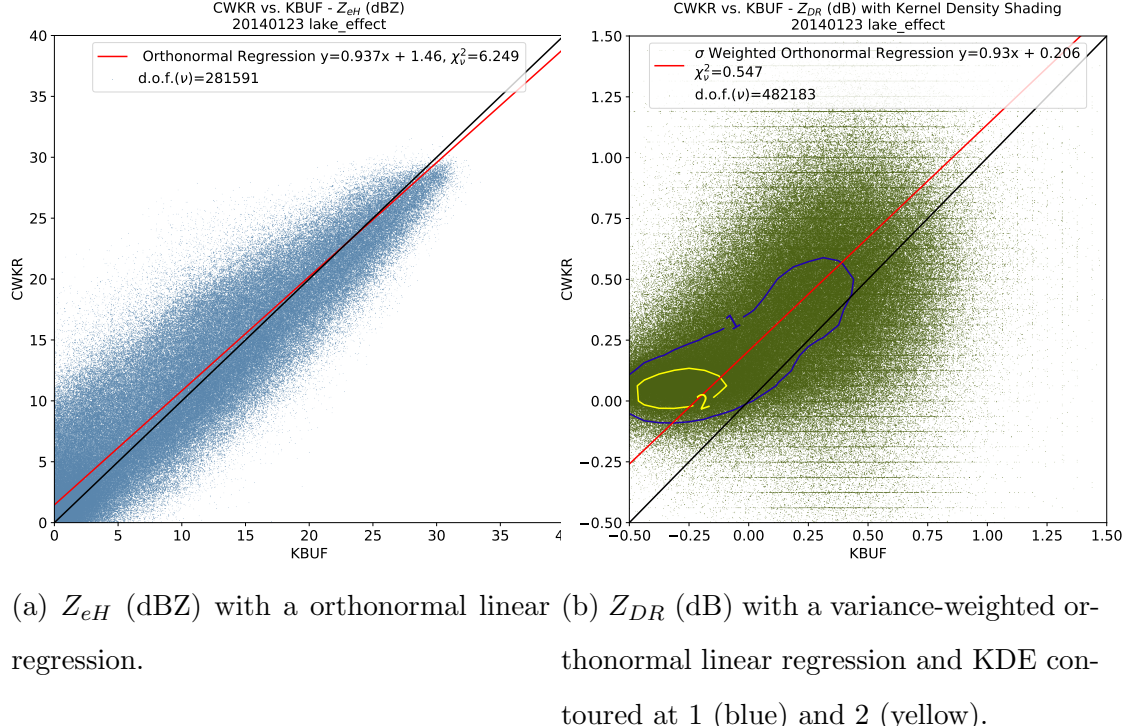


Figure 3.7: Direct comparisons for 23 January 2014. Dataset includes all admitted grid cells.

The scatter-plot in Figure 3.7a shows an analysis free of artifacts, and good agreement on average between radars. Although the agreement in Z_{eH} between radars as indicated by the orthonormal regression is acceptable, the χ^2_ν statistic indicates a high error variance. A slightly bi-modal distribution of Z_{DR} is shown in

Figure 3.7a, with the main peak near 0 dB and a secondary peak near 0.5 dB, with artifacts much more prevalent near the secondary peak. Both analysis methods have indicated a bias in Z_{DR} , so the KDE constraint method is used to estimate. Figure 3.8 gives an estimate of the bias at CWKR, with a median value of -0.055 dB. Once again, no discernible bias exists outside of the error threshold of ± 0.1 dB for this event.

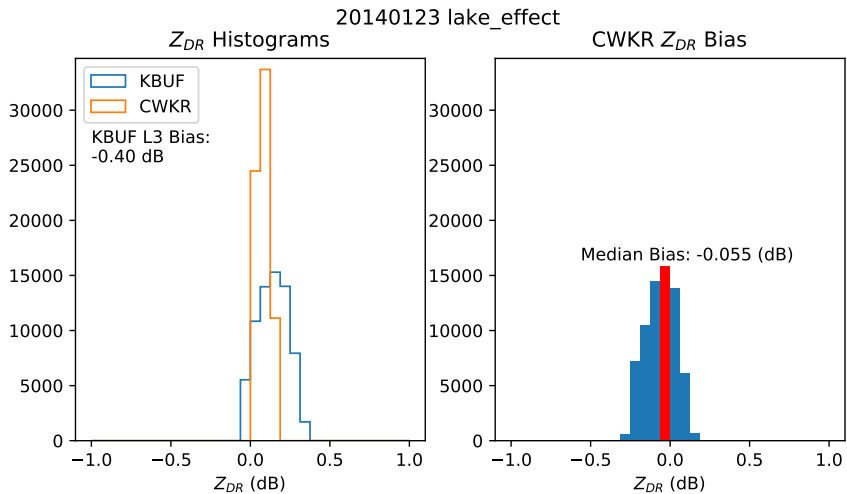


Figure 3.8: Histograms of Z_{DR} (left), Z_{DR} bias at CWKR (right). Bias is calculated by subtracting the gridded, bias-adjusted Z_{DR} at KBUF from the Z_{DR} at CWKR. Both datasets include points with $KDE \geq 2$. The modal bin is shaded red.

3.1.3 1 February 2014 - Synoptic

This event is characterized by strong SW flow aloft, with above average moisture content. This leads to widespread stratiform snow, with an eventual transition to rain outside of the time interval selected. A large swath of steady snow is depicted by the time-averaged Z_{eH} in Figure 3.9. Furthermore, Figure 3.10 shows smoother Z_{DR} fields as compared with other events, which confirms the stratiform nature of the precipitation. Next, Figure 3.11a indicates very good agreement in Z_{eH} with

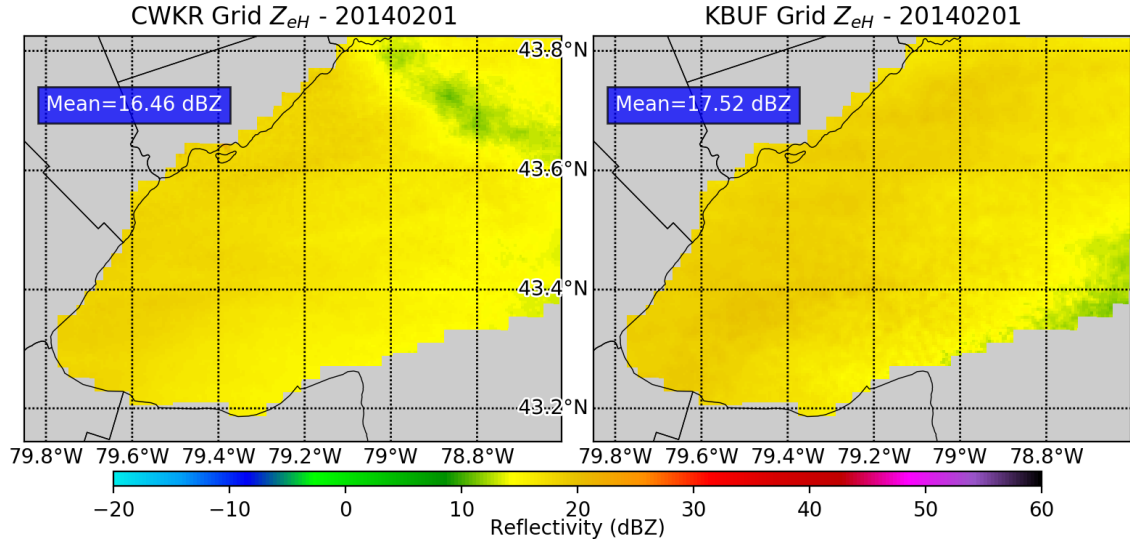


Figure 3.9: Gridded Z_{eH} comparison for 1 February 2014. Time-average of all admitted scans.

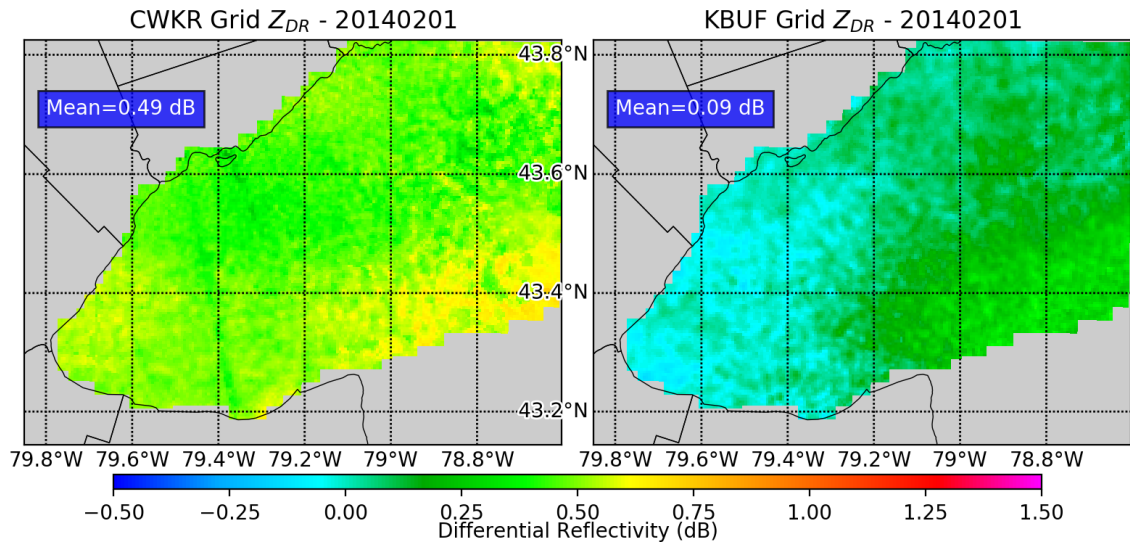
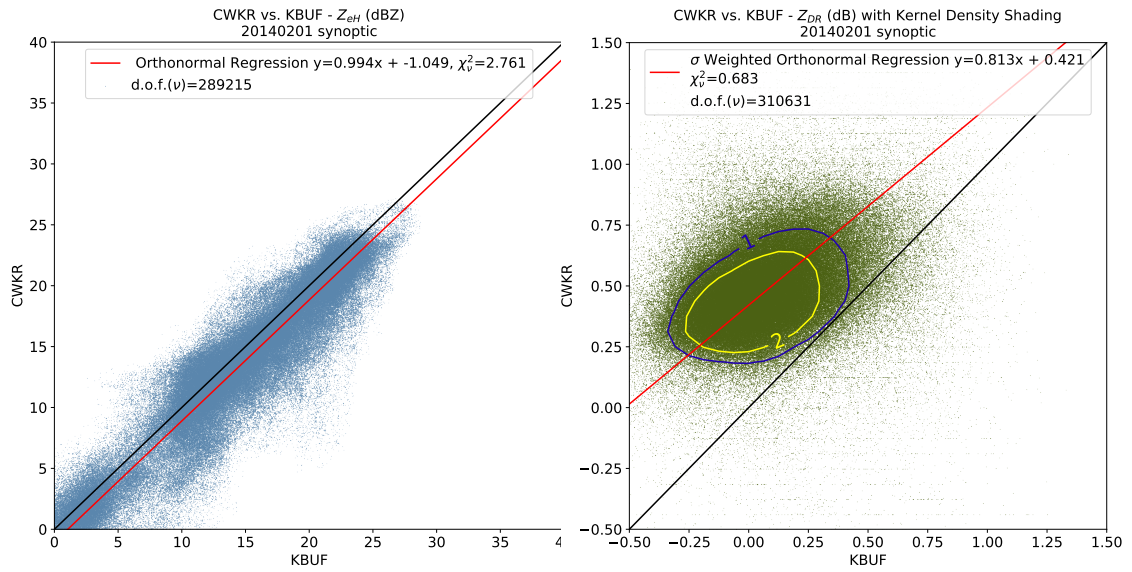


Figure 3.10: Gridded Z_{DR} comparison for 1 February 2014. Time-average of all admitted scans.

low error variance, while Figure 3.11b shows a very dense uni-modal kernel for Z_{DR} . The histogram in Figure 3.12 reveals that the anomalous bias between the radars is indicative of a Z_{DR} bias at CWKR, with a value of 0.217 dB. The source of this bias will be discussed in the next chapter.



(a) Z_{eH} (dBZ) with a orthonormal linear regression.
(b) Z_{DR} (dB) with a variance-weighted orthonormal linear regression and KDE contoured at 1 (blue) and 2 (yellow).

Figure 3.11: Direct comparisons for 1 February 2014. Dataset includes all admitted grid cells.

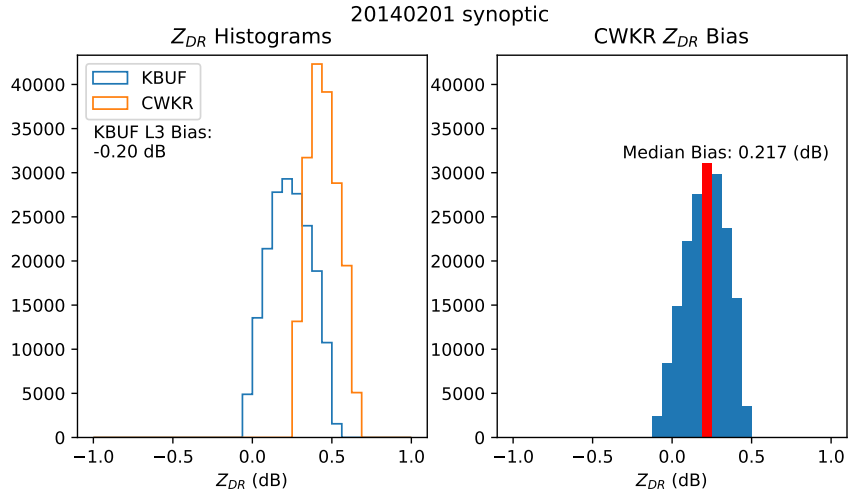


Figure 3.12: Histograms of Z_{DR} (left), Z_{DR} bias at CWKR (right). Bias is calculated by subtracting the gridded, bias-adjusted Z_{DR} at KBUF from the Z_{DR} at CWKR. Both datasets include points with $KDE \geq 2$. The modal bin is shaded red.

3.1.4 6 January 2015 - Lake-Effect

A highly zonal, NW flow aloft is present in this case, a typical pattern for lake-effect snow across the Great Lakes region. Narrow in radar appearance, a lake-effect band develops in the light winds near the surface; this case could be characterized as a weak “tea-kettle” event. Figure 3.13 depicts stationary banding in the time-averaged Z_{eH} . Of note is that CWKR observes more of the finer scale features as compared with KBUF, also evidenced by the +2.9 dBZ difference in Z_{eH} mean. This case stands out from the rest in terms of Z_{DR} , as the fields are very similar and unbiased as shown in Figure 3.14. The scatter-plot in Figure 3.15a confirms what is shown in the gridded Z_{eH} , with values skewed higher for CWKR. Figure 3.15b shows a bi-modal distribution for Z_{DR} , with the main peak around 0.5 dB and a secondary peak near 0 dB. The histogram in Figure 3.16 confirms the observed unbiased Z_{DR} , with a nearly zero median value of 0.003 dB.

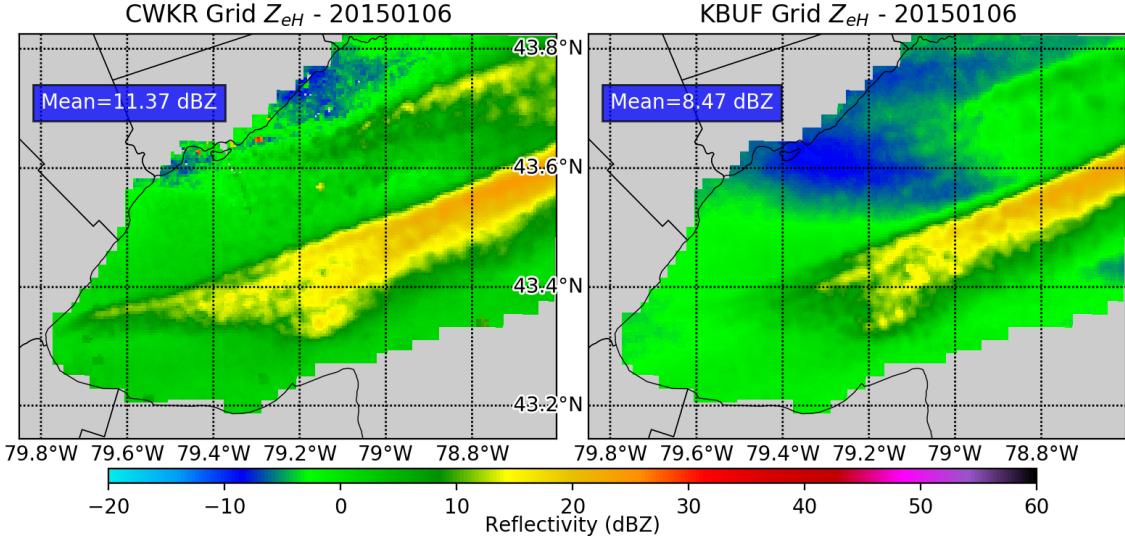


Figure 3.13: Gridded Z_{eH} comparison for 6 January 2015. Time-average of all admitted scans.

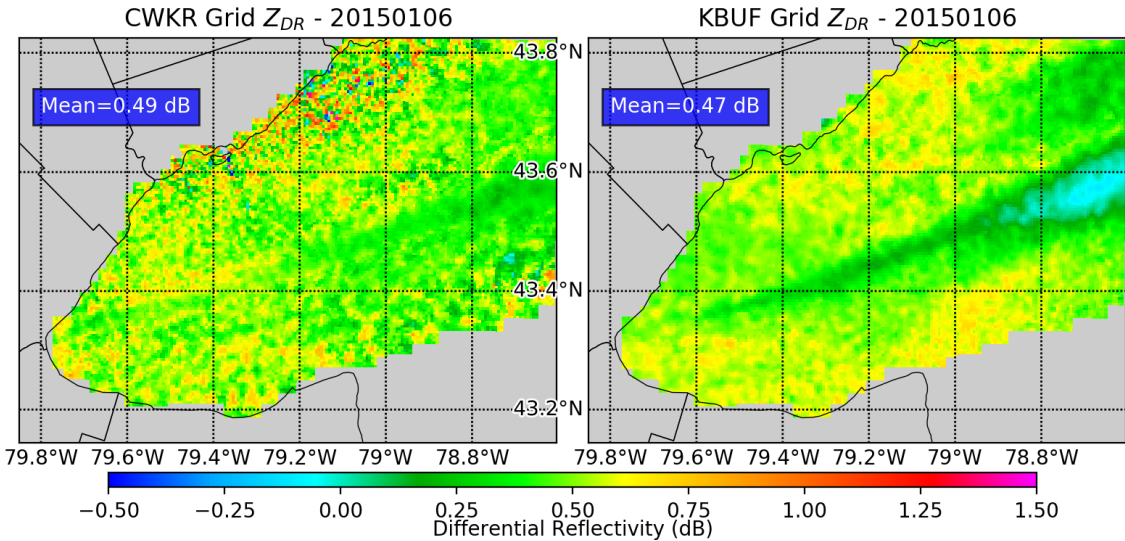
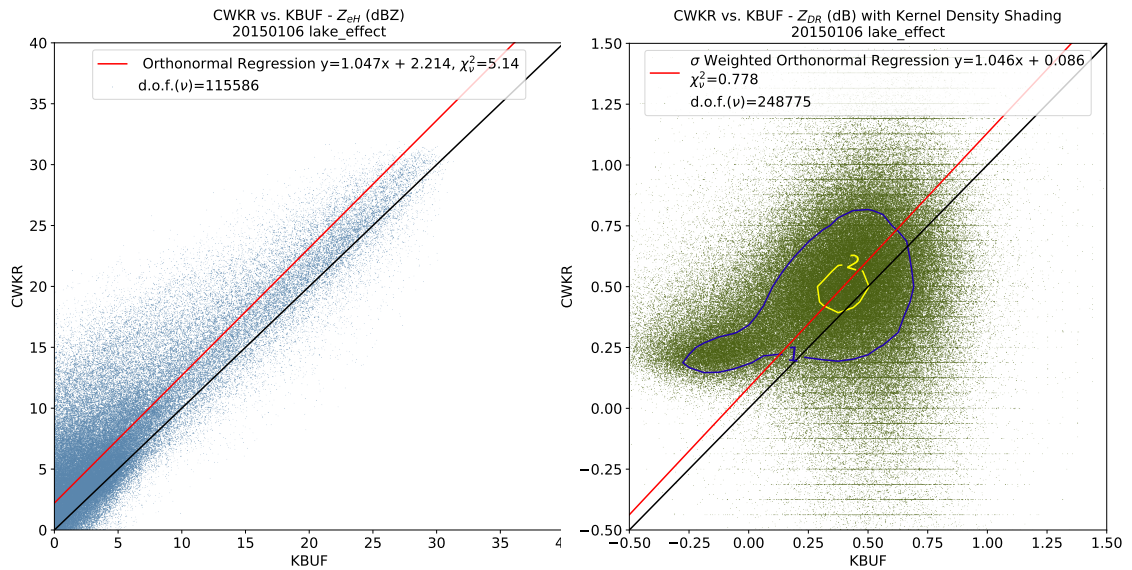


Figure 3.14: Gridded Z_{DR} comparison for 6 January 2015. Time-average of all admitted scans.



(a) Z_{eH} (dBZ) with a orthonormal linear regression.
(b) Z_{DR} (dB) with a variance-weighted orthonormal linear regression and KDE contoured at 1 (blue) and 2 (yellow).

Figure 3.15: Direct comparisons for 6 January 2015. Dataset includes all admitted grid cells.

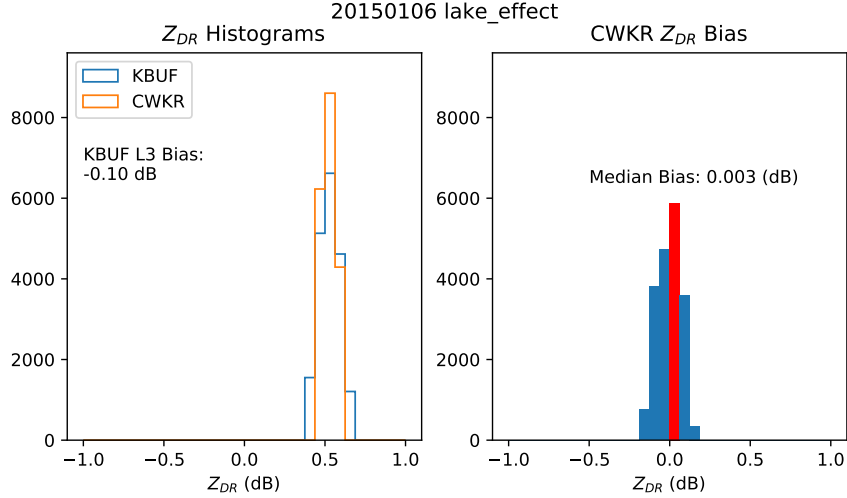


Figure 3.16: Histograms of Z_{DR} (left), Z_{DR} bias at CWKR (right). Bias is calculated by subtracting the gridded, bias-adjusted Z_{DR} at KBUF from the Z_{DR} at CWKR. Both datasets include points with $KDE \geq 2$. The modal bin is shaded red.

3.1.5 7 January 2015 - Synoptic

Less than 24 hours after the previous event, the zonal flow has buckled and a strong shortwave is overhead Southern Ontario. Radar animations indicate a frontally forced band of snow showers. Figure 3.17 shows the solid band of snow progressed from mid-lake southward, with similar depictions of Z_{eH} between radars. Inspection of the scatter-plot in Figure 3.19a indicates good agreement with reasonable error variance, while Figure 3.19b shows a uni-modal distribution of Z_{DR} with a relatively dense kernel. Meanwhile, Figure 3.18 shows two non-linear fields, especially noisy in areas of light returns. Estimating the bias at CWKR, the histogram in Figure 3.20 gives a median value of -0.040 dB. This indicates that no discernible bias exists outside of the error threshold of ± 0.1 dB for this event.

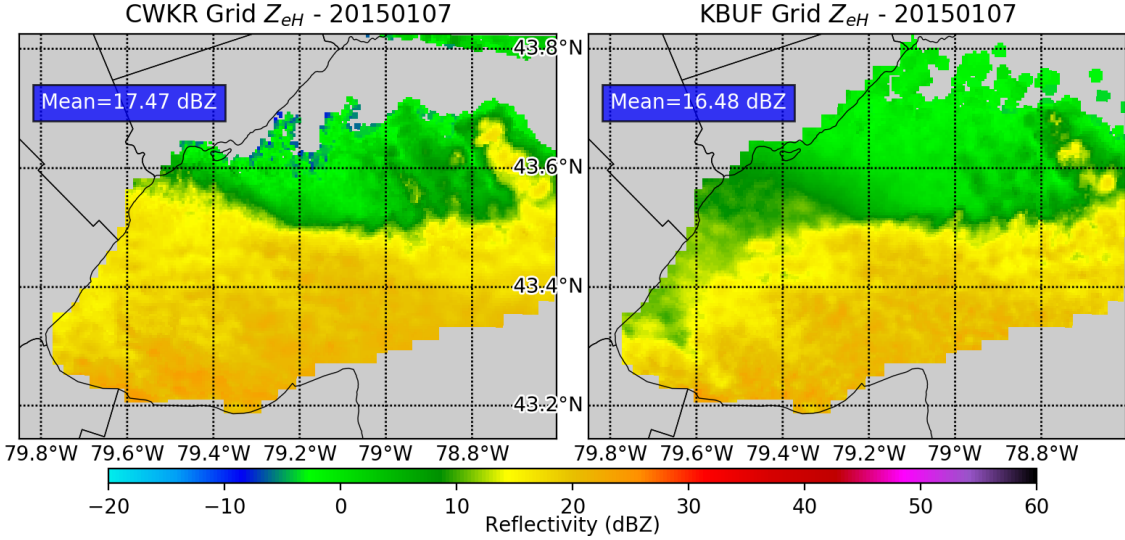


Figure 3.17: Gridded Z_{eH} comparison for 7 January 2015. Time-average of all admitted scans.

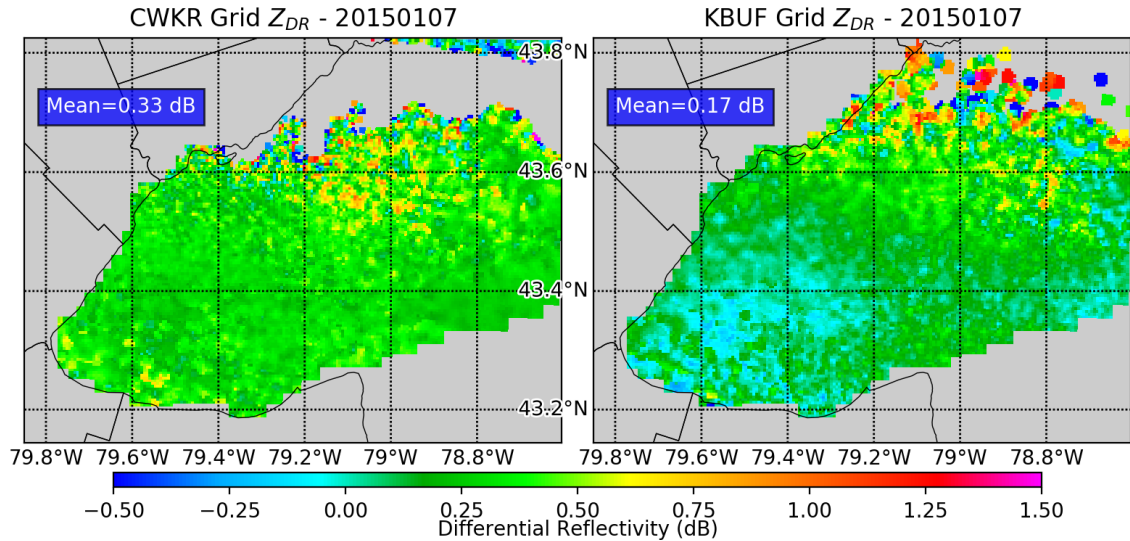
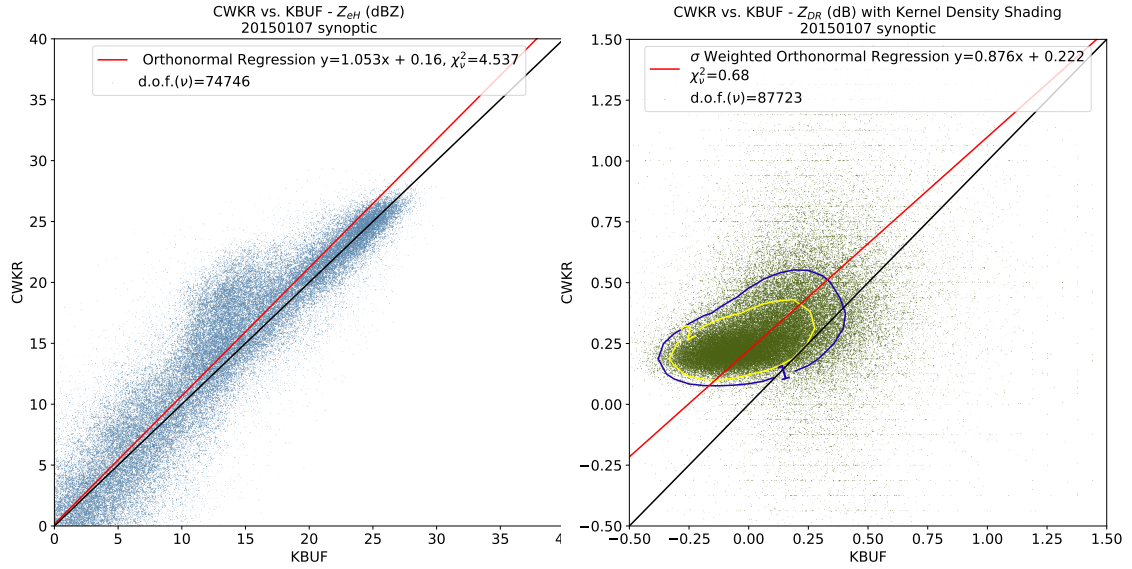


Figure 3.18: Gridded Z_{DR} comparison for 7 January 2015. Time-average of all admitted scans.



(a) Z_{eH} (dBZ) with a orthonormal linear regression.
(b) Z_{DR} (dB) with a variance-weighted orthonormal linear regression and KDE contoured at 1 (blue) and 2 (yellow).

Figure 3.19: Direct comparisons for 7 January 2015. Dataset includes all admitted grid cells.

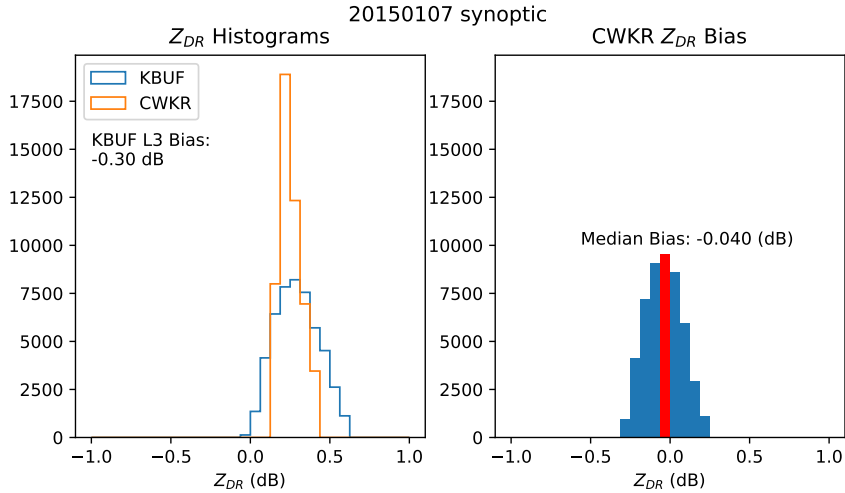


Figure 3.20: Histograms of Z_{DR} (left), Z_{DR} bias at CWKR (right). Bias is calculated by subtracting the gridded, bias-adjusted Z_{DR} at KBUF from the Z_{DR} at CWKR. Both datasets include points with $KDE \geq 2$. The modal bin is shaded red.

3.1.6 6 February 2015 - Synoptic

With a strong ridge centered over the SW US, Southern Ontario is on the backside of a progressive shortwave, with a radar animations indicating the passage of a front once again. A broad swath of snow is depicted by the time-averaged Z_{eH} fields in Figure 3.21, with the CWKR mean value 2 dBZ higher than KBUF. Comparing Z_{DR} as shown in Figure 3.22, the fields are similar but slightly biased. Partial beam blockages are noted at CWKR as indicated by the stripes in the NE section of grid. Next to the scatter-plots, with Figure 3.23 indicating a high frequency of points between 15-25 dBZ, a preferred range for comparing Z_{DR} values. Also of note is the high error variance of 9.773 . Figure 3.23b shows a dense, symmetric kernel with an ill-fitted regression. Proceeding on to the histograms in Figure 3.24, a median bias of 0.283 dB at CWKR is estimated. The source of the bias will be discussed in the next chapter.

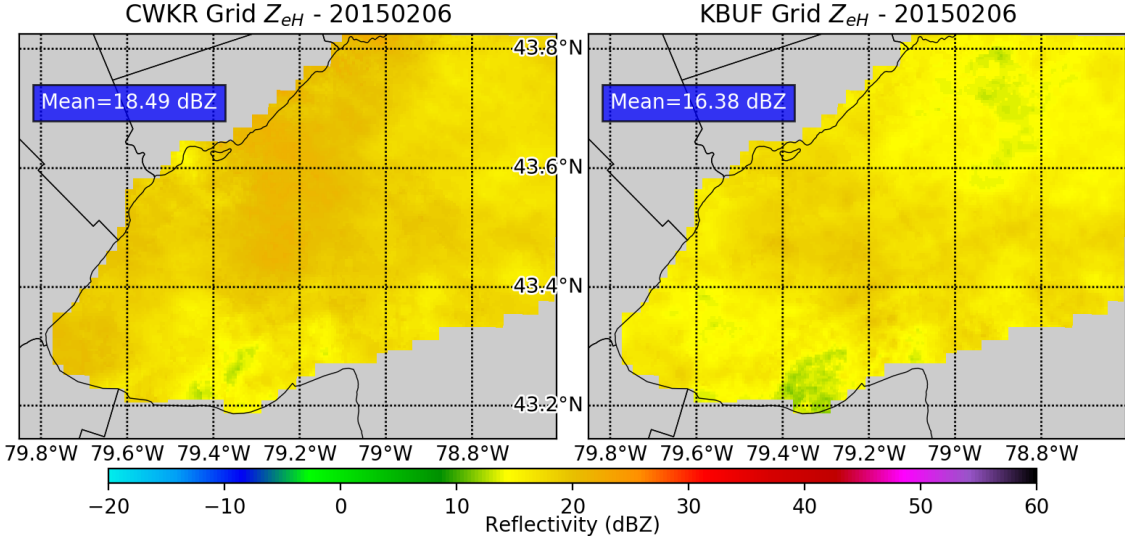


Figure 3.21: Gridded Z_{eH} comparison for 6 February 2015. Time-average of all admitted scans.

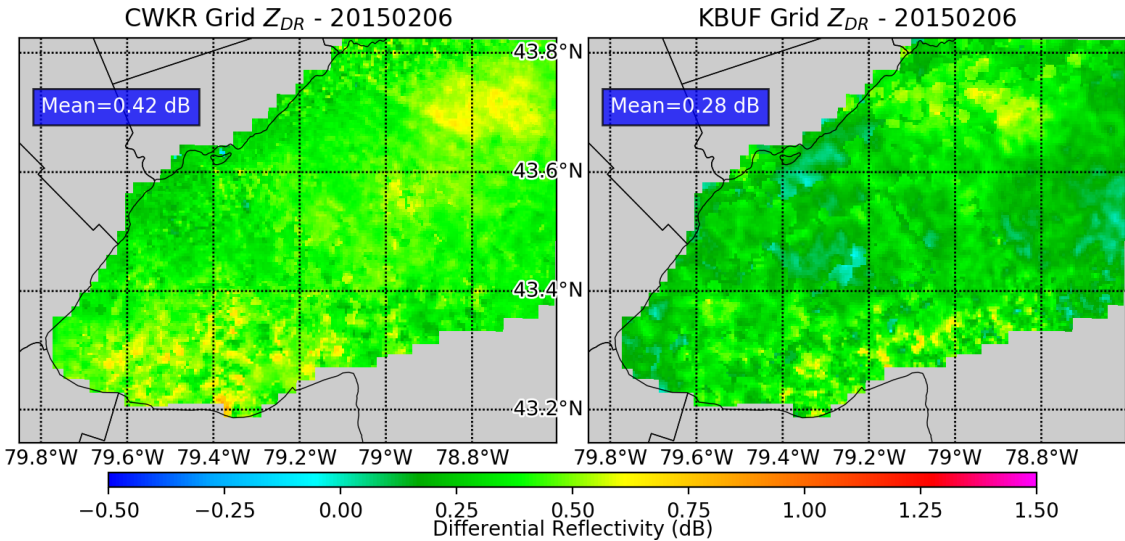
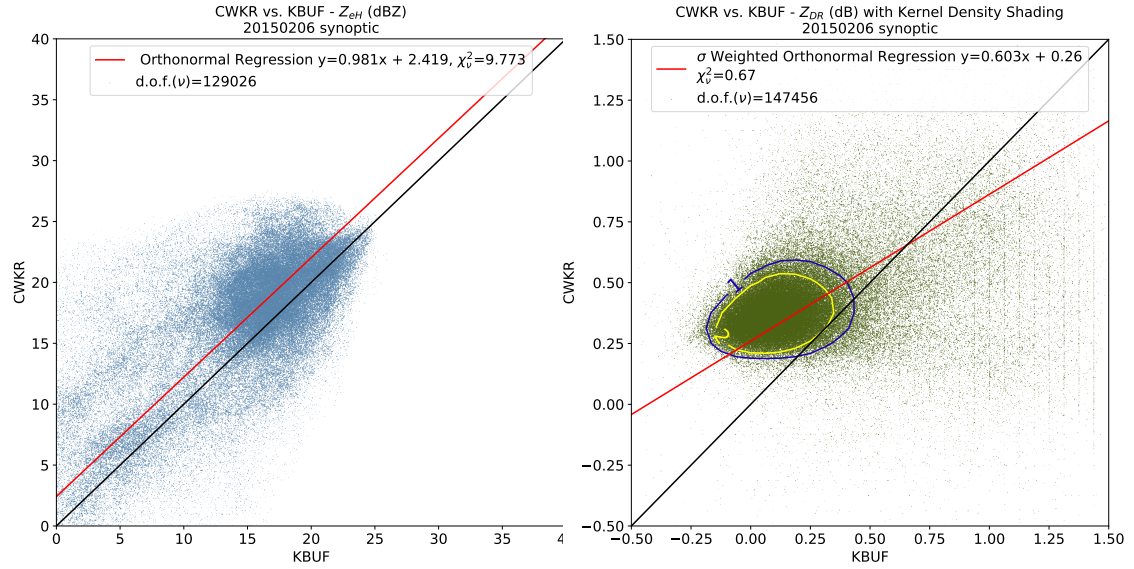


Figure 3.22: Gridded Z_{DR} comparison for 6 February 2015. Time-average of all admitted scans.



(a) Z_{eH} (dBZ) with a orthonormal linear regression.
(b) Z_{DR} (dB) with a variance-weighted orthonormal linear regression and KDE contoured at 1 (blue) and 2 (yellow).

Figure 3.23: Direct comparisons for 6 February 2015. Dataset includes all admitted grid cells.

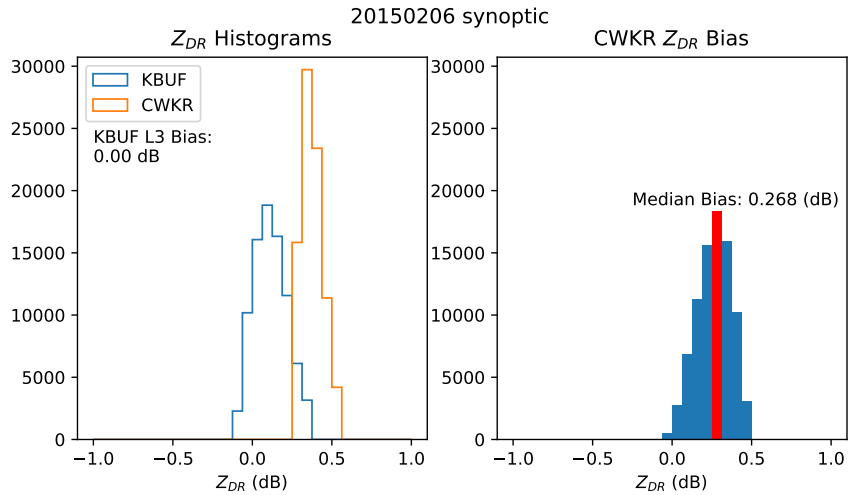


Figure 3.24: Histograms of Z_{DR} (left), Z_{DR} bias at CWKR (right). Bias is calculated by subtracting the gridded, bias-adjusted Z_{DR} at KBUF from the Z_{DR} at CWKR. Both datasets include points with $KDE \geq 2$. The modal bin is shaded red.

3.1.7 14 February 2015 - Lake-Effect

As a strong lobe of the polar vortex approaches Southern Ontario, strong W to SW flow from the surface to 850mb allows for a prolonged period of lake-effect snow over the lake. From Figure 3.25, we see again that CWKR resolves the convective scale features of the snow squalls better than KBUF. Horizontal convective rolls are clearly depicted by CWKR, whereas they become muddled by KBUF. Figure 3.26 shows similar patterns of Z_{DR} , but a large bias exists. The Z_{eH} scatter-plot in Figure 3.27 shows a dense clustering of points for low values, becoming increasingly skewed towards CWKR as they increase. For Z_{DR} , the variance-weighted regression achieves a near perfect reduced chi-squared statistic (χ^2_ν) of 0.968. The histogram in Figure 3.28 indicates a anomalous bias for this event, with a median value of 0.377 dB.

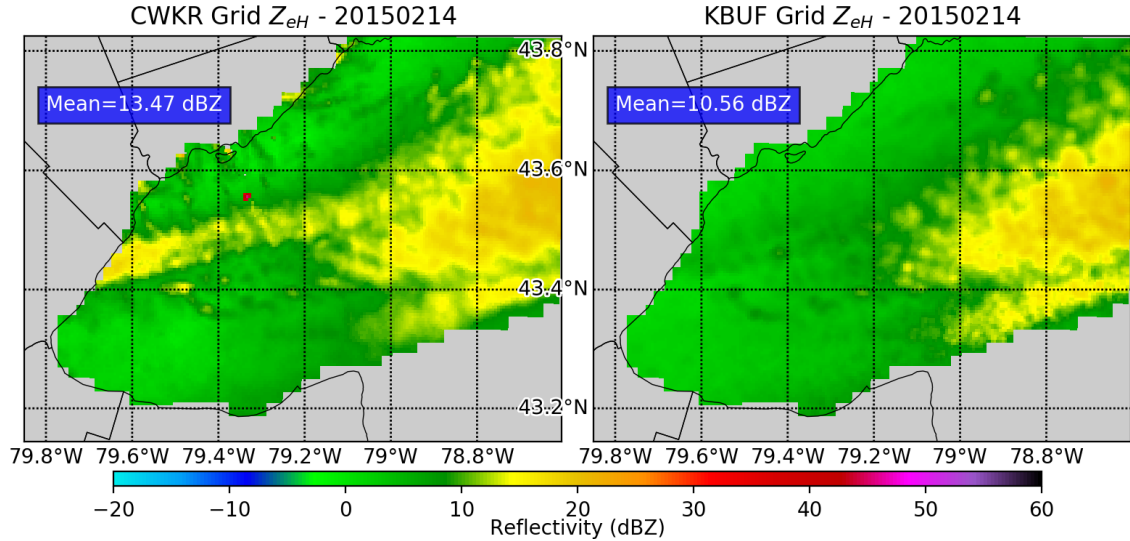


Figure 3.25: Gridded Z_{eH} comparison for 14 February 2015. Time-average of all admitted scans.

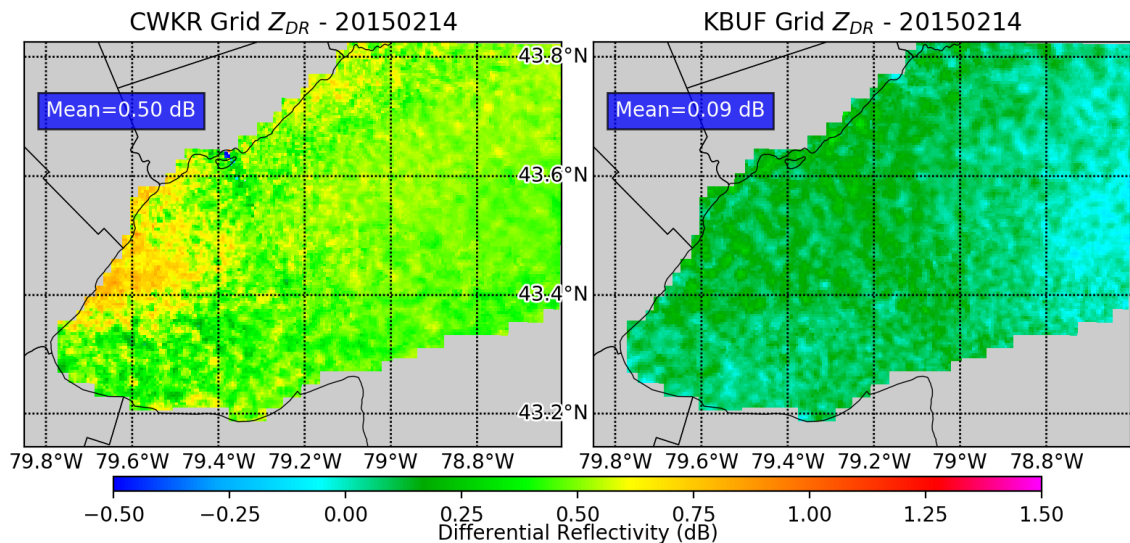
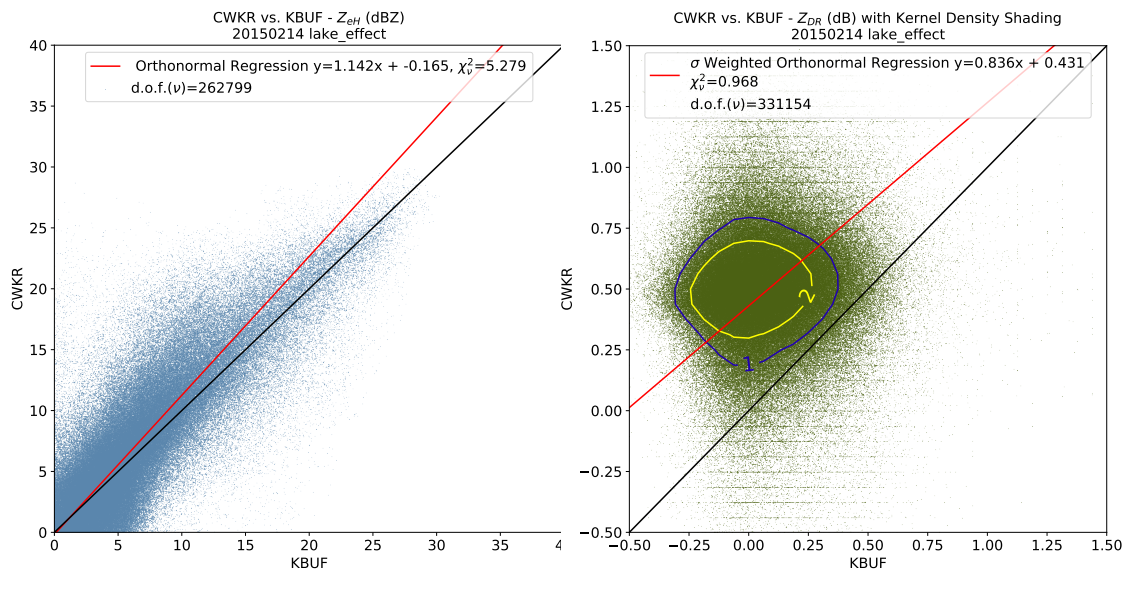


Figure 3.26: Gridded Z_{DR} comparison for 14 February 2015. Time-average of all admitted scans.



(a) Z_{eH} (dBZ) with a orthonormal linear regression.

(b) Z_{DR} (dB) with a variance-weighted orthonormal linear regression and KDE contoured at 1 (blue) and 2 (yellow).

Figure 3.27: Direct comparisons for 14 February 2015. Dataset includes all admitted grid cells.

3.1.8 18 February 2015 - Lake-Effect

Four days later, The polar vortex has arrived in earnest for this event, with the 500 dm isoheight at 500mb nearing as far south as Windsor, ON. The cold airmass allows for the development of an intense lake-effect snow band, the strongest of all the lake-effect cases as indicated by the Z_{eH} means in Figure 3.29. Next, Figure 3.30 shows similar band structure as compared between radars, with a bias evident. A orthonormal fit with decent agreement between radars is shown in Figure 3.31a, with the values biased towards CWKR all along the line. In Figure 3.31b, a unique bi-modal distribution of Z_{DR} is shown, with two peaks equal in magnitude around 0.50 dB and 0.75 dB. The histogram in Figure 3.32 also depicts this bi-modal distribution of Z_{DR} , and gives an estimate median value of 0.296 dB. The source of the bias will be discussed in the next chapter.

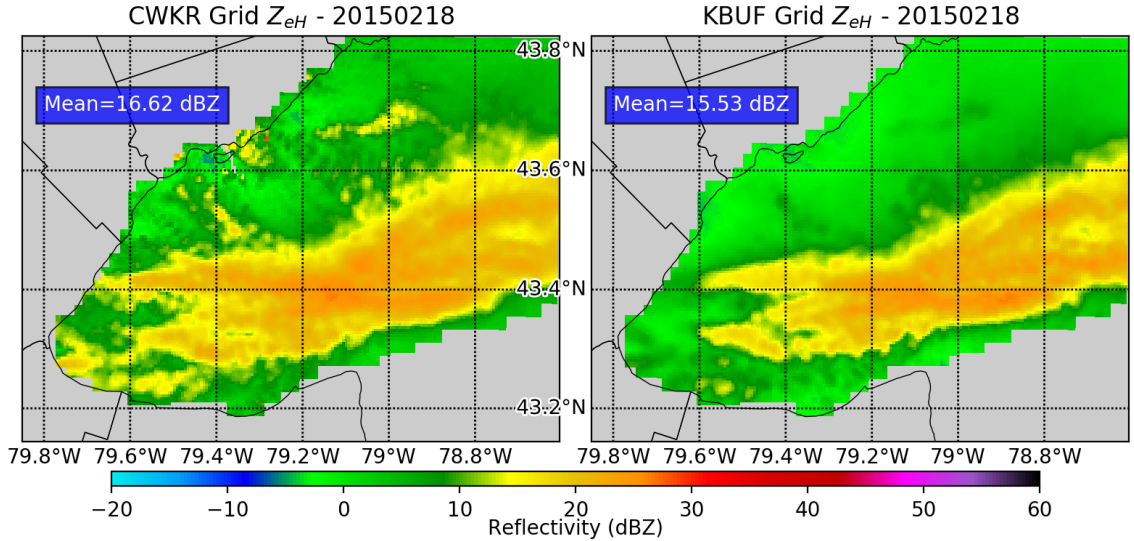


Figure 3.29: Gridded Z_{eH} comparison for 18 February 2015. Time-average of all admitted scans.

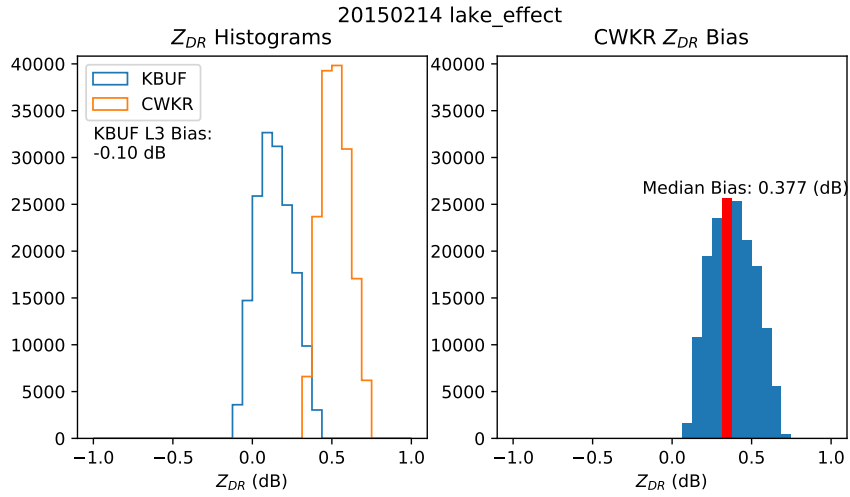


Figure 3.28: Histograms of Z_{DR} (left), Z_{DR} bias at CWKR (right). Bias is calculated by subtracting the gridded, bias-adjusted Z_{DR} at KBUF from the Z_{DR} at CWKR. Both datasets include points with $KDE \geq 2$. The modal bin is shaded red.

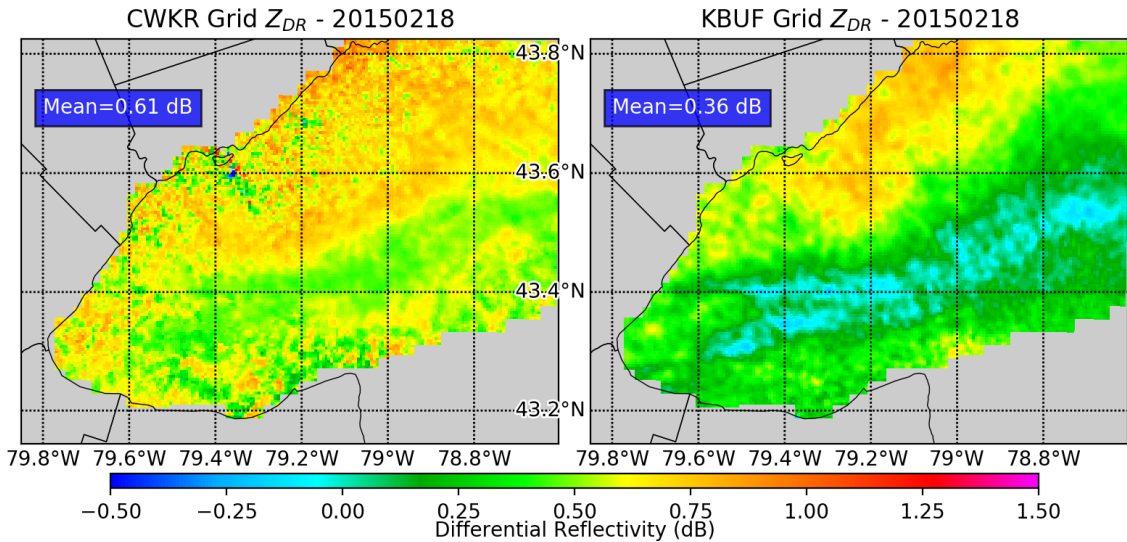
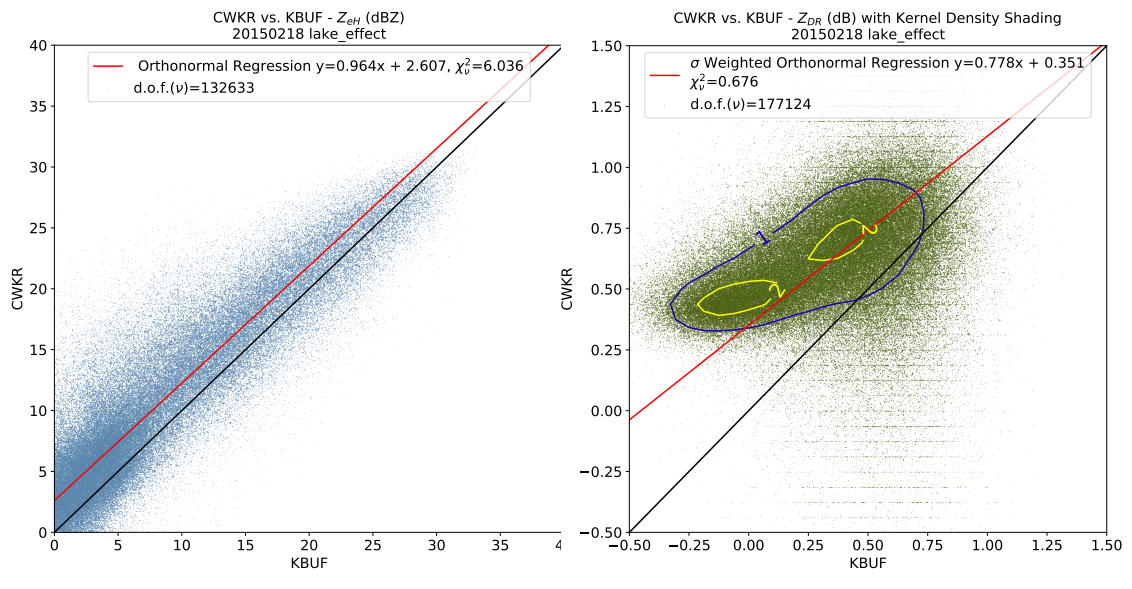


Figure 3.30: Gridded Z_{DR} comparison for 18 February 2015. Time-average of all admitted scans.



(a) Z_{eH} (dBZ) with a orthonormal linear regression.
 (b) Z_{DR} (dB) with a variance-weighted orthonormal linear regression and KDE contoured at 1 (blue) and 2 (yellow).

Figure 3.31: Direct comparisons for 18 February 2015. Dataset includes all admitted grid cells.

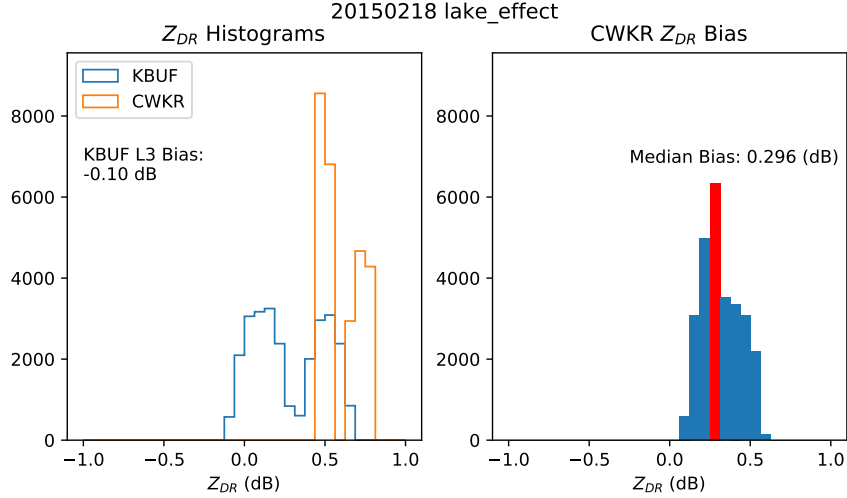


Figure 3.32: Histograms of Z_{DR} (left), Z_{DR} bias at CWKR (right). Bias is calculated by subtracting the gridded, bias-adjusted Z_{DR} at KBUF from the Z_{DR} at CWKR. Both datasets include points with $KDE \geq 2$. The modal bin is shaded red.

3.1.9 10 February 2016 - Lake-Effect

The 500mb ridge axis is centered to the south of Southern Ontario in the Appalachians, with WNW flow aloft during this event. With a slight amount of pre existing instability augmenting the lake induced instabilities, a healthy band of lake-effect snow forms on the southern end of the lake. KBUF observes higher values of Z_{DR} in this band on the southern edge of the lake, as shown in Figure 3.33. This is likely due to the CWKR beam overshooting the shallow convection while the KBUF beam is lower in height. The intensity of the band overcomes the degraded signal strength due to beam blockages at CWKR, evident in Z_{DR} on the western end of the band in Figure 3.34.

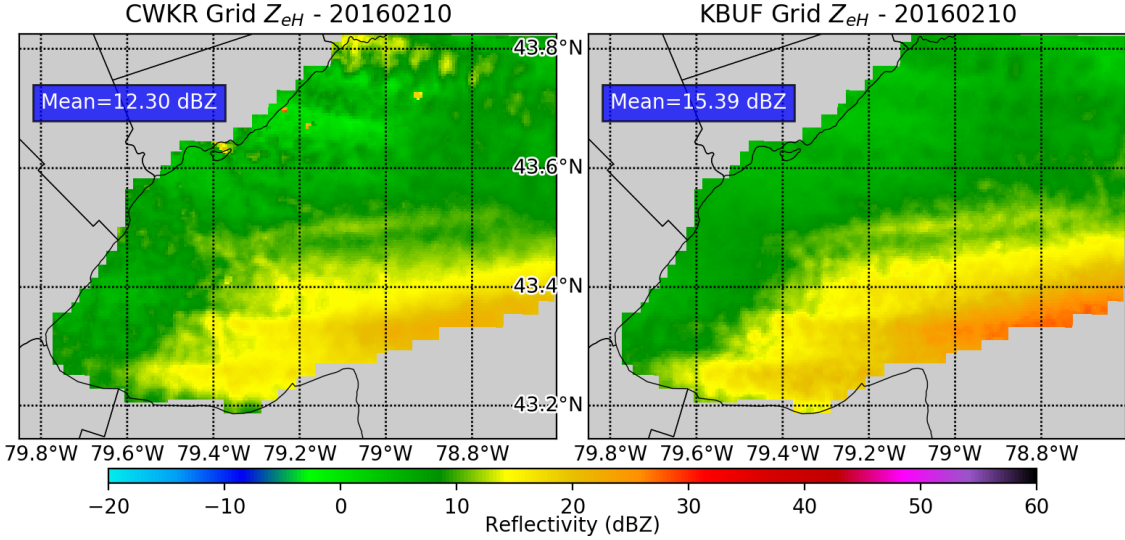


Figure 3.33: Gridded Z_{eH} comparison for 10 February 2016. Time-average of all admitted scans.

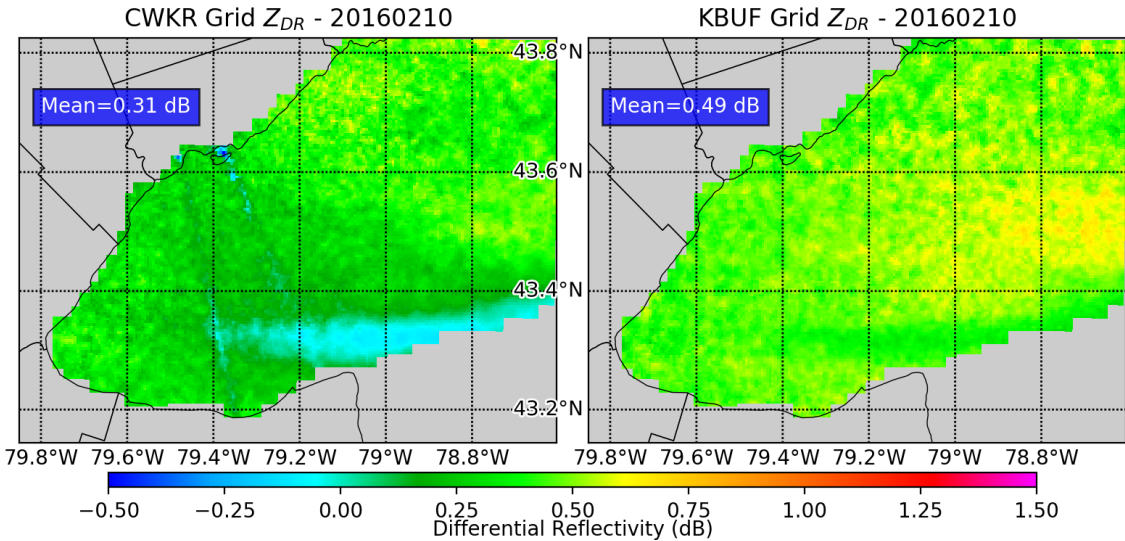


Figure 3.34: Gridded Z_{DR} comparison for 10 February 2016. Time-average of all admitted scans.

Due to the long duration of this case, the large sample of matched points was obtained from this case. Figure 3.35a shows that matched Z_{eH} values tends higher towards KBUF as they increase. Next, Figure 3.35b demonstrates the value of the kernel density estimate, as its impossible to visually analyze a scatter-plot with nearly a million points. The kernel extracted from the data is small, but information rich. Figure 3.36 leverages this information to show that the median Z_{DR} at CWKR is -0.055 dB, indicating no discernible bias exists outside of the error threshold of ± 0.1 dB for this event.

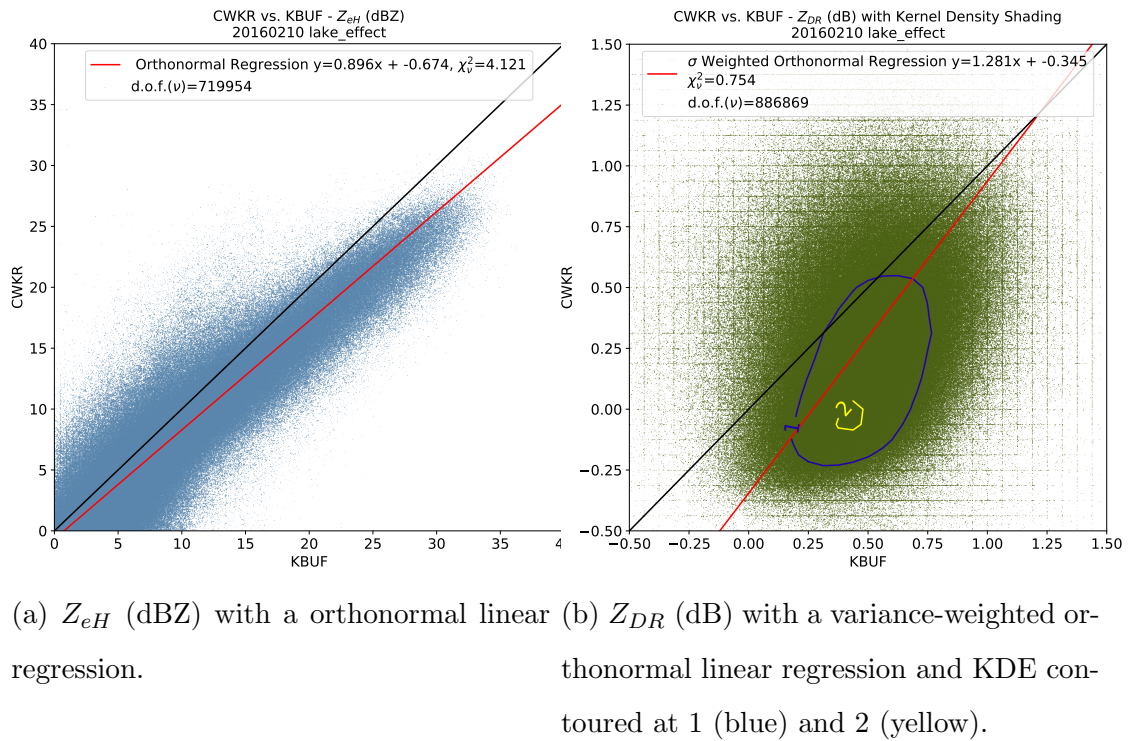


Figure 3.35: Direct comparisons for 10 February 2016. Dataset includes all admitted grid cells.

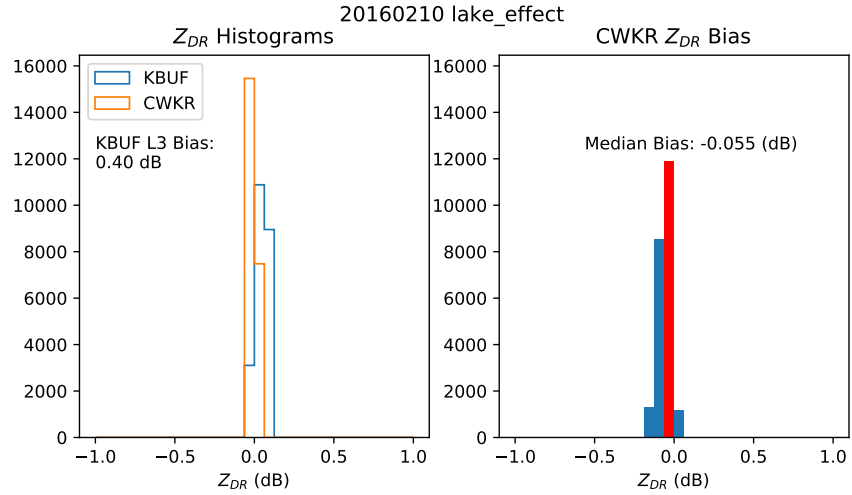


Figure 3.36: Histograms of Z_{DR} (left), Z_{DR} bias at CWKR (right). Bias is calculated by subtracting the gridded, bias-adjusted Z_{DR} at KBUF from the Z_{DR} at CWKR. Both datasets include points with $KDE \geq 2$. The modal bin is shaded red.

3.1.10 15 December 2016 - Synoptic

A deep longwave trough is centered over Southern Ontario, with an Arctic airmass in place over the Great Lakes region. With meager moisture in place, a post-frontal trough manages to squeeze out some passing snow-showers. As indicated by Figure 3.37, the spatial patterns of Z_{eH} are in very good agreement. In contrast, Figure 3.38 shows two very noisy Z_{DR} fields. Even with the small sample size, Figure 3.39 shows that decent fits are achieved for both moments. Meanwhile, the histogram in Figure 3.40 shows that the estimate of bias at CWKR is large, with a median value of -0.465 dB. This case is an outlier; the source of this large bias will be discussed in the next chapter.

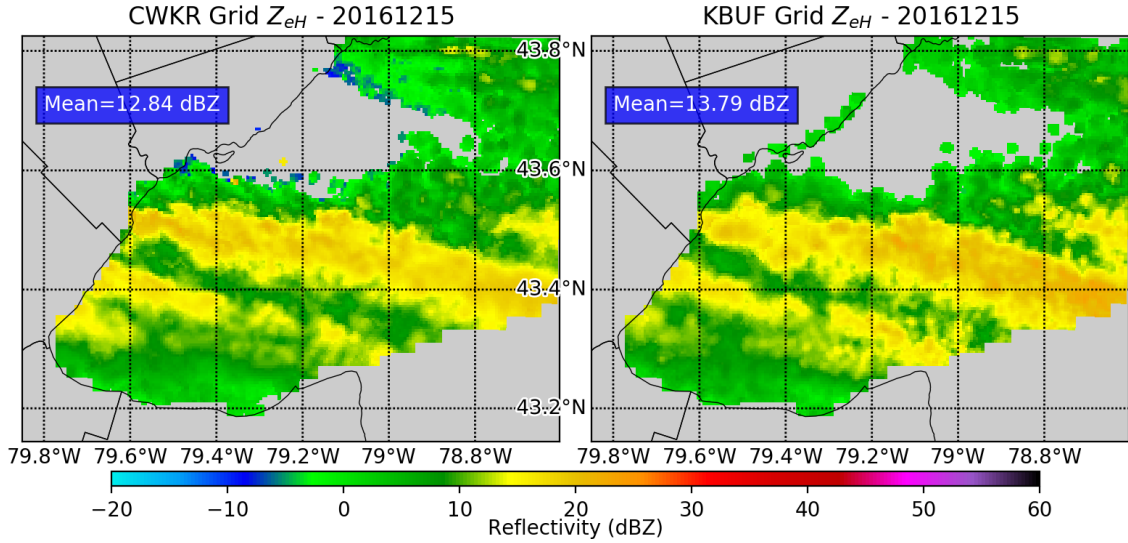


Figure 3.37: Gridded Z_{eH} comparison for 15 December 2016. Time-average of all admitted scans.

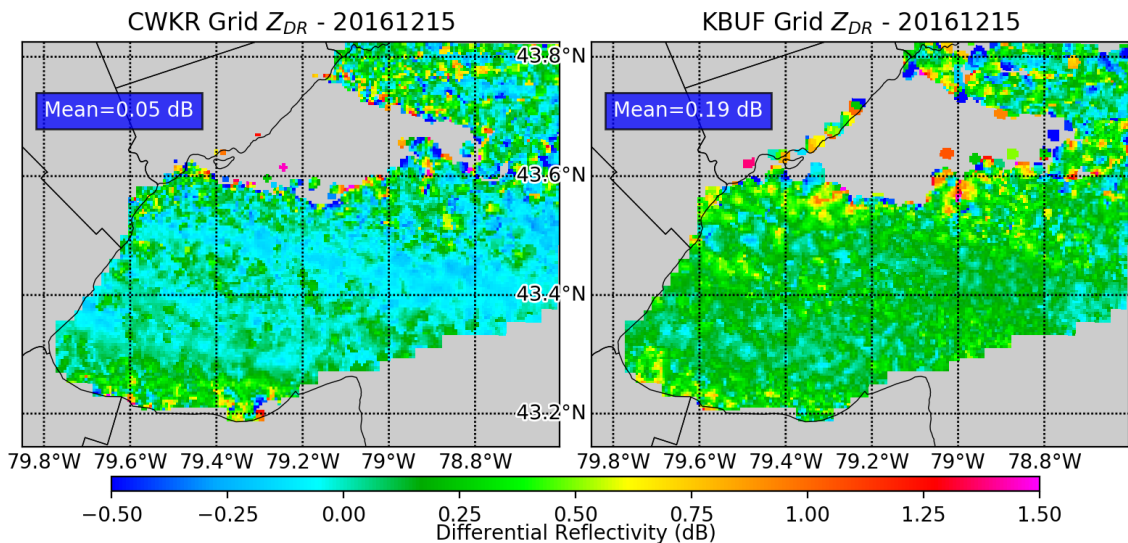
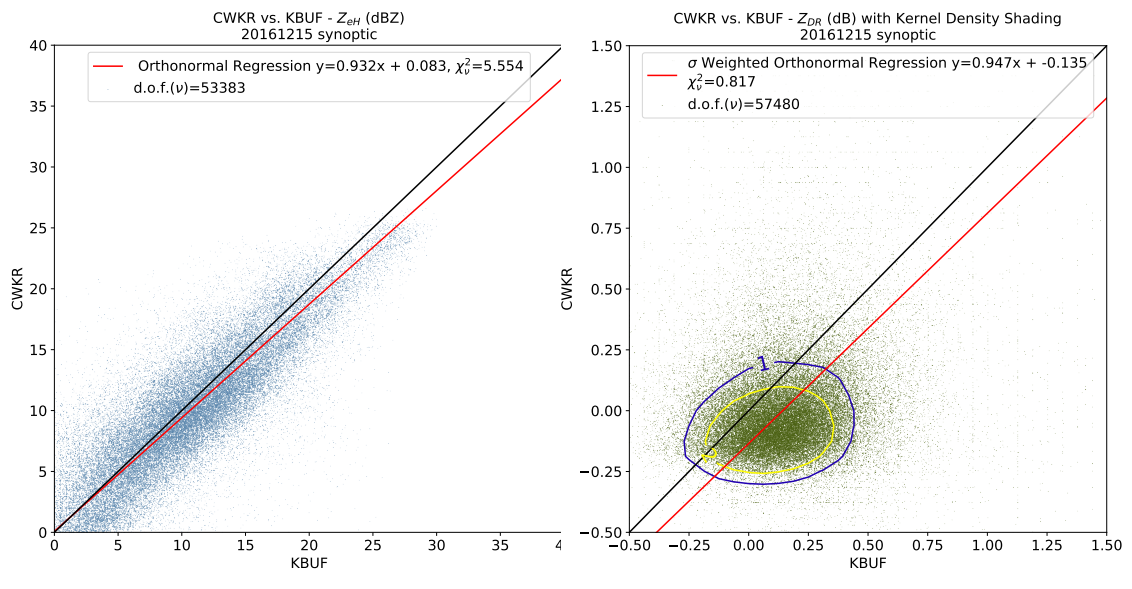


Figure 3.38: Gridded Z_{DR} comparison for 15 December 2016. Time-average of all admitted scans.



(a) Z_{eH} (dBZ) with a orthonormal linear regression.
 (b) Z_{DR} (dB) with a variance-weighted orthonormal linear regression and KDE contoured at 1 (blue) and 2 (yellow).

Figure 3.39: Direct comparisons for 15 December 2016. Dataset includes all admitted grid cells.

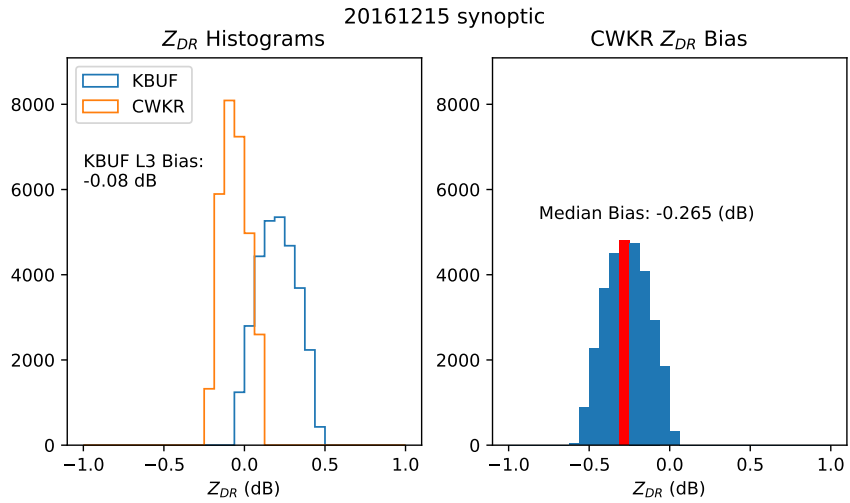


Figure 3.40: Histograms of Z_{DR} (left), Z_{DR} bias at CWKR, determined by subtracting the gridded, bias adjusted Z_{DR} at KBUF from the Z_{DR} at CWKR. Both datasets include points with $KDE \geq 2$. The modal bin is shaded red.

3.2 Z_{eH} Subset Comparisons

Now that all the cases have been presented individually, two subsets are created for comparison. The first consists of the five lake-effect events, the subset of interest, as compared with the five synoptic events, which act as a control subset. A comparison of these subsets is shown in Figure 3.41, with a scatter-plot of KBUF Z_{eH} data versus CWKR on the common grid. Figure 3.41a is the subset of synoptic events while Figure 3.41b is the subset of lake-effect events.

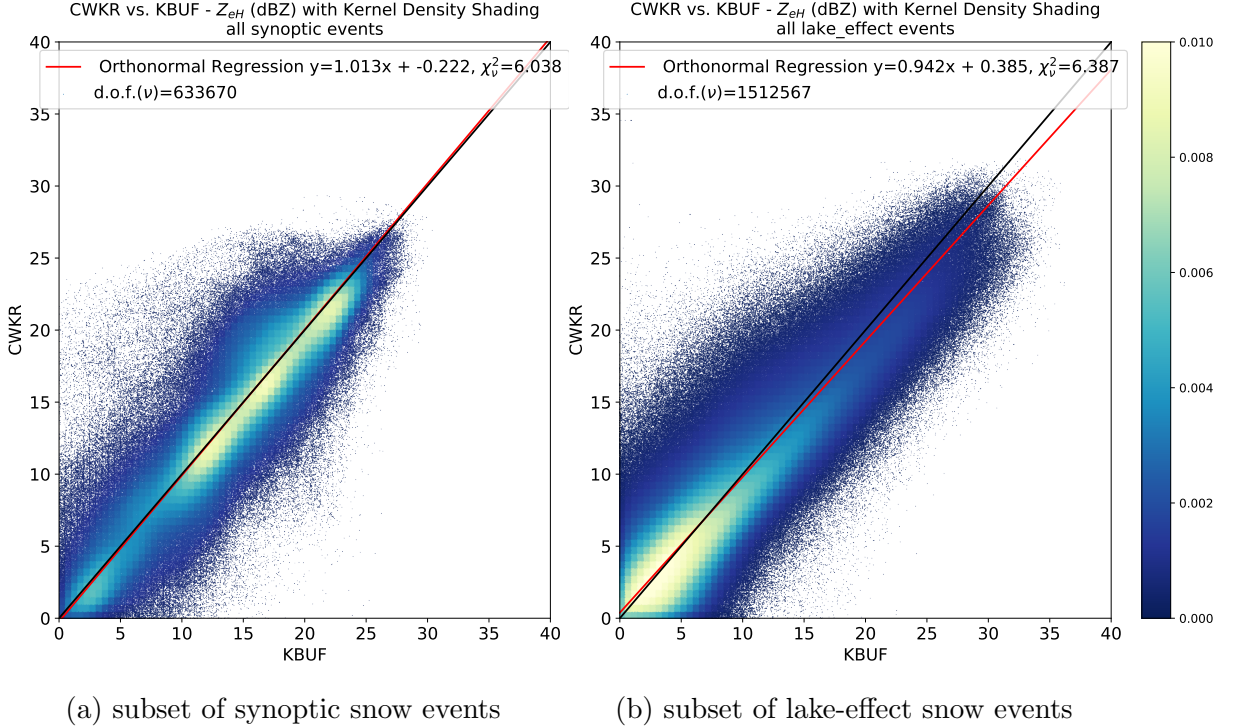


Figure 3.41: Scatter-plots of CWKR versus KBUF grid analyzed reflectivity, with Kernel Density Estimation shading. The red line is an Orthonormal Linear Regression, with a black identity line.

These results show that comparable performance between radars is achieved in lake-effect events. An interesting result is the clustering of points for the range $0 < Z_{eH} < 10$ dBZ in lake-effect events. This is in contrast with the higher clustering of points in synoptic events, from $10 < Z_{eH} < 25$. This could indicate that KBUF is underestimating Z_{eH} in shallow lake-effect events, as the slope of regression is 0.94, compared to 1.01 for synoptic events.

3.3 KDE Constrained Z_{DR}

The next step is to demonstrate the utility of constraining the datasets with a KDE threshold. Points with $\text{KDE} < 2$ are discarded; this level is chosen through subjective analysis of the scatterplots in the previous section. These constrained Z_{DR} datasets represent samples where both radars indicate a high likelihood of representing the true bulk hydrometeor type present in any given volume, essentially creating an even playing field between events. An inference on the predominant hydrometeor in any given event can then be drawn, based on the range of values found in the constrained set. All cases are presented in chronological order.

3.3.1 Unbiased Z_{DR} Cases

Cases where the calculated Z_{DR} bias at CWKR did not exceed the error threshold of ± 0.1 dB are presented first, without any bias adjustment made.

3.3.1.1 18 January 2014

The first unbiased case in Figure 3.42 shows how the constraint highlights the cells that passed through the eastern side of the domain. Areas of higher Z_{eH} are correlated with the constrained Z_{DR} areas, indicating that dataset is distilled down to include only returns with higher signal-to-noise-ratio (SNR) values. Z_{DR} values closer to 0.50 dB in this case indicate that less aggregation is occurring and more pristine crystals are present.

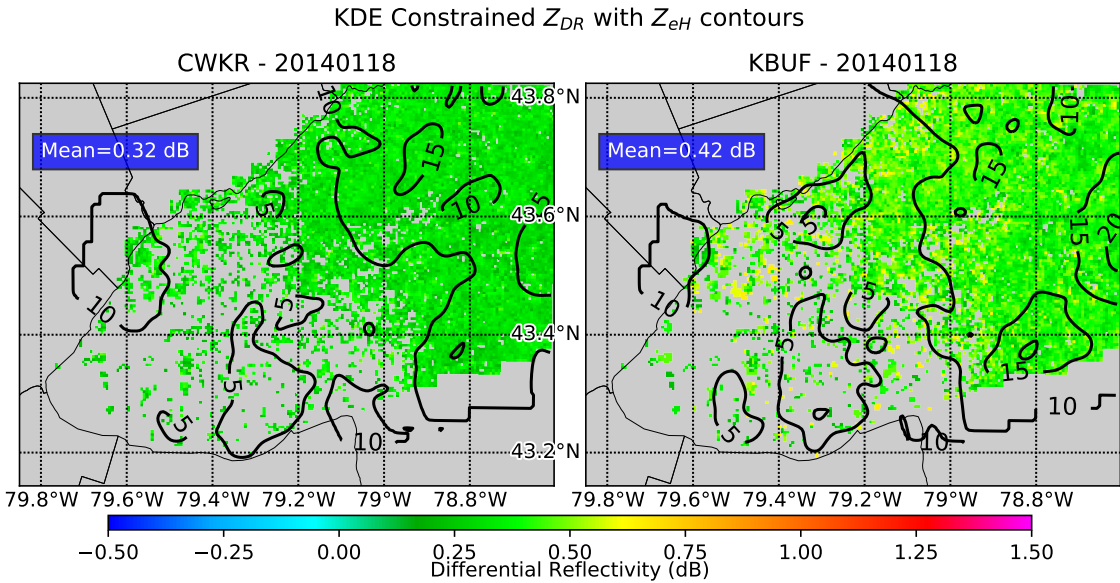


Figure 3.42: Comparison of gridded Z_{DR} with Gaussian ($\sigma = 3$) smoothed contours of Z_{eH} for 18 January 2014. Z_{DR} is constrained by only including points with a KDE ≥ 2 .

3.3.1.2 23 January 2014

The next case in Figure 3.43 also shows the advantage of the constraintment, in that it delineates the banding pattern present in this case. Furthermore, the partial beam blockages present in the unconstrained dataset are removed. Both radars agree that this intense snow squall is generating dry aggregated snow, with Z_{DR} values in the characteristic range of 0-0.2 dB.

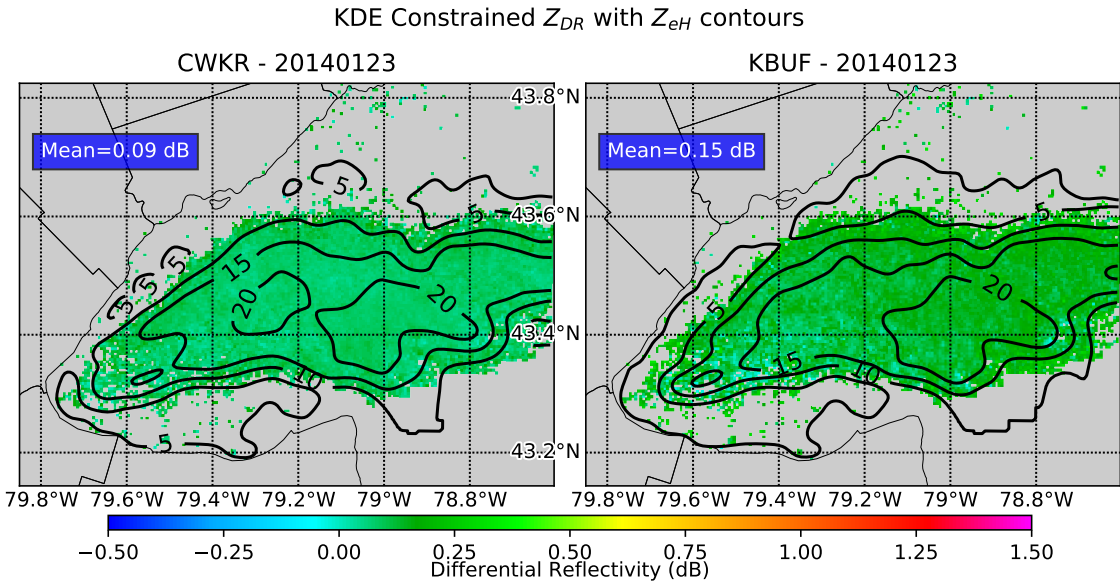


Figure 3.43: Comparison of gridded Z_{DR} with Gaussian ($\sigma = 3$) smoothed contours of Z_{eH} for 23 January 2014. Z_{DR} is constrained by only including points with a $KDE \geq 2$.

3.3.1.3 6 January 2015

The 6 January 2015 case shown in Figure 3.44 shows remarkably similar fields for both variables. This is likely due to the extremely shallow nature of the snow-squall, with a mean max echo top of 0.46 km. Another feature shown is the high amount of points excluded in high Z_{eH} areas, i.e. inside the 20 dBZ contour. Looking back at Figure 3.14, even with very similar mean values of Z_{DR} , CWKR reports much higher values in this area. It is likely that large, spherical aggregates were occurring inside this 20 dBZ contour. As these large particles approach the C-Band wavelength of 5 cm, they could be inducing resonance effects; this type of resonance effect has been observed by Hassan et al. (2017).

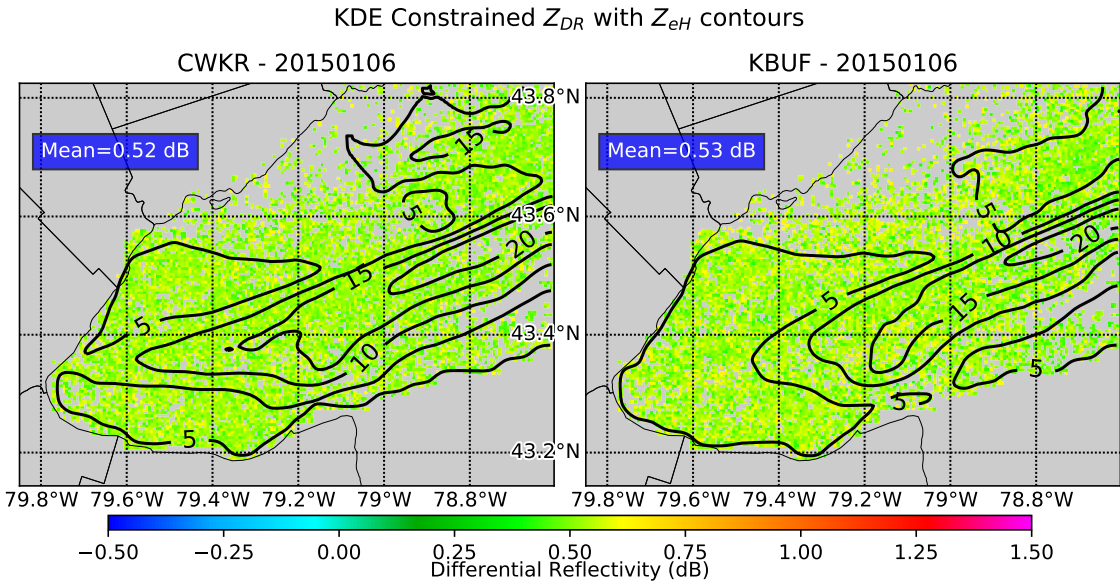


Figure 3.44: Comparison of gridded Z_{DR} with Gaussian ($\sigma = 3$) smoothed contours of Z_{eH} for 6 January 2014. Z_{DR} is constrained by only including points with a KDE ≥ 2 .

3.3.1.4 7 January 2015

Once again, as shown in Figure 3.45, excellent delineation of precipitating structures is achieved through this method. No obvious pattern emerges within the higher Z_{DR} , with values varying tightly around 0.2 dB. Of note are the higher Z_{DR} values on the edge of the heavier precipitation shield as reported by KBUF, with CWKR not reporting these higher values. This could be due to unequal beam broadening between radars.

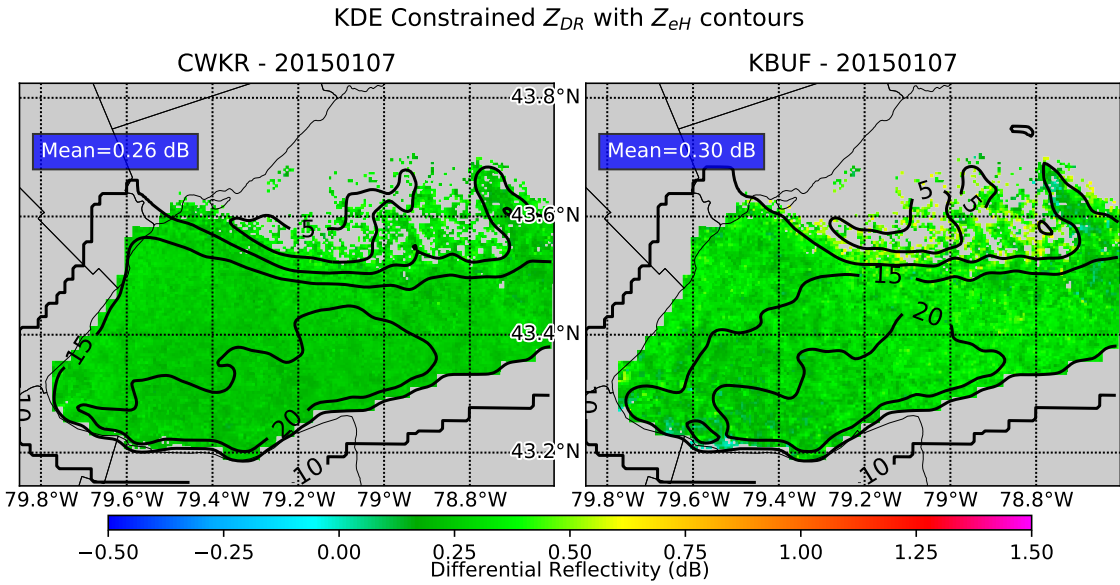


Figure 3.45: Comparison of gridded Z_{DR} with Gaussian ($\sigma = 3$) smoothed contours of Z_{eH} for 7 January 2014. Z_{DR} is constrained by only including points with a KDE ≥ 2 .

3.3.1.5 10 February 2016

A much more subtle gradient from filtered to admitted points is present in Figure 3.46. Z_{DR} values are right around 0 dB for this case, which indicates spherical aggregates are dominating. This event has the warmest surface temperature, with the 12Z Buffalo sounding reporting -2.7° C. Warmer temperatures closer to 0° C are conducive for this type of aggregation process (Hosler et al. 1957).

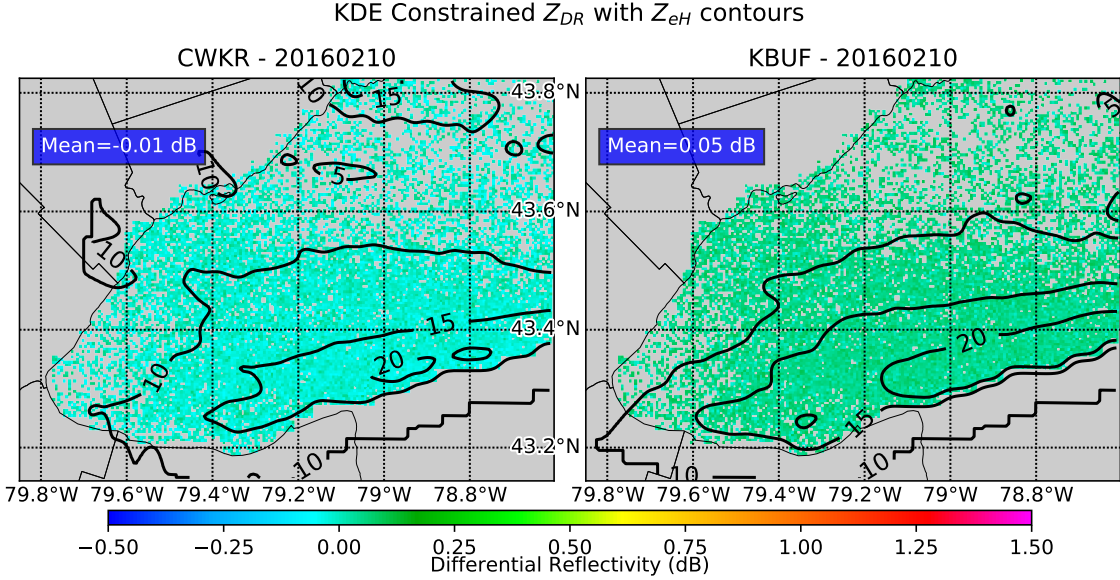


Figure 3.46: Comparison of gridded Z_{DR} with Gaussian ($\sigma = 3$) smoothed contours of Z_{eH} for 10 February 2016. Z_{DR} is constrained by only including points with a KDE ≥ 2 .

3.3.2 Biased Z_{DR} Cases

Cases where the calculated Z_{DR} bias at CWKR exceeded the error threshold of ± 0.1 dB are presented next, with the previously calculated median bias used to adjust Z_{DR} values at CWKR.

3.3.2.1 1 February 2014

The first biased case shown in Figure 3.47 indicates a bias even after adjustment. This means that the sampling volume differences are large enough to create an uncorrectable bias. Large vertical gradients of hydrometeor shape could explain why this occurred in this case and not others, which is supported by this case having the highest mean max top of 4.3 km.

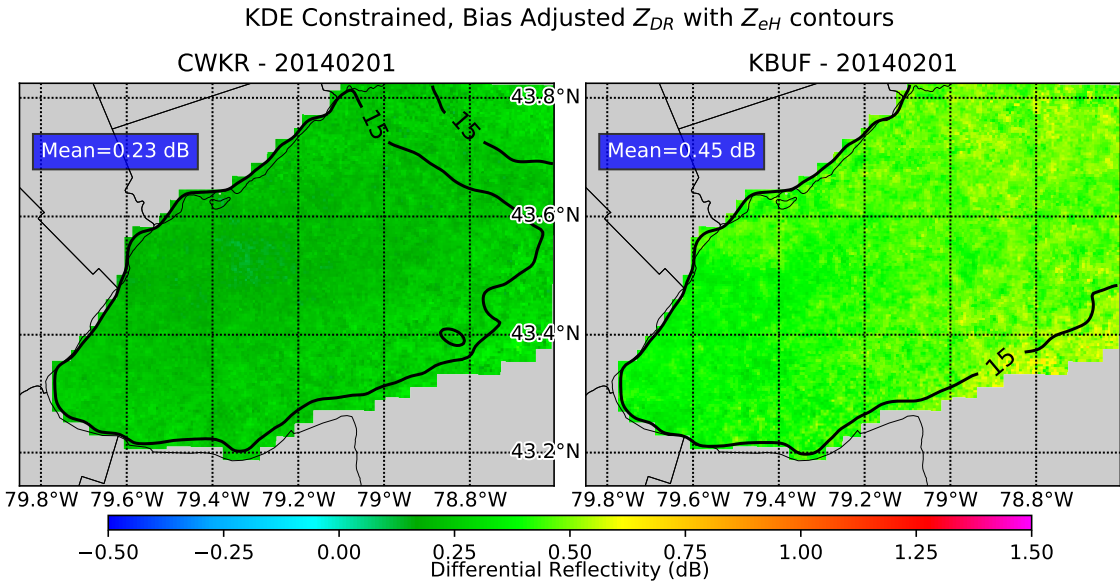


Figure 3.47: Comparison of gridded Z_{DR} with Gaussian ($\sigma = 3$) smoothed contours of Z_{eH} for 1 February 2014. Z_{DR} is constrained by only including points with a KDE ≥ 2 , and is bias-adjusted using the offset calculated in the first section of Chapter 3.

3.3.2.2 6 February 2015

In the next case in Figure 3.48, the mean Z_{DR} values are nearly the same, but the patterns of Z_{eH} and Z_{DR} are different and uncorrelated. These differences once again appear to be due to the differences in beam sampling of the deeper clouds present, with a mean max top of 3.9 km. This is also supported by the presence of higher reflectivities near the northern shores of Lake Ontario, as compared with KBUF. In this area the beam height at CWKR is much lower than KBUF.

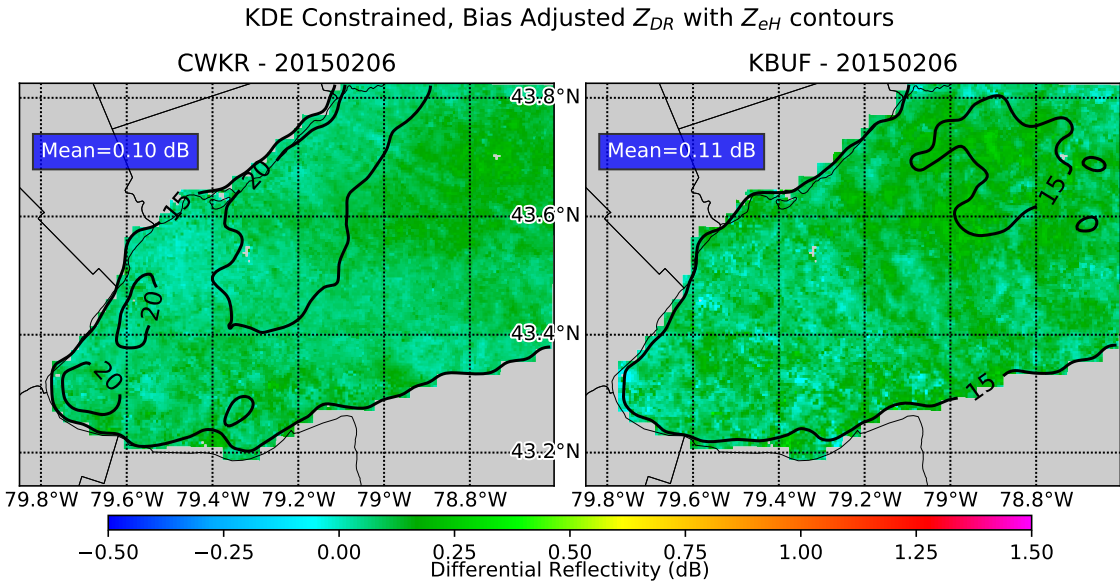


Figure 3.48: Comparison of gridded Z_{DR} with Gaussian ($\sigma = 3$) smoothed contours of Z_{eH} for 6 February 2015. Z_{DR} is constrained by only including points with a KDE ≥ 2 , and is bias-adjusted using the offset calculated in the first section of Chapter 3.

3.3.2.3 14 February 2015

With similar mean values and patterns of Z_{DR} as shown in Figure 3.49, the bias was successfully removed in this case. Once again, the differences lie in the reflectivity fields. Looking back at Figure 3.25, it is seen that CWKR samples a shallow lake-effect band which KBUF overshoots. In terms of predominant hydrometeor type, slightly oblate, dry aggregated snow dominates, with values closer to 0.2 dB than 0 dB.

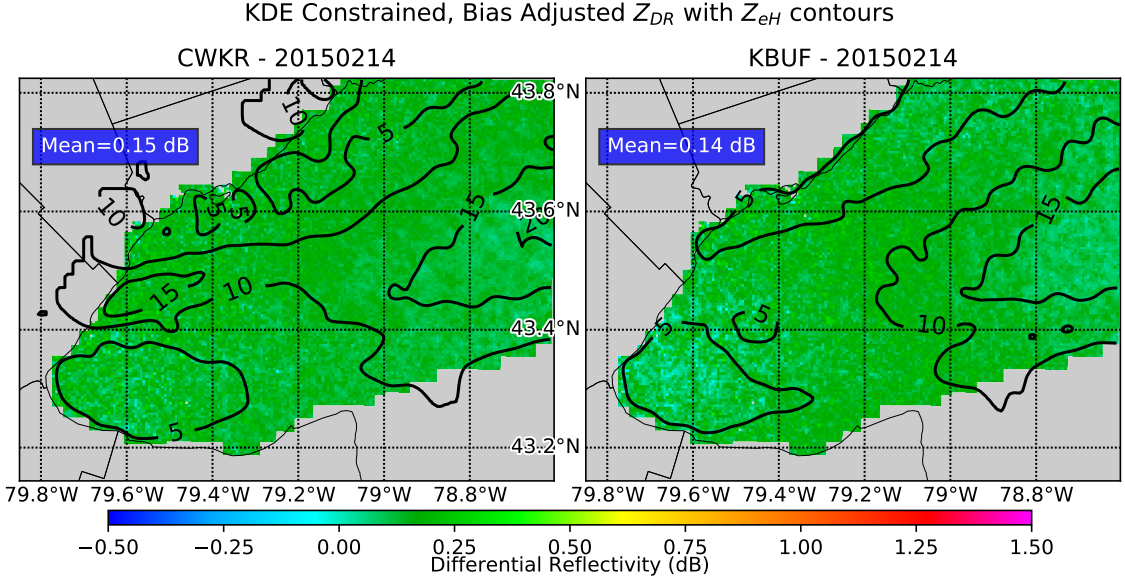


Figure 3.49: Comparison of gridded Z_{DR} with Gaussian ($\sigma = 3$) smoothed contours of Z_{eH} for 14 February 2015. Z_{DR} is constrained by only including points with a KDE ≥ 2 , and is bias-adjusted using the offset calculated in the first section of Chapter 3.

3.3.2.4 18 February 2015

In this case, the mean values of Z_{DR} are exactly the same, but the range of values at CWKR are much smaller than KBUF. The root cause of the bias likely comes down to differences in beam volume, with KBUF sampling a larger variation of hydrometeors in its larger volume, while CWKR cuts through the core. In contrast with other biased cases, the Z_{eH} fields are correlated with the Z_{DR} fields in this case. The higher Z_{DR} values present in this case (0.3-0.5 dB) would suggest a mix of pristine crystals with aggregates, with more aggregates present in the main band.

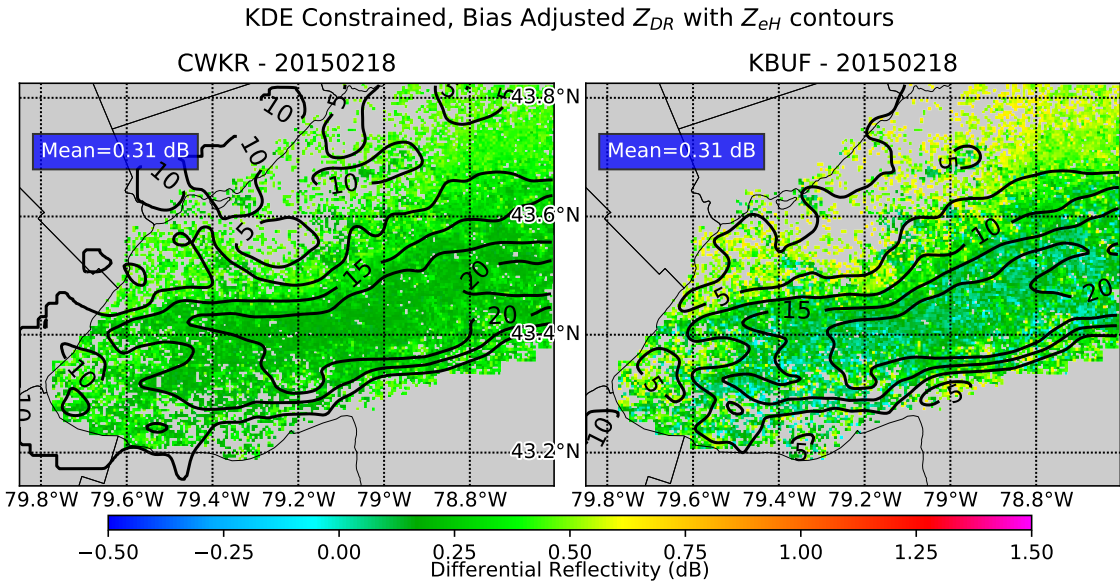


Figure 3.50: Comparison of gridded Z_{DR} with Gaussian ($\sigma = 3$) smoothed contours of Z_{eH} for 18 February 2015. Z_{DR} is constrained by only including points with a KDE ≥ 2 , and is bias-adjusted using the offset calculated in the first section of Chapter 3.

3.3.2.5 15 December 2016

Finally, the last biased case is presented in Figure 3.51. This case has all the makings of an unbiased case, with matching Z_{eH} and Z_{DR} fields. The main difference lies in the main 15 dBZ band, where KBUF includes a 20 dBZ contour, while CWKR does not. This can once again be explained by large vertical gradients of hydrometeors, with mean max tops extending up to 3.5 km in this case. Mean Z_{DR} values around 0.4 dB are suggestive of mainly pristine crystals, with aggregation occurring in pockets of heavier cells. This case has a precipitable water value of 1.9 mm, the lowest of all the cases, which reinforces this result.

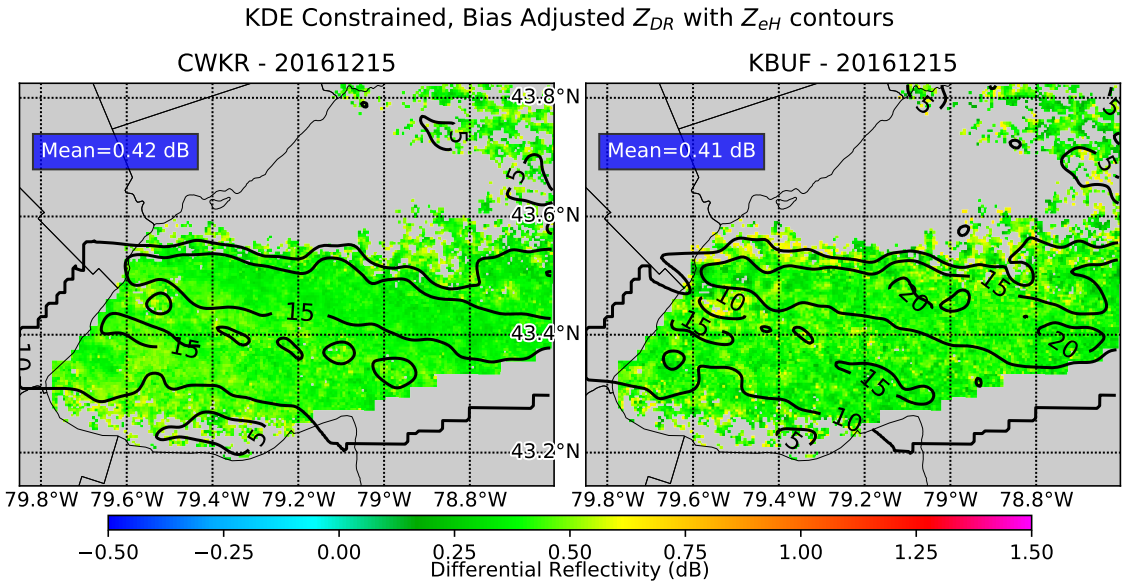


Figure 3.51: Comparison of gridded Z_{DR} with Gaussian ($\sigma = 3$) smoothed contours of Z_{eH} for 15 December 2016. Z_{DR} is constrained by only including points with a KDE ≥ 2 , and is bias-adjusted using the offset calculated in the first section of Chapter 3.

4 Chapter Four

4.1 Discussion

It has been shown that the constrained Z_{DR} datasets aid in determining event biases, which then allows hydrometeor type to be inferred from the unbiased datasets. Now, statistics are compiled, and the probable source of the bias addressed. The relative merit of the two radar systems in observing lake-effect snow is also discussed.

4.1.1 Diagnosing Z_{DR} Bias

The source of the bias could be due to large differences in beam volumes between radars, in combination with a large gradients of Z_{DR} with height. A similiar result was found by (Ryzhkov 2007), in that cross-beam gradients of Z_{DR} can produce significant biases. Modeling the beam as a Gaussian function, Equation 4.1 gives the solid angle of the beam, as a function of beamwidth θ (Probert-Jones 1962).

$$\Omega = \int \int f^2(\theta) d\omega \approx \frac{\pi\theta^2}{8 \ln 2} \quad (4.1)$$

$$V = \frac{\Omega}{4\pi} * \frac{4}{3}\pi r^3 \quad (4.2)$$

Equation 4.2 describes how the beam broadens as range (r) increases. This combined with differing Ω creates the large difference in beam volumes between radars, as shown in Figure 4.1.

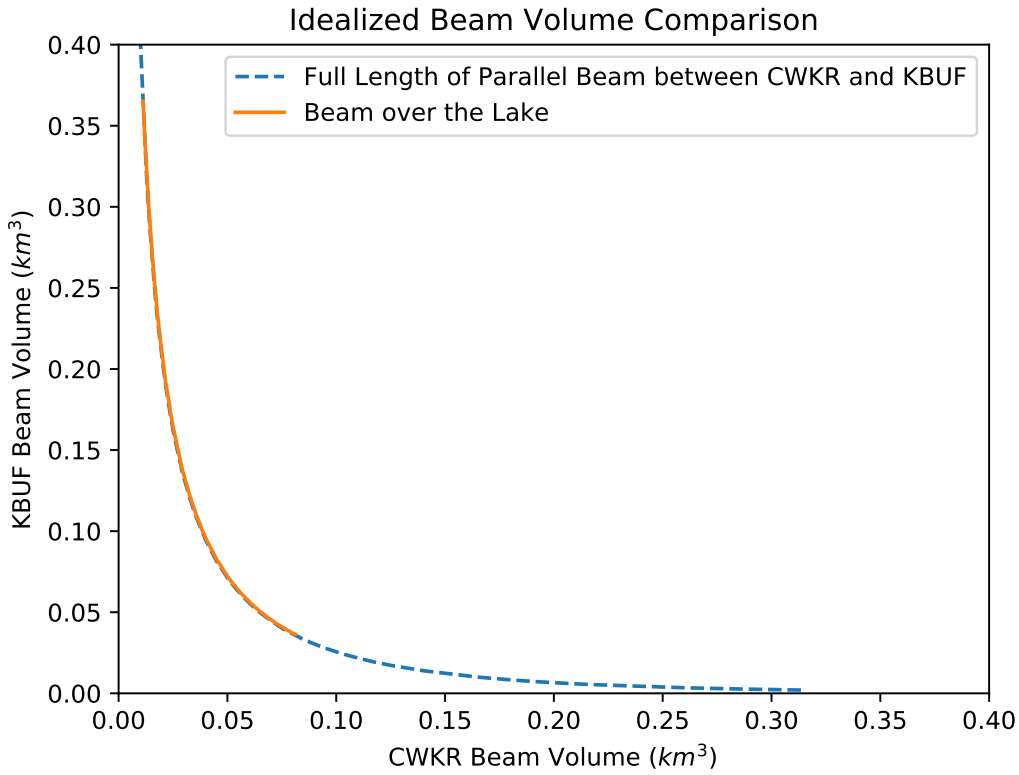


Figure 4.1: Gate-by-gate idealized beam volume comparison along a straight line between radars, assuming Gaussian beam functions.

As to why only certain cases are biased, it is likely due to these cases containing deeper, more intense precipitation, with more opportunity for intra-cloud variations, e.g. ongoing aggregation. As shown in Table 4.1, biased cases contain precipitating structures that are on average 1.1 km deeper than unbiased cases. Furthermore, biased cases are shown to be more intense, with average Z_{eH} values 2-3 dBZ greater than unbiased cases. Another result that supports this is found by comparing the range of Z_{DR} values present in each case. As shown in Figure 4.2, the biased cases tend towards a larger range of values than unbiased.

Table 4.1: Comparing depth and intensity of unbiased and biased cases, where the overbar indicate global means.

Unbiased Cases			
Event	Echo Top (km)	CWKR $\overline{Z_{eH}}$ (dBZ)	KBUF $\overline{Z_{eH}}$ (dBZ)
2014-01-18	2.4	10	11
2014-01-23	1.9	14	14
2015-01-06	0.5	11	8
2015-01-07	3.2	18	17
2016-02-10	1.9	12	15
Mean	2.0	13	13
Biased Cases			
2014-02-01	4.3	17	18
2015-02-06	3.9	19	16
2015-02-14	2.1	14	11
2015-02-18	1.9	17	16
2016-12-15	3.5	13	14
Mean	3.1	16	15

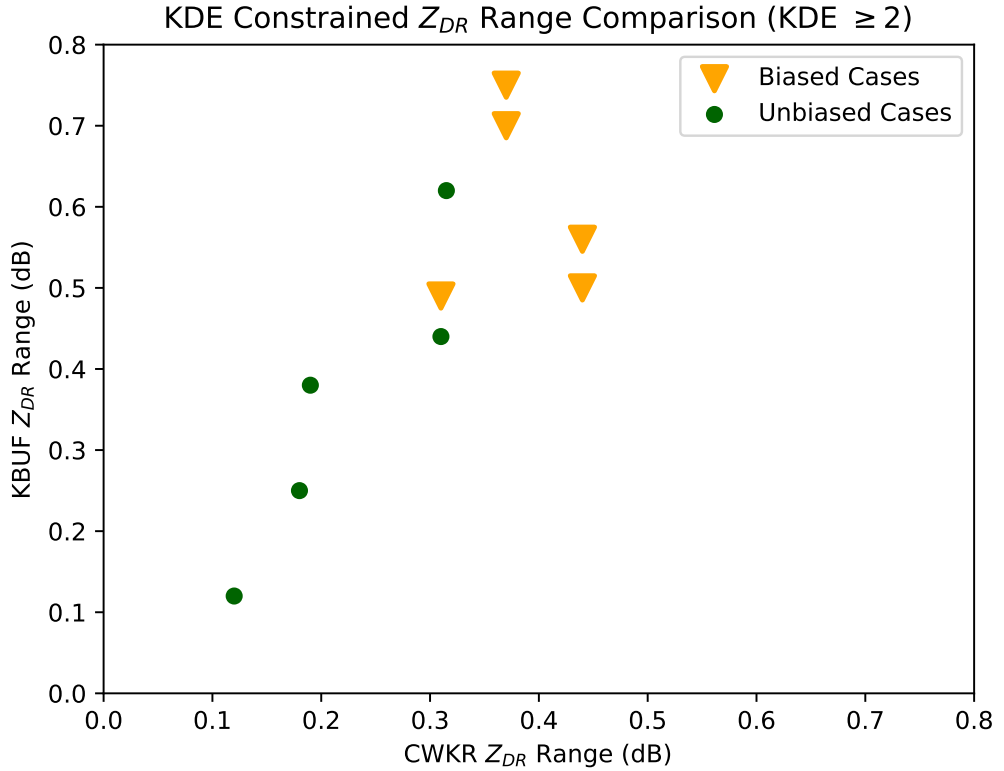


Figure 4.2: Comparison of the range of Z_{DR} (max-min) values observed for each case, with biased cases depicted with yellow triangles and unbiased as green dots.

4.1.2 Z_{DR} Statistics

A statistical comparison of synoptic and lake-effect cases is made in Table 4.2. Both types of events show very similar mean values, with both radars indicating 0.2 dB for lake-effect and 0.3 dB for synoptic. This suggests that synoptic events tend more towards pristine snow crystals, while lake-effect events contain more aggregated snow. While the mean values match between radars, it is shown that KBUF yields a larger range of Z_{DR} regardless of the type of event. A wider beamwidth could aid in the detection of a larger variety of hydrometeor types.

Table 4.2: Bias-adjusted Z_{DR} Statistics, comparing synoptic and lake-effect events

Synoptic Events										
	CWKR Z_{DR} (dB)					KBUF Z_{DR} (dB)				
Event	Bias	Min	Mean	Max	Range	Bias	Min	Mean	Max	Range
2014-01-18	-0.10	0.2	0.3	0.5	0.3	-0.40	0.2	0.4	0.7	0.5
2014-02-01	0.22	0.0	0.2	0.5	0.5	-0.20	0.0	0.5	0.5	0.5
2015-01-07	-0.04	0.1	0.3	0.4	0.3	-0.30	0.0	0.3	0.6	0.6
2015-02-06	0.28	0.0	0.1	0.3	0.3	0.00	-0.1	0.1	0.4	0.5
2016-12-15	-0.47	0.2	0.3	0.6	0.4	-0.28	-0.3	0.4	0.5	0.8
Mean	–	0.1	0.3	0.5	0.4	–	0.0	0.3	0.5	0.5
Lake-Effect Events										
2014-01-23	-0.06	0.0	0.1	0.2	0.2	-0.40	0.0	0.2	0.3	0.3
2015-01-06	0.00	0.4	0.5	0.6	0.2	-0.10	0.4	0.5	0.7	0.3
2015-02-14	0.38	-0.1	0.2	0.4	0.5	-0.10	-0.1	0.1	0.4	0.5
2015-02-18	0.30	0.1	0.3	0.5	0.4	-0.10	-0.1	0.3	0.7	0.8
2016-02-10	-0.04	-0.1	0.0	0.1	0.2	0.40	0.0	0.0	0.1	0.1
Mean	–	0.1	0.2	0.4	0.3	–	0.0	0.2	0.4	0.4

4.1.3 Relative Merits of C-Band vs. S-Band in Lake-Effect Snow

The results have shown that the wider beamwidth of S-Band may contribute to the detection of a higher diversity of hydrometeors per sampling volume. This becomes more critical for mixed phases of precipitation, but for pure snow is not as relevant. For quantitative precipitation purposes this becomes more relevant, as the shape

of the snow crystals can give insights into their density, providing a better estimate of snow-to-liquid ratios. Furthermore, comparing values of Z_{eH} in lake-effect snow events versus synoptic events has shown that C-Band radar has a slight advantage in detecting shallow snow-squalls.

5 Chapter Five

5.1 Conclusions

The Greater Golden Horseshoe region in Southern Ontario is highly susceptible to lake-effect snow. C-Band radar is the current tool used to observe and nowcast these events in real-time. This tool will soon be replaced by S-Band radar, with its wider beamwidth and higher elevation angles similiar to KBUF. A case study comparing lake effect snow events, with synoptic snow events used a control, has been undertaken to assess the relative merits of these two types of radar systems. With the data transformed to a common grid, the base variables of two neighboring radars in this region are compared. These two radars are Environment and Climate Change Canada's King City C-Band radar and the National Weather Service's Buffalo, NY S-Band radar. Comparisons indicate that these radars are calibrated well relative to one another, as the bias-adjusted values for both Z_{eH} and Z_{DR} are similiar. In terms of Z_{eH} , subset comparisons indicate that the higher elevation angle of the S-Band radar leads to overshooting, and slight underestimation of the strength of the snow-squall. This problem is especially acute at mid to long ranges. The difference is small enough that it does not limit forecasters ability to nowcast for these events. For Z_{DR} , S-Band radar shows advantages over C-Band in comparatively observing a larger range of values due to a larger beam volume. In terms of hydrometeor types observed in lake-effect snow versus synoptic snow,

aggregated snow is more prevalent in lake-effect events. Also, multi-modal distributions of hydrometeors appear more often in more intense snowfall events. These findings are enhanced by estimating joint probability density functions of matched variables. It is shown that this method can reduce noise and improve the quality of the data, by removing erroneous data caused by partial beam blockages, low SNR, temporal and spatial mismatching, and even transmit and receive errors. The KDE constraint method essentially distills the massive amount of information which radars provide to the most valuable areas for meteorological interests.

A Appendix A

A.1 Upper-Air Charts

Images provided by the NOAA/ESRL Physical Science Division, Boulder, Colorado.

Original data can be found at <http://www.esrl.noaa.gov/psd/>.

A.2 Skew-T Charts

Raw sounding data provided by the Department of Atmospheric Science at the University of Wyoming. Original data can be found at <http://weather.uwyo.edu/upperair/sounding.html>.

A.3 Sounding Climatology

Images provided by the National Weather Service Storm Prediction Center in Norman, Oklahoma. Original data can be found at <http://www.spc.noaa.gov/exper/soundingclimo/>.

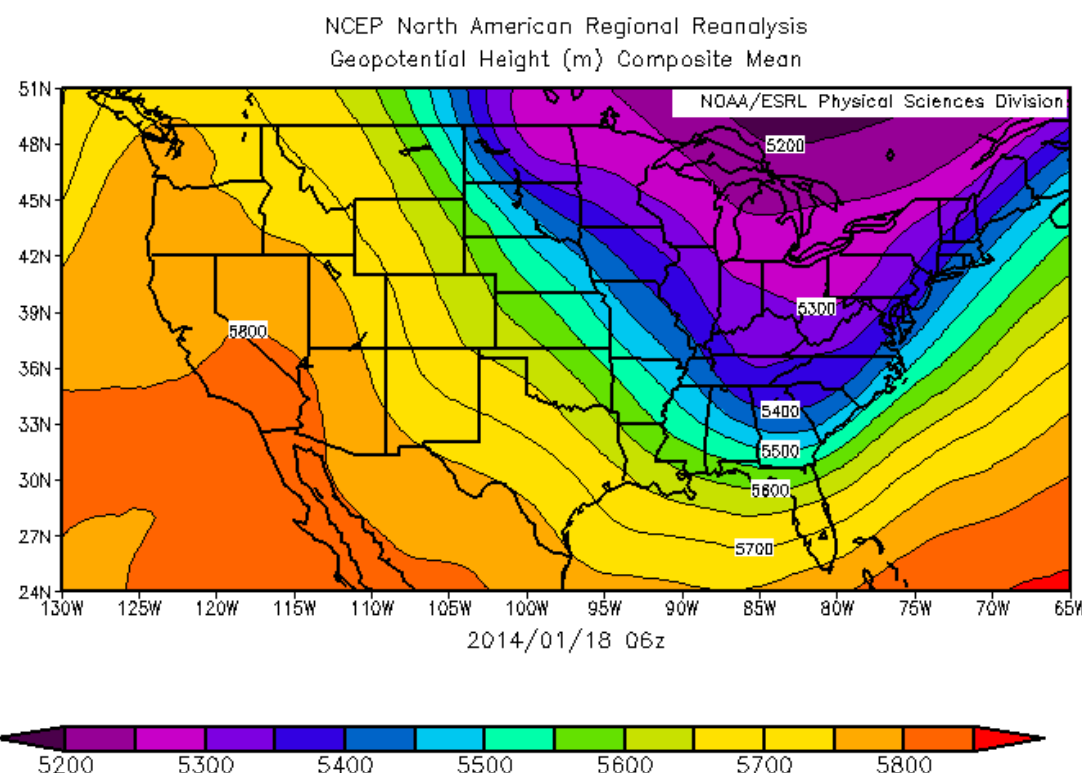


Figure A.1: 500mb Geopotential Height at 06Z 18 January 2014.

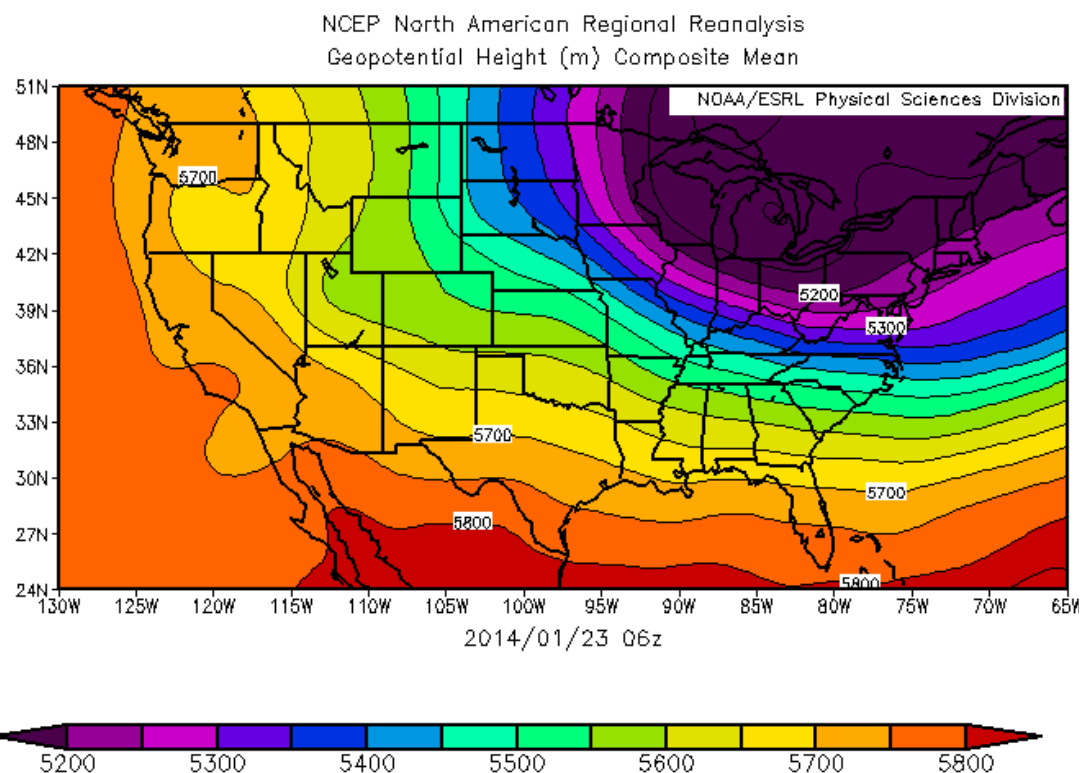


Figure A.2: 500mb Geopotential Height at 06Z 23 January 2014

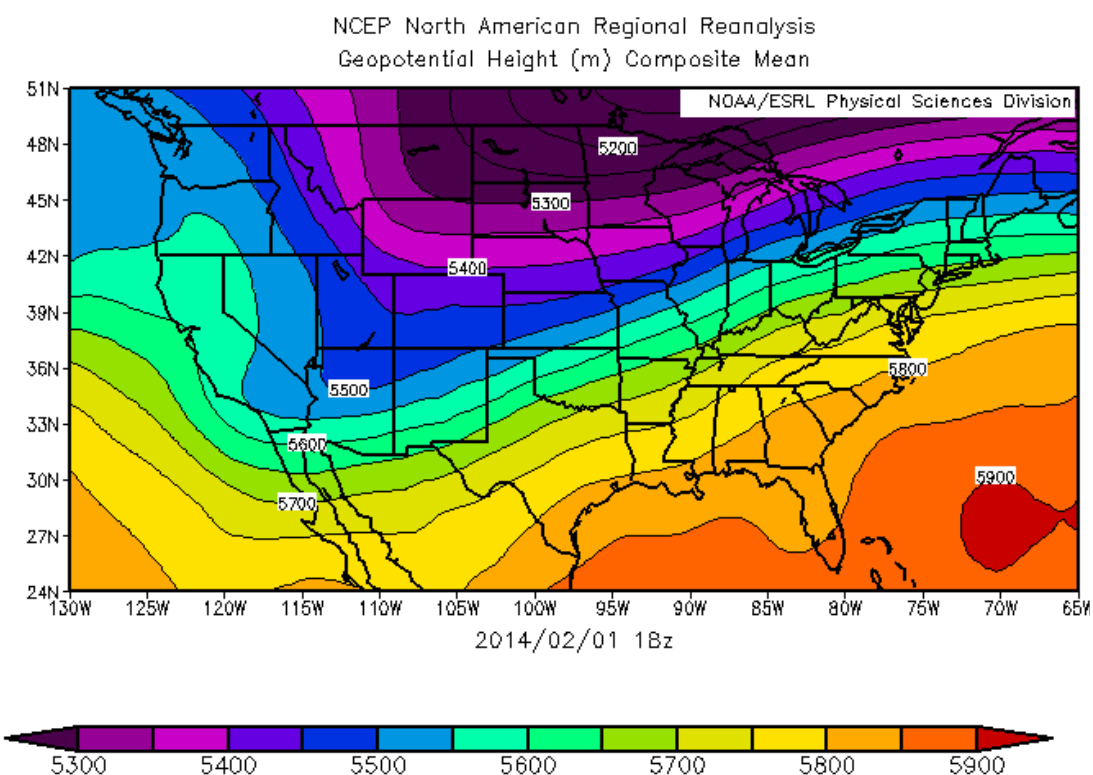


Figure A.3: 500mb Geopotential Height at 18Z 1 February 2014.

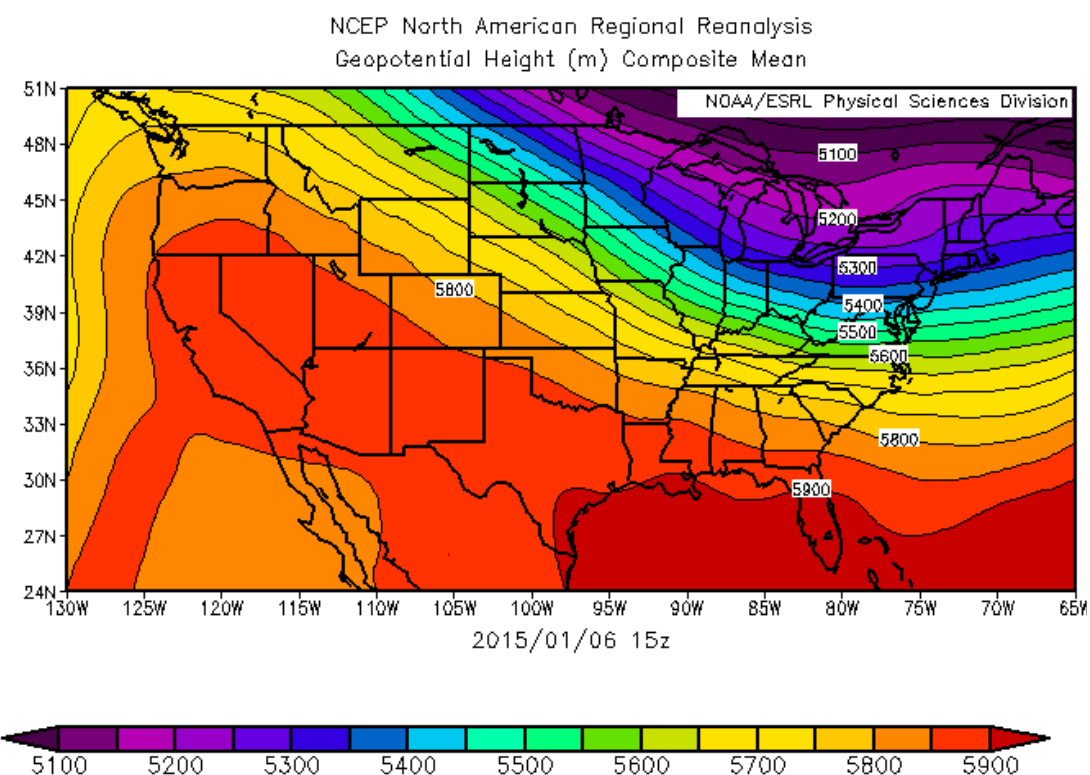


Figure A.4: 500mb Geopotential Height at 15Z 6 January 2015.

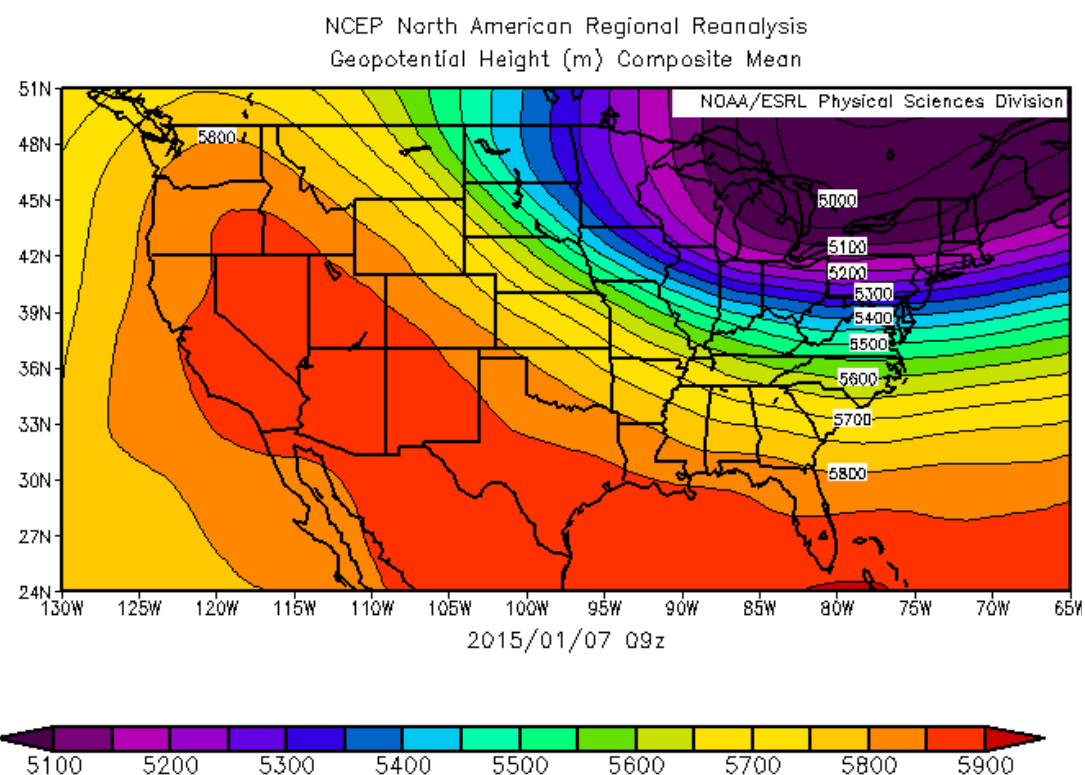


Figure A.5: 500mb Geopotential Height at 09Z 7 January 2015.

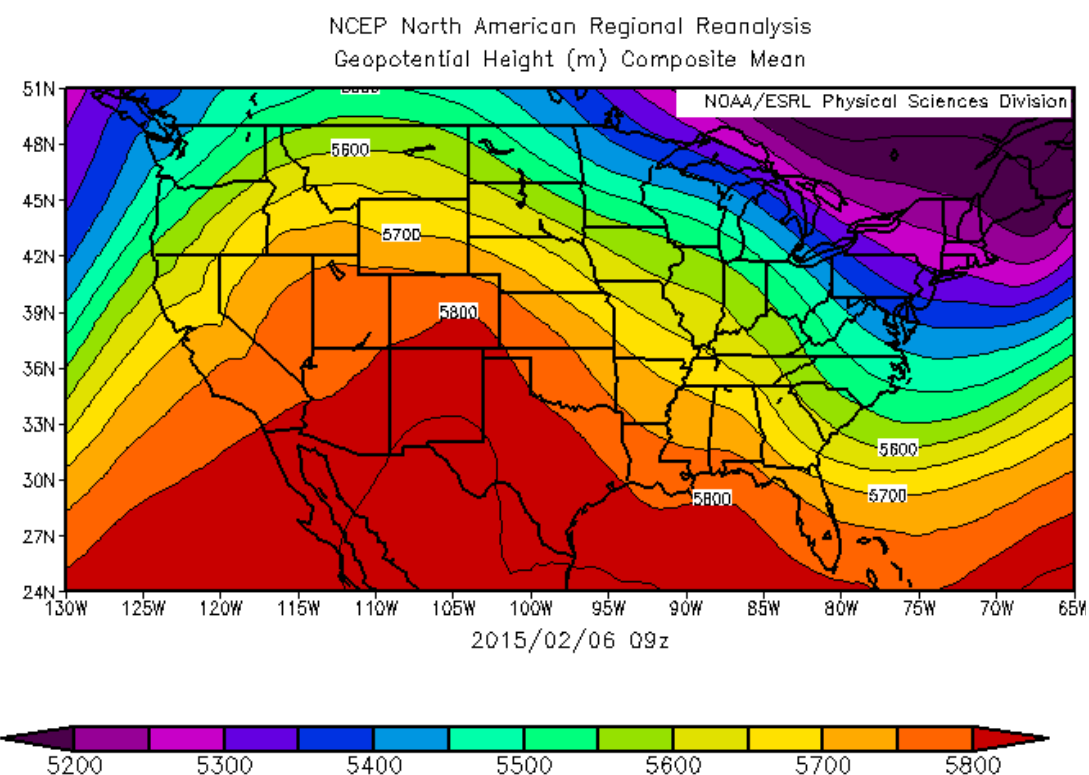


Figure A.6: 500mb Geopotential Height at 09Z 6 February 2015.

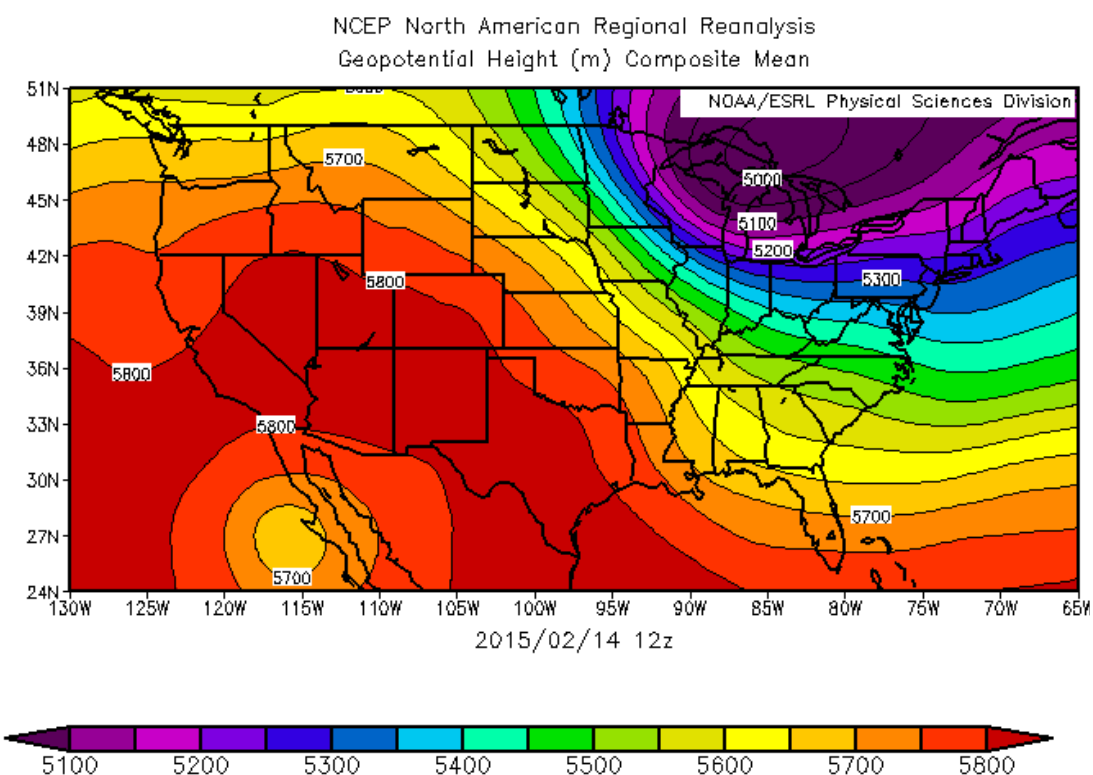


Figure A.7: 500mb Geopotential Height at 12Z 14 February 2015.

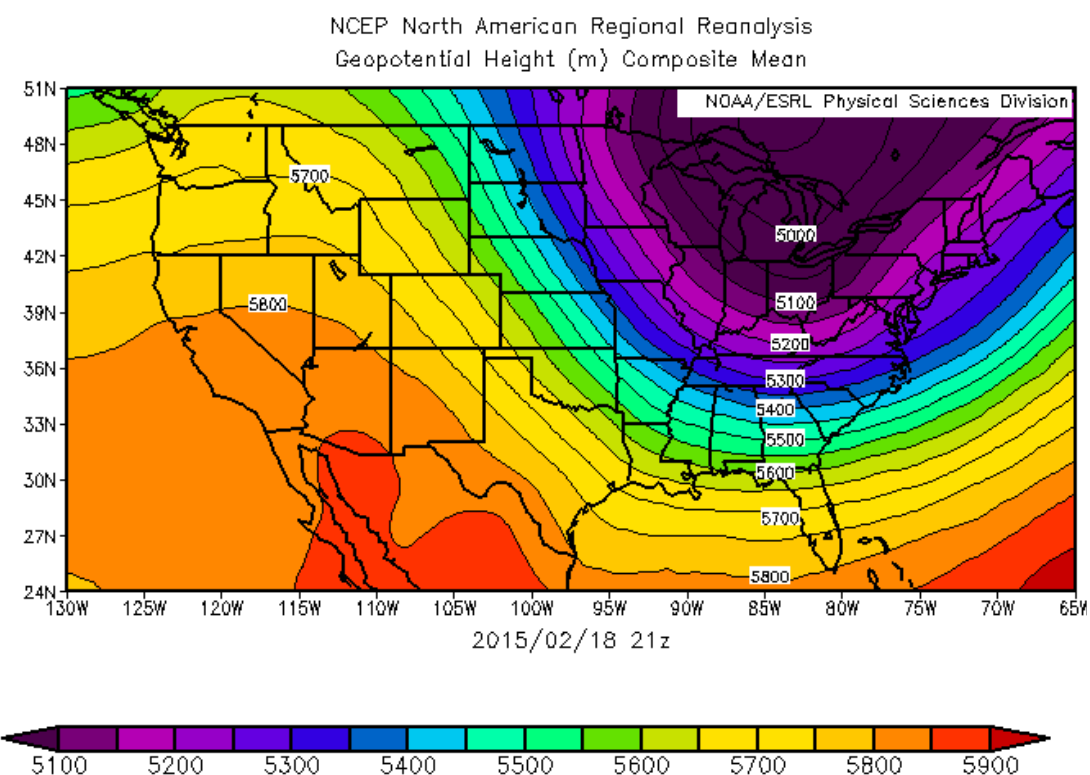


Figure A.8: 500mb Geopotential Height at 21Z 18 February 2015.

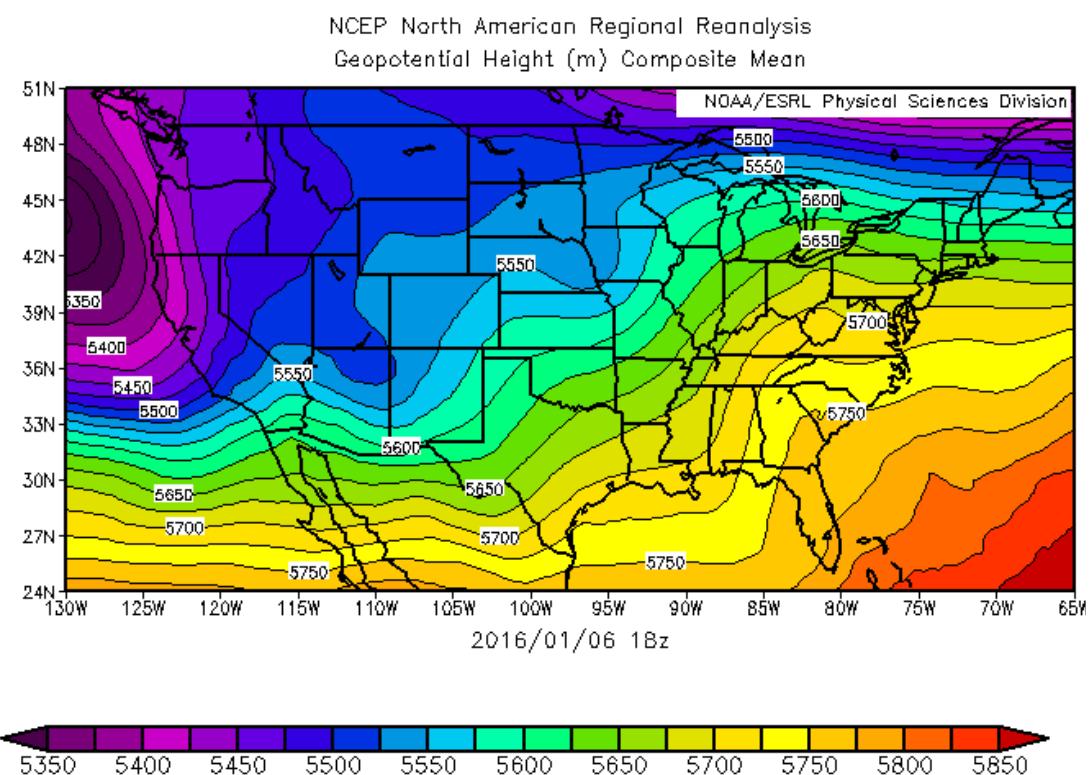


Figure A.9: 500mb Geopotential Height at 18Z 10 February 2016.

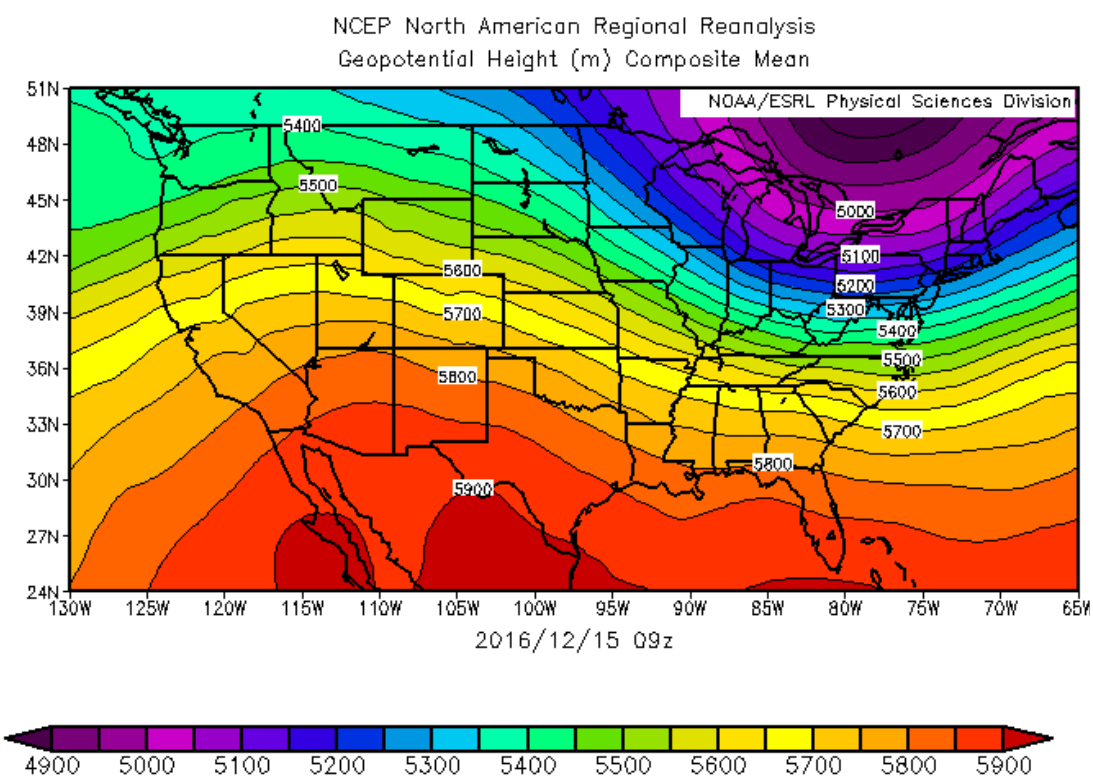


Figure A.10: 500mb Geopotential Height at 09Z 15 December 2016.

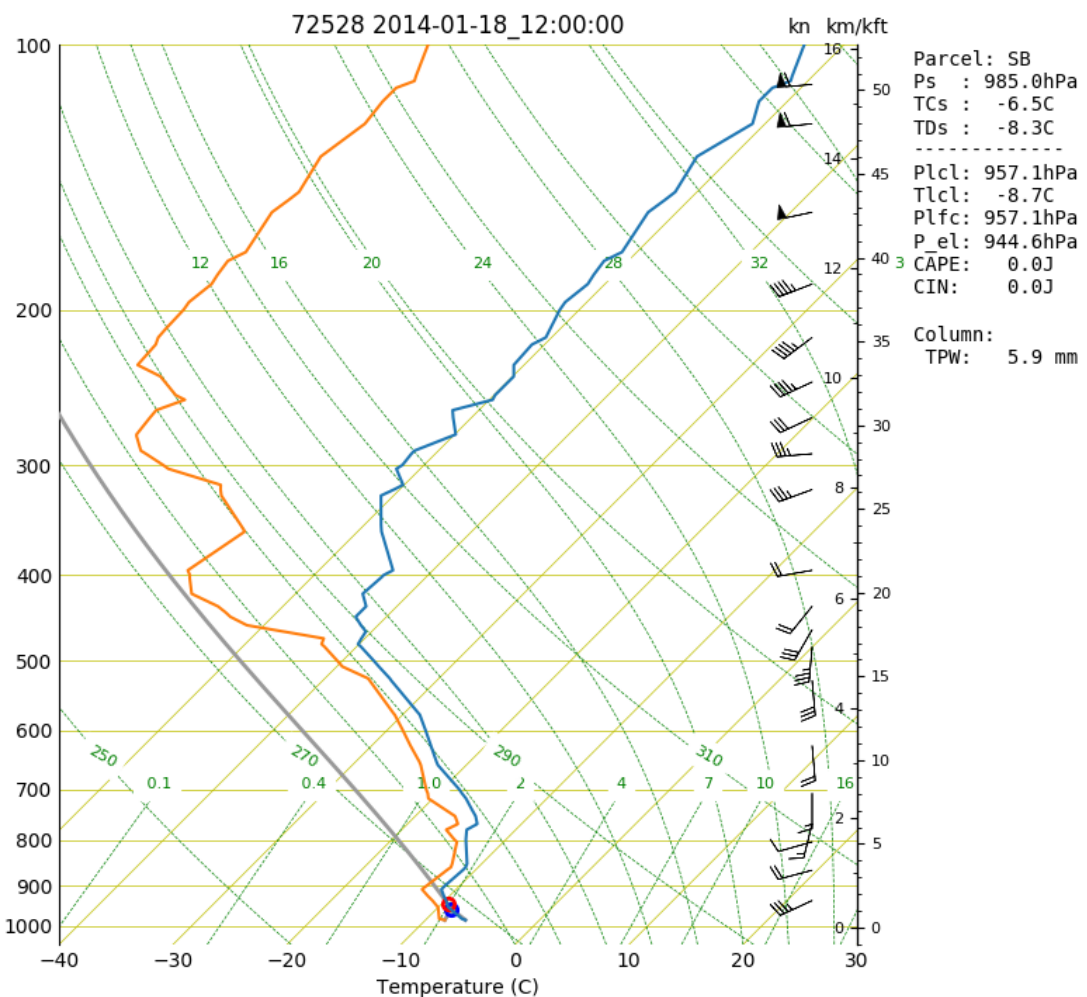


Figure A.11: SkewT/Log-P Chart from the BUF Radiosonde launched at 12Z 18 January 2014

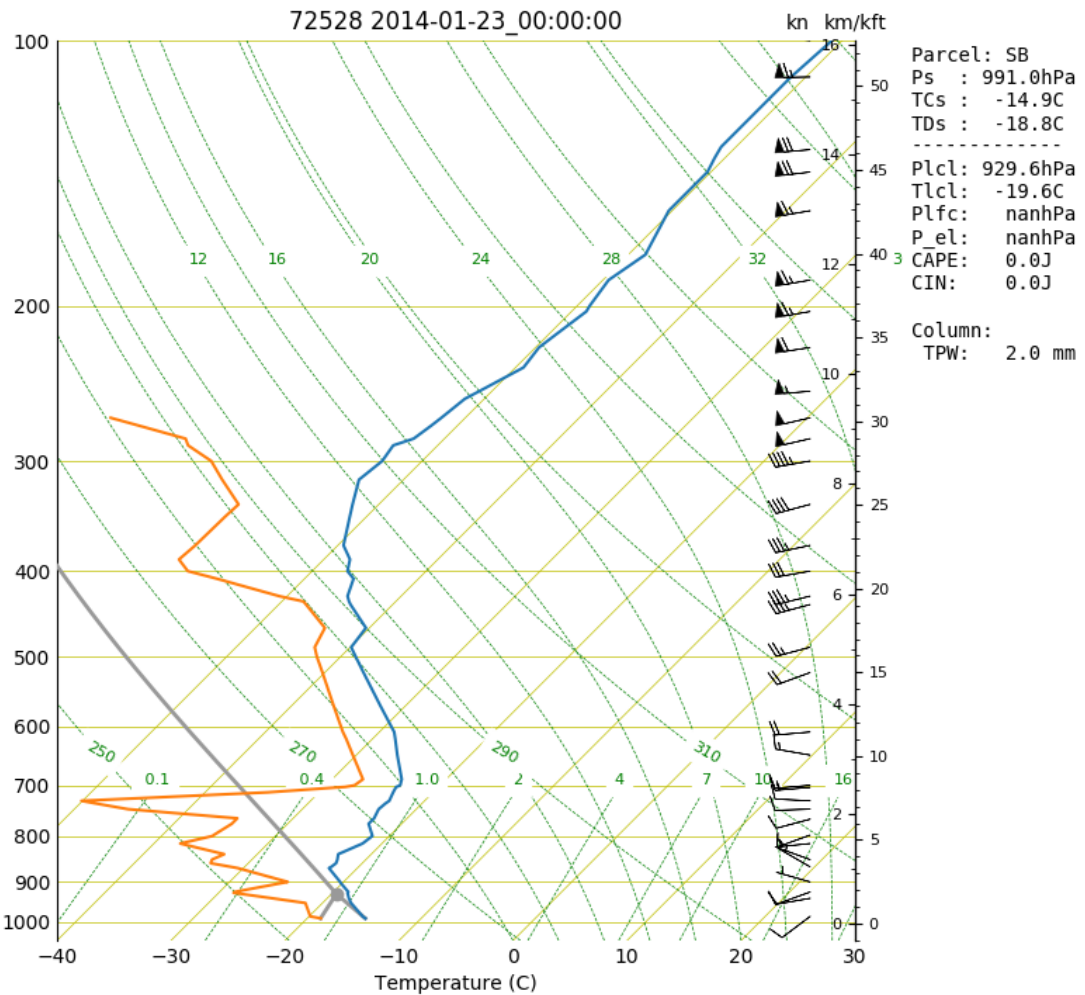


Figure A.12: SkewT/Log-P Chart from the BUF Radiosonde launched at 00Z 23 January 2014

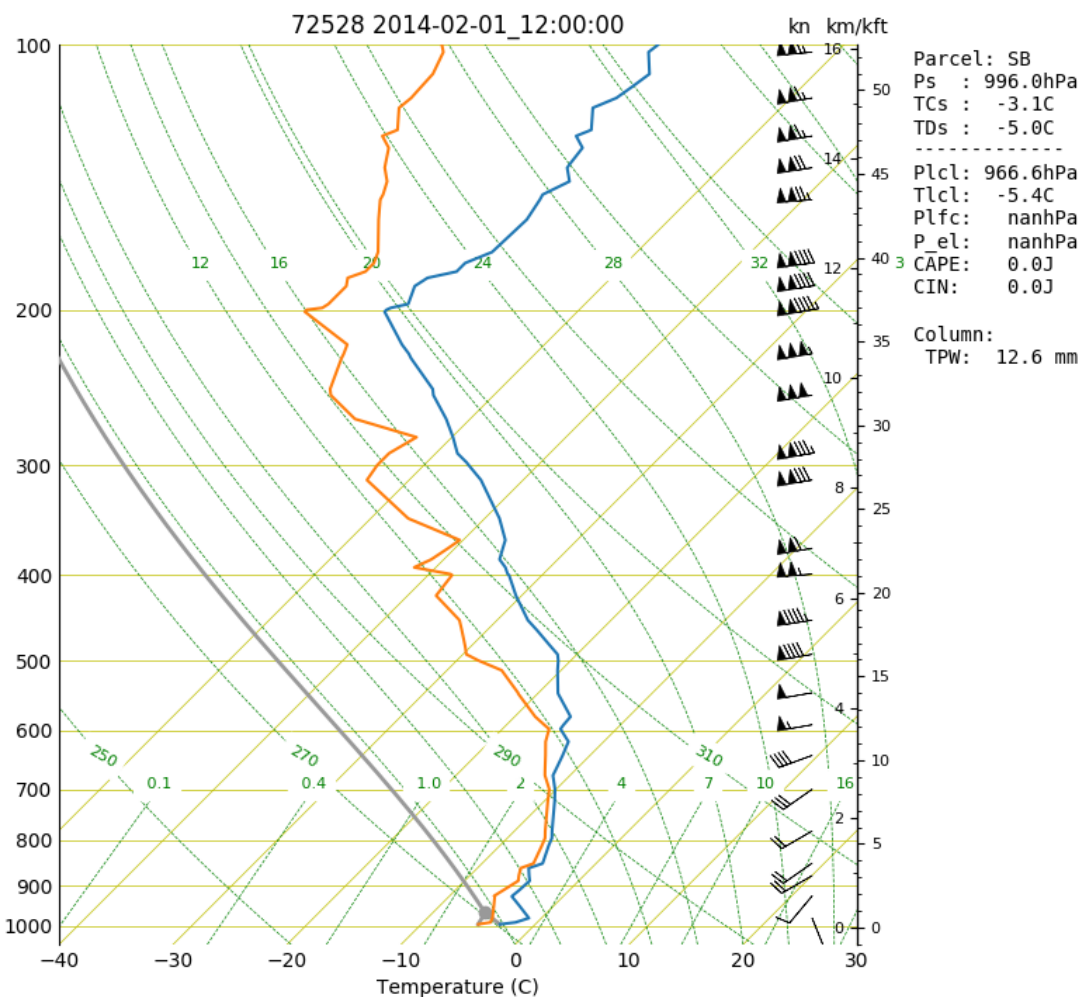


Figure A.13: SkewT/Log-P Chart from the BUF Radiosonde launched at 12Z 1

February 2014

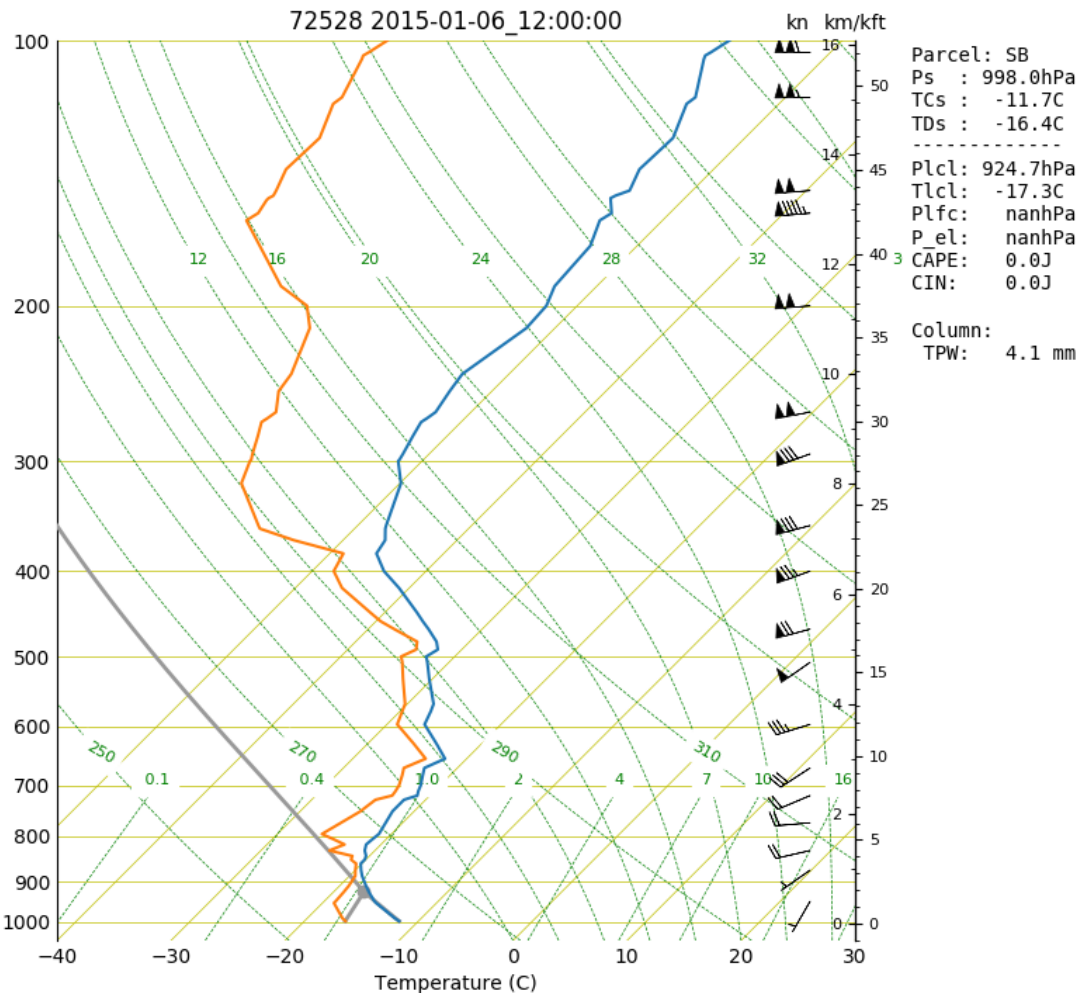


Figure A.14: SkewT/Log-P Chart from the BUF Radiosonde launched at 00Z 6 January 2015

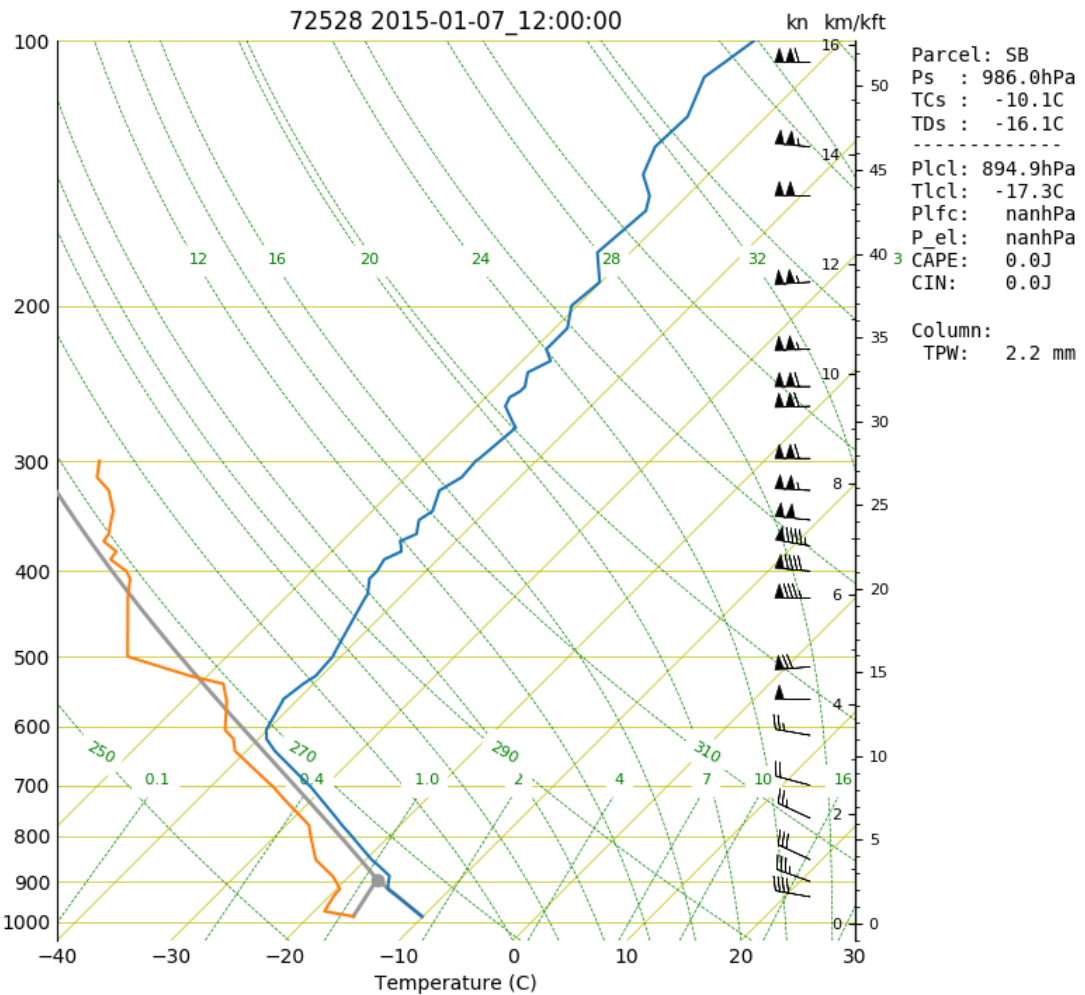


Figure A.15: SkewT/Log-P Chart from the BUF Radiosonde launched at 12Z 7 January 2015

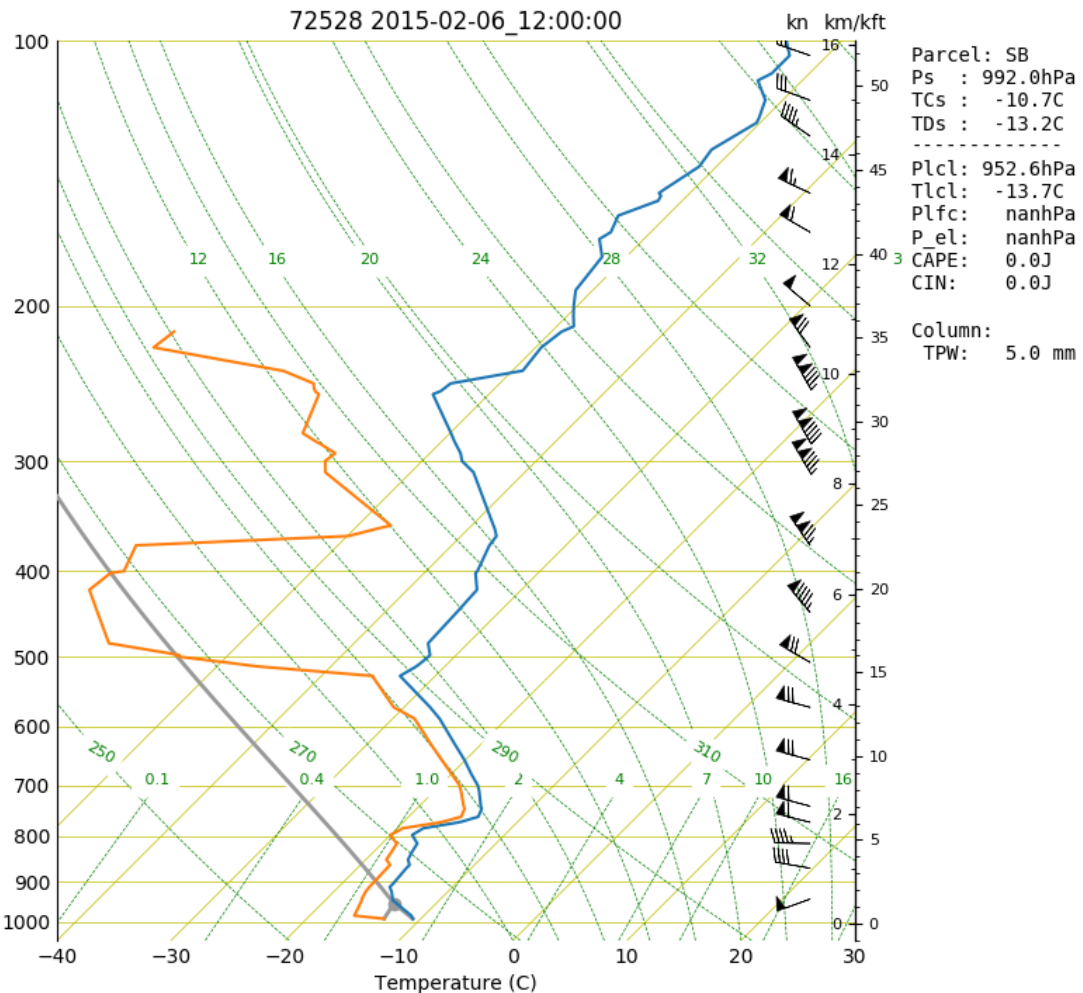


Figure A.16: SkewT/Log-P Chart from the BUF Radiosonde launched at 00Z 6 February 2015

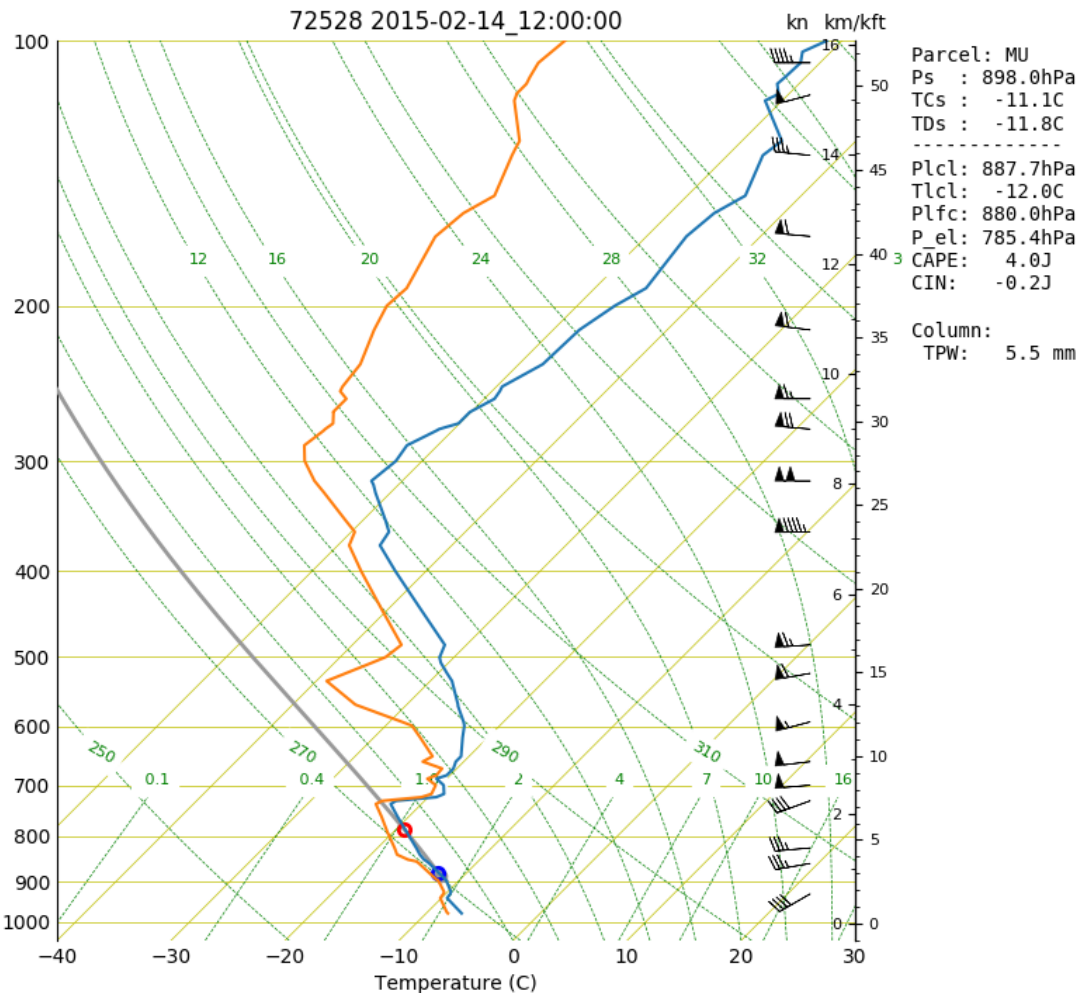


Figure A.17: SkewT/Log-P Chart from the BUF Radiosonde launched at 12Z 14 February 2015

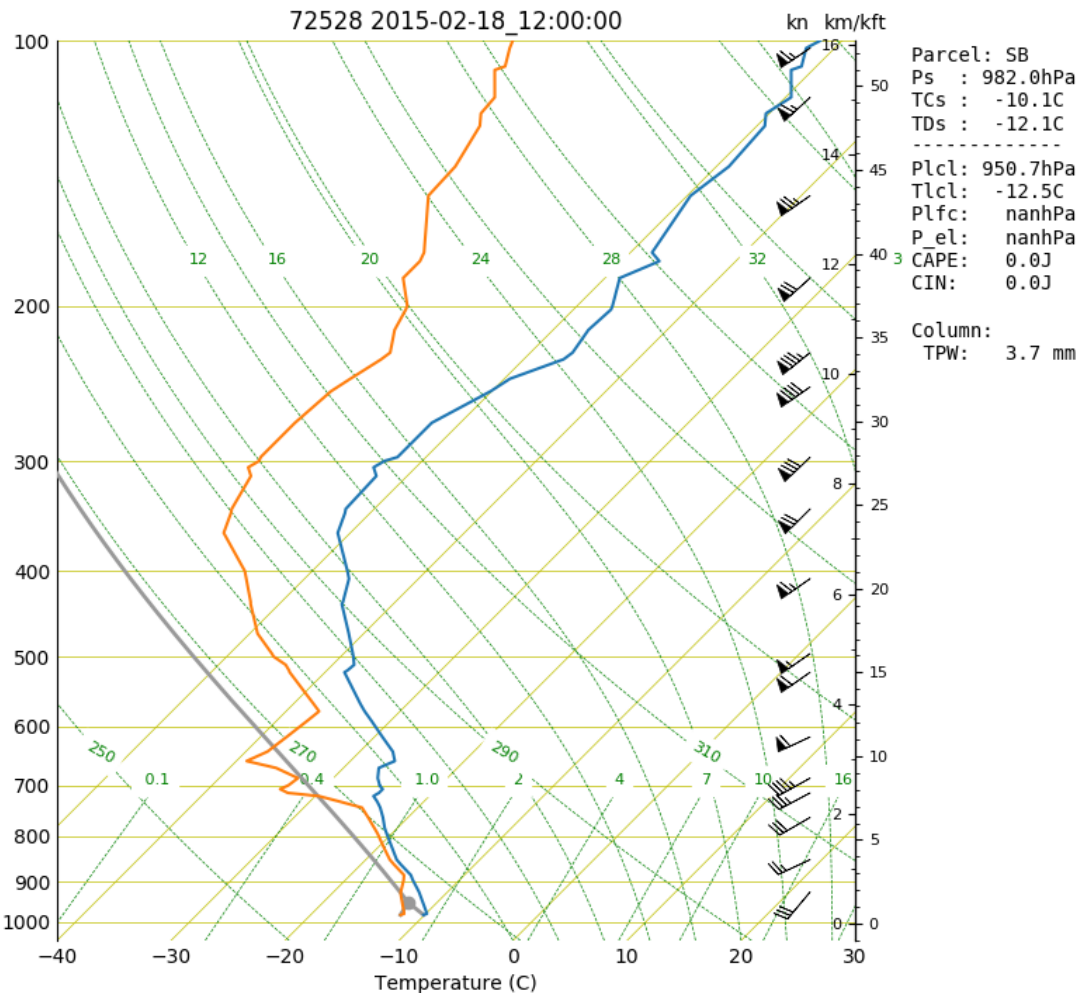


Figure A.18: SkewT/Log-P Chart from the BUF Radiosonde launched at 00Z 18 February 2015

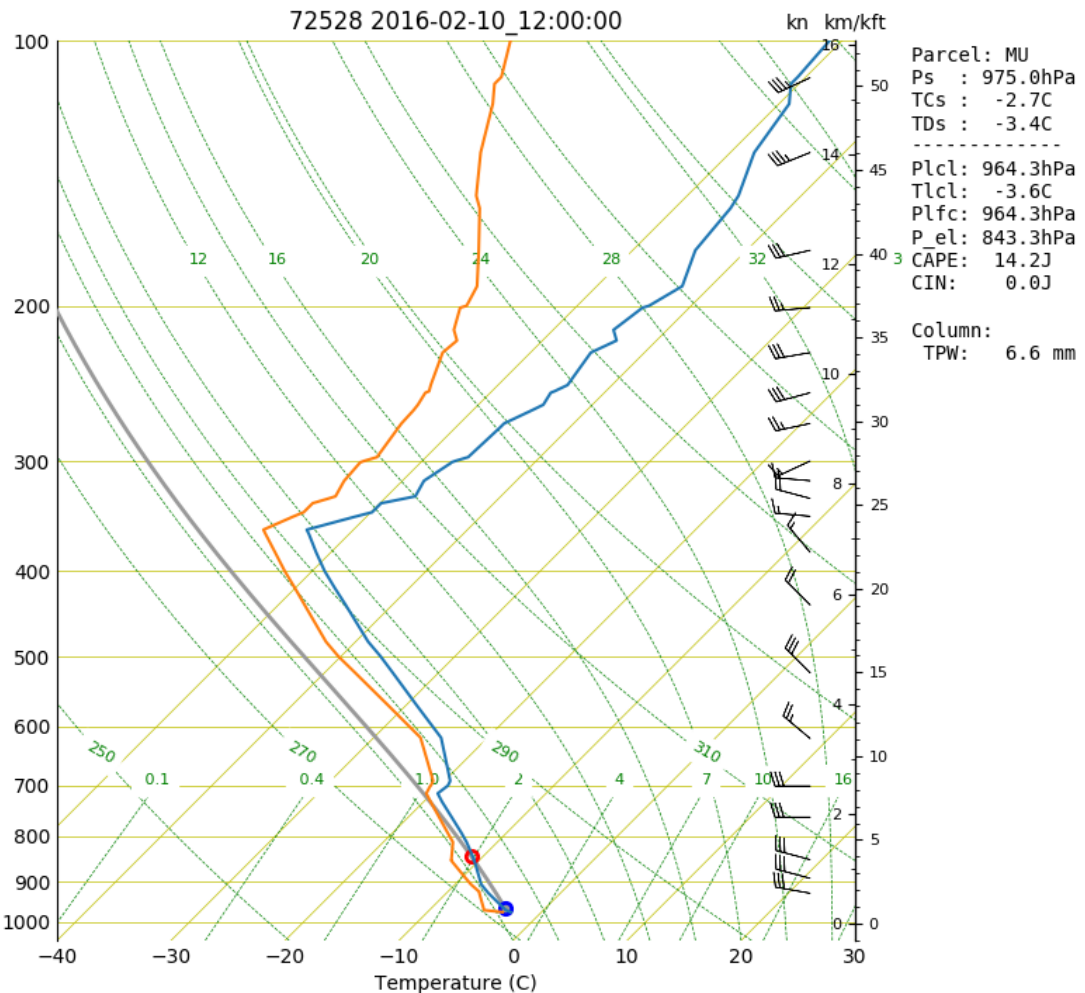


Figure A.19: SkewT/Log-P Chart from the BUF Radiosonde launched at 12Z 10

February 2016

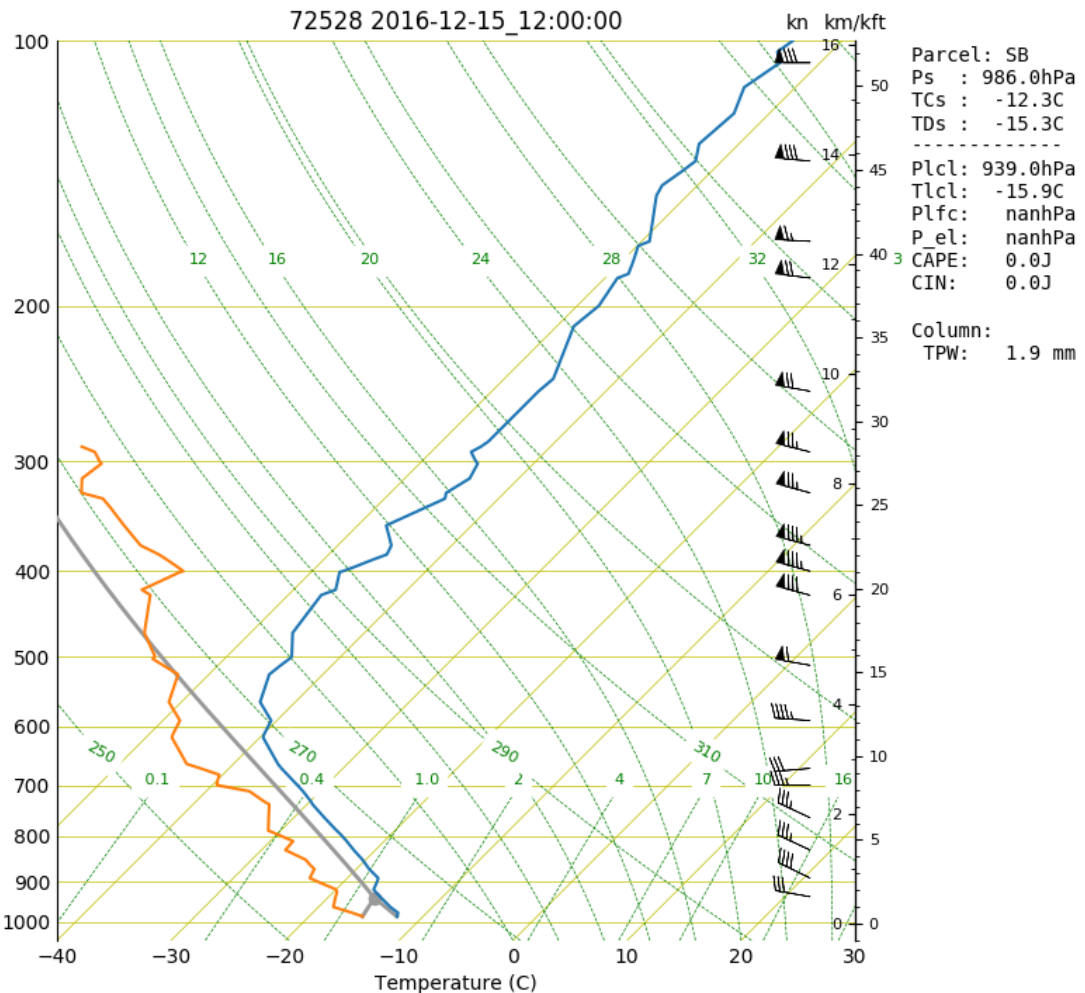


Figure A.20: SkewT/Log-P Chart from the BUF Radiosonde launched at 12Z 15

December 2016

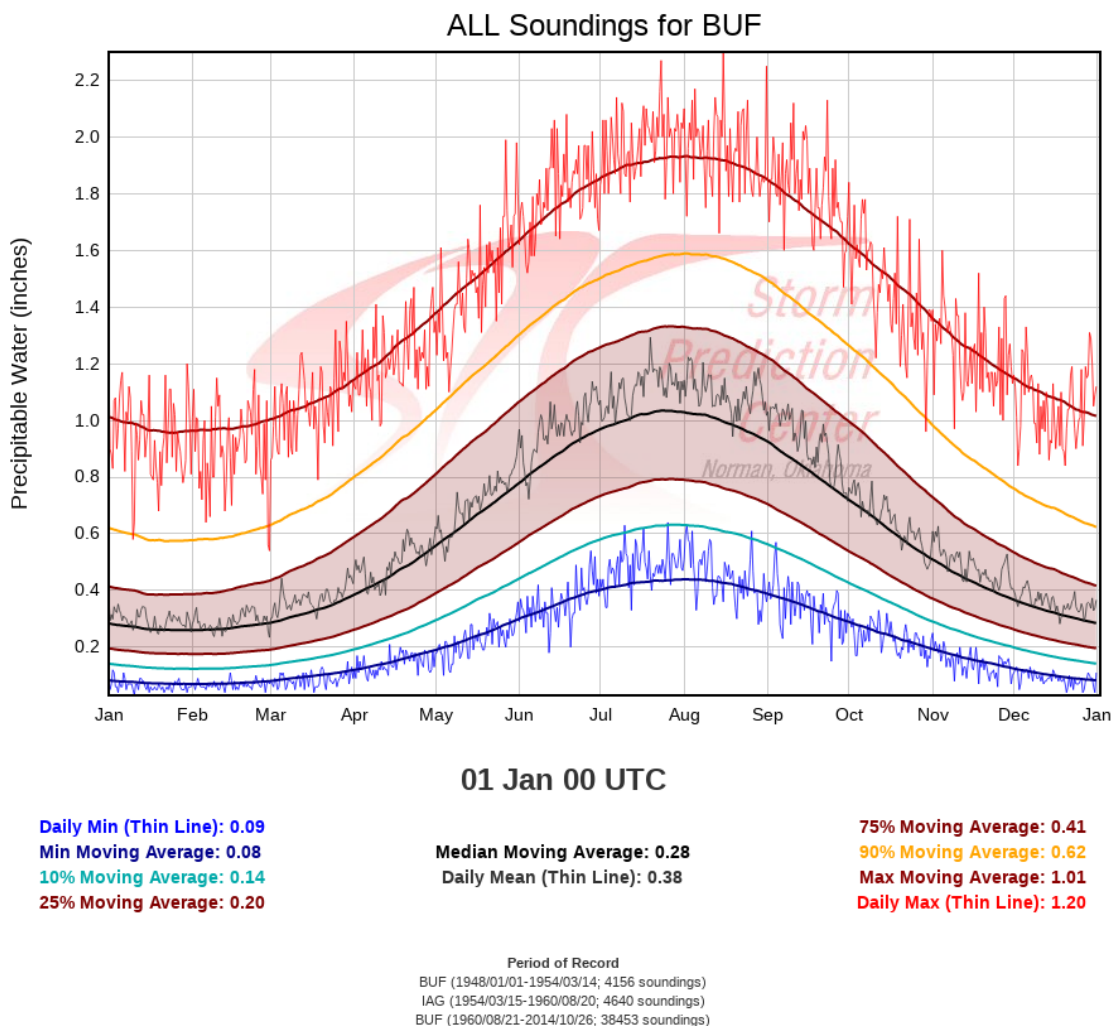


Figure A.21: Sounding Precipitable Water Climatology for BUF

References

- Abon, C., I. Crisologo, D. Kneis, A. Bronstert, and M. Heistermann, 2014: *Comparison between C-band and S-band radar rainfall for hydrological simulations in Marikina River Basin, Philippines*, URL https://www.researchgate.net/publication/268147287_Comparison_between_C-band_and_S-band_radar_rainfall_for_hydrological_simulations_in_Marikina_River_Basin_Philippines.
- Boodoo, S., D. Hudak, A. Ryzhkov, P. Zhang, N. Donaldson, D. Sills, and J. Reid, 2015: Quantitative Precipitation Estimation from a C-Band Dual-Polarized Radar for the 8 July 2013 Flood in Toronto, Canada. *Journal of Hydrometeorology*, **16** (5), 2027–2044, URL <https://doi.org/10.1175/JHM-D-15-0003.1>.
- Fabry, F., 2015: *Radar Meteorology: Principles and Practice*. Cambridge University Press, 256 pp.
- Hassan, D., P. A. Taylor, and G. A. Isaac, 2017: Snowfall Rate Estimation using C-Band Polarimetric Radars. *Meteor. Appl.*, **24** (1), 142–156, URL <http://doi.org/10.1002/met.1613>.
- Helmus, J. J. and S. M. Collis, 2016: The Python ARM Radar Toolkit (Py-ART), a Library for Working with Weather Radar Data in the Python Programming Language. *JORS*, **4** (1), e25, URL <http://doi.org/10.5334/jors.119>.
- Hosler, C. L., D. C. Jensen, and L. Goldshlak, 1957: On the aggregation of ice crystals to form snow. *Journal of Meteorology*, **14** (5), 415–420, URL [https://doi.org/10.1175/1520-0469\(1957\)014<0415:OTAOIC>2.0.CO;2](https://doi.org/10.1175/1520-0469(1957)014<0415:OTAOIC>2.0.CO;2).
- Hubbert, J. and F. Pratte, 2006: Differential Reflectivity Calibration for Nexrad. *2006 IEEE International Symposium on Geoscience and Remote Sensing*, 519–522, URL <https://doi.org/10.1109/IGARSS.2006.138>.
- Kernen, R., J. Yllsjrvi, R. P. Jr., and J. Selzler, 2008: *Comparison of polarimetric C band Doppler radar observations with reflectivity fields obtained at S band; a case*

- study of water induced attenuation*, URL [https://www.wmo.int/pages/prog/www/IMOP/publications/IOM-96_TEC0-2008/1\(12\)_Keranen_Finland.pdf](https://www.wmo.int/pages/prog/www/IMOP/publications/IOM-96_TEC0-2008/1(12)_Keranen_Finland.pdf).
- Markovsky, I. and S. V. Huffel, 2007: Overview of total least-squares methods. *Elsevier BV*, URL <http://doi.org/10.1016/j.sigpro.2007.04.004>.
- Mulholland, J. P., J. Frame, S. W. Nesbitt, S. M. Steiger, K. A. Kosiba, and J. Wurman, 2017: Observations of misovortices within a long-lake-axis-parallel lake-effect snowband during the owles project. *Monthly Weather Review*, **145** (8), 3265–3291, URL <https://doi.org/10.1175/MWR-D-16-0430.1>.
- Orlanski, I., 1975: A rational subdivision of scales for atmospheric processes. *Bulletin of the American Meteorological Society*, **56** (5), 527–530, URL <http://www.jstor.org/stable/26216020>.
- Pauley, P. M. and X. Wu, 1990: The theoretical, discrete, and actual response of the barnes objective analysis scheme for one- and two-dimensional fields. *Mon. Wea. Rev.*, **118** (5), 1145–1164, URL [http://doi.org/10.1175/1520-0493\(1990\)118<1145:TTDAAR>2.0.CO;2](http://doi.org/10.1175/1520-0493(1990)118<1145:TTDAAR>2.0.CO;2).
- Petersen, W. A., K. R. Knupp, D. J. Cecil, and J. R. Mecikalski, 2007: *The University of Alabama Huntsville THOR Center Instrumentation: Research and Operational Collaboration*, 33rd Intl. Conf. on Radar Met., Cairns, Australia, Amer. Meteor. Soc., 5.1, URL https://ams.confex.com/ams/33Radar/techprogram/paper_123410.htm.
- Probert-Jones, J. R., 1962: The radar equation in meteorology. *Quarterly Journal of the Royal Meteorological Society*, **88** (378), 485–495, URL <https://doi.org/10.1002/qj.49708837810>.
- Rogers, R. and M. Yau, 1989: *A Short Course in Cloud Physics*, Vol. 113. Elsevier, 290 pp.
- Ryzhkov, A. V., 2007: The impact of beam broadening on the quality of radar polarimetric data. *Journal of Atmospheric and Oceanic Technology*, **24** (5), 729–744, URL <https://doi.org/10.1175/JTECH2003.1>.
- Ryzhkov, A. V. and D. S. Zrnić, 2007: Depolarization in ice crystals and its effect on radar polarimetric measurements. *Journal of Atmospheric and Oceanic Technology*, **24** (7), 1256–1267, URL <https://doi.org/10.1175/JTECH2034.1>.
- Scott, D. W., 1992: *Multivariate Density Estimation: Theory, Practice, and Visualization*. John Wiley.

- Silverman, B. W., 1986: *Density Estimation for Statistics and Data Analysis*, Vol. 26. Chapman and Hall, 176 pp.
- Straka, J. M., D. S. Zrnić, and A. V. Ryzhkov, 2000: Bulk hydrometeor classification and quantification using polarimetric radar data: Synthesis of relations. *Journal of Applied Meteorology*, **39** (8), 1341–1372, URL [https://doi.org/10.1175/1520-0450\(2000\)039<1341:BHCAQU>2.0.CO;2](https://doi.org/10.1175/1520-0450(2000)039<1341:BHCAQU>2.0.CO;2).
- Torres, S. and C. Curtis, 2007: *Initial Implementation of Super-Resolution Data on the NEXRAD Network*, 23rd Conf. on IIPS, San Antonio, TX, Amer. Meteor. Soc., 5B.10, URL https://ams.confex.com/ams/87ANNUAL/techprogram/paper_116240.htm.
- Zhang, J., et al., 2016: Multi-radar multi-sensor (mrms) quantitative precipitation estimation: Initial operating capabilities. *Bulletin of the American Meteorological Society*, **97** (4), 621–638, URL <https://doi.org/10.1175/BAMS-D-14-00174.1>.
- Zittel, W. D., R. R. Lee, L. M. R. J. G. Cunningham, J. Schultz, and R. L. Ice, 2015: *Geographical and Seasonal Availability of Light Rain, Dry Snow, and Bragg Scatter to Estimate WSR-88D Z_{DR} System Bias*, 31st Conf. on EPT, Phoenix, AZ, Amer. Meteor. Soc., 11.2, URL <https://ams.confex.com/ams/95Annual/webprogram/Paper265374.html>.
- Zrnić, D., V. M. Melnikov, and J. K. Carter, 2006: Calibrating Differential Reflectivity on the WSR-88D. *Journal of Atmospheric and Oceanic Technology*, **23** (7), 944–951, URL <https://doi.org/10.1175/JTECH1893.1>.